JOINT EUROPEAN TORUS JET

JET–P(94)28

Many Authors

11th International Conference on Plasma Surface Interactions in Controlled Fusion Devices (11th PSI)

(Mito-shi, Japan, 23–27 May 1994)

11th International Conference on Plasma Surface Interactions in Controlled Fusion Devices (11th PSI)

(Mito-shi, Japan, 23–27 May 1994)

Many Authors

JET-Joint Undertaking, Culham Science Centre, OX14 3DB, Abingdon, UK

Preprint of a paper to be submitted for publication in
Journal of Nuclear Material (Proceedings of 11th PSI)

Papers presented to
11th International Conference on
Plasma Surface Interactions in Controlled Fusion Devices (11th PSI)
(Mito-shi, Japan, 23-27 May 1994)

Review of Vacuum Vessel Conditioning Procedures at JET and their Impact on Plasma Operation

G Saibene, A Rossi, R D Monk[1], J Orchard, P Andrew, R Barnsley, D Cushing, P J Coad, S Davies, K Erents[2], H Y Guo, K Lawson[2], J Lingertat, G Matthews, G Sips, M Stamp, A Tanga.

JET Joint Undertaking, Abingdon, Oxon, OX14 3EA.
[1] Dept of Physics, Royal Holloway University of London, Surrey, TW20 0EX UK.
[2] UKAEA, Culham Laboratory, Abingdon, Oxfordshire, UK.

1. Introduction

The installation of the pumped divertor with 4 internal coils has consequences for the cleaning and conditioning of the JET vessel prior to plasma operation. A new Glow Discharge Cleaning (GDC) system has been commissioned and exploited during the 1994 restart of operation and the standard conditioning procedures have been adapted to suit the new in-vessel configuration. In addition, the glow discharge has been characterised with a number of plasma diagnostics specifically adapted for the parameters of the discharge. First results from initial plasma operation are used to evaluate the level of the present machine conditioning compared to that of past operation periods.

2. Conditioning procedures

To obtain long lasting effects from in-situ gettering (Be evaporation in the case of JET) the vacuum vessel has to be cleaned to high-vacuum standards. The previous standard conditioning procedure (high pressure water wash, bake at 350 °C + GDC in D and He in preparation for Be evaporation [1]) was not used because of the presence of the 4 internal divertor magnetic coils, in particular no water wash was carried out before closure, and the baking temperature (T_{vessel}) was limited to 250 °C. Moreover, the coil cases and the multilayered radiation shields (area = 1600 m^2) are out of reach of the glow, and are maintained at low T (from 250 down to < 100 C). The present procedure is :

1. Vacuum vessel baking at 250 °C.
2. High pressure (3 mbar) N_2 purge of vacuum vessel (to heat in a controlled way the radiation shields and coil case)

3. D and He GDC at T_{vessel} = 250 °C

4. Be evaporation

3. Vessel cleaning after in-vessel coil construction

Of particular relevance for the vacuum vessel contamination was the in-situ construction of the 4 divertor coils (including brazing, impregnation and curing). Surface analysis (by ^4He induced x-ray emission) of metallic in-vessel components at the end of the construction phase showed that manual wiping with either water or solvents was not effective in removing trace contaminants, such as Si, P, S and Cl. Therefore a new technique, high pressure blasting with frozen CO_2 pellets, was tested as an alternative to a water wash. Analysis of the test pieces indicated a reduction by a factor of 2 to 5 in the surface contamination levels. This method was then used to decontaminate the vacuum vessel after completion of the in-vessel construction phase [2]. More than 200 gr of material were removed from the vacuum vessel surfaces, of which 100 gr were inorganic compounds. Metals (Ni, Cr and Fe) and fairly large amounts of Cl, S and P were identified in the removed materials. It is estimated that between 50 and 95% of the contaminant material was removed from the vessel surface [2].

4. Vacuum baking and N_2 purge

In the previous bakeouts at 350 °C, two main thermal desorption peaks were measured, one at 210-240 °C and one at 320 °C. With the present limitation in temperature only the first thermal release peak is achieved. No desorption peaks are observed during a second bakeout cycle, carried out 24 h later and after a short venting. The lower baking temperature implies that a larger reservoir of H_2O, CO and CO_2 remains in the wall components, in particular for H_2O. In fact, the ratio m_{18}/m_{28} after bakeout is 10, compared with 5 or less, which was typical of the vacuum achieved after high T baking. However, the level of gaseous impurities is low (H_2O pp = $2x10^{-6}$ mbar, CO and CO_2 pp = 2-3 $x10^{-7}$ mbar), and represents less than 1% contamination for typical JET glow discharge pressures.

The radiation heat shields insulating the divertor coils from the hot vessel remain at temperatures as low as 80 °C during baking. To promote H_2O release from the inner layers of the heat shields, a continuous flow of N_2 at 3 mbar (contact

gas) was established in the JET vessel. The temperature of the shields increased by approximately 25 °C and the H_2O removal rate increased, on average, by a factor of 10. This procedure resulted in the release of $\cong 1x10^{22}$ water molecules, or 0.1 monolayer for an estimated area of the cold surface of 600 m^2.

5. Glow Discharge Cleaning

A new and improved GDC system was installed in JET during the 1992-93 shut-down. It consists of 4 (instead of 2) electrodes equally spaced toroidally situated at the top of the machine (see figure1). The electrodes are fed by current controlled power supplies, capable of 80 A total DC current (instead of 10) and maximum DC voltage of 1500 V. RF power up 150 W is available, to assist the breakdown and stabilise the glow at low pressures [3].

For the first time in JET the glow discharge has been diagnosed by using a real time wide-angle view colour CCD camera, fixed and movable Langmuir probes for current density and floating voltage measurement, visible spectroscopy and surface collector probes for the monitoring of metal sputtering. These were in addition to the standard mass spectrometry measurements of impurity partial pressures for cleaning rate calculation and vacuum assessment. The location of the diagnostics is shown in figure 1. In order to assess the influence of the gas species, total current and discharge base pressure on the glow uniformity and impurity removal efficiency, the following parameter space was investigated :

gas species : (H), D and He

glow currents : from 4 to 28 A

glow pressures : from $1x10^{-3}$ to $1x10^{-2}$ mbar

number of electrodes : 1 electrode at 4 A and 4 electrodes at 1 A each.

5a. Langmuir probe measurements.

One of the key elements that determines the cleaning efficiency of the glow discharge is the current density distribution, i.e. the effective surface area of the vessel influenced by the glow. In addition, the impurity removal rate from the walls depends on the voltage drop at the edge of the discharge, since it determines the incident energy of the ions (both ion-induced desorption and chemical sputtering are energy dependent). Moreover, for each impurity species, the global cleaning efficiency (the ratio between the characteristic pump out time

τ_p and the ionisation characteristic time τ_i) is a function of the glow background parameters in particular, the electron temperature T_e and density n_e. The main results of the measurements are summarised as follows (figures 2 and 3):

1. For all discharge conditions, the He GD is more uniformly distributed than D GD (figure 2), both on the walls and in the divertor region, in full agreement with CCD camera observations. The current densities at the limiters in He are, on average, a factor of 2 to 8 higher compared with D GD, and the effect is stronger at lower pressures. The current density at the divertor target achieved during He GD is a factor of 10 to 50 higher that achieved with D.

2. For both D and He, the CCD camera shows that the discharge stability deteriorates at high pressure. Uniform spreading of the glow is observed for $p < 1x10^{-2}$ mbar. This stability threshold is particularly pronounced in He (figure 3).

3. To maintain the same current, larger applied voltages at the electrode are required for D, compared to He GD (typically 300 V for D and 100-150 V for He). The corresponding potential drops measured at the edge of the glow follow the same trend (150 to 250 V for D and 20 to 120 V for He). For both D and He, the plateau value and the shape of the floating voltage profile (V_f) are not constant and are a function of the total current. Variation of the discharge pressure also causes changes in the plateau value of V_f. Also, for D, the shape of the V_f profile varies with pressure, in agreement with the CCD camera observation of increased discharge instability at high pressure. For most of the glow conditions the plateau value of V_f is reached at 10 to 15 cm from the vessel walls. The e-folding length mapped across equipotential surfaces varies from 7 to 10 cm.

4. The temperature and density of the glow have been derived from the I/V characteristic measured with the movable Langmuir probe. Typical values are $T_e \cong 2$ eV and $n_e \cong 10^{12}$ m^{-3}. The corresponding τ_i for CO and H_2O are >200 s, compared with $\tau_p = 27$s, therefore the ionisation of impurities removed from the walls is unlikely to play a major role in determining the glow cleaning efficiency.

5. The current density distribution is strongly dependent on the number of the electrodes. When only 1 electrode only is used instead of 4 (at constant total current), the average flux to the walls is reduced to 40% (D) and 60% (He). The

reduction in the divertor region is even more pronounced where the current density reduced to 20% and 40% for D and He respectively.

5b. Metal sputtering during glow discharge

The occurrence of metal sputtering during GDC has been monitored by analysis (RBS and PIXE) of the surface collector probe, exposed to several hours of GDC and with a visible spectrometer, configured for glow discharge measurements.

Preliminary results show that during D GD, no metal sputtering is observed. Both collector probe results (≅60 Ah exposure) and visible spectroscopy show no significant levels of metal deposited or in the glow. In contrast, during He GD the analysis of the visible emission spectra show traces of Cr at 12 A and 16 A total GD current . No collector probe measurements are available to correlate the measured line intensity to sputtering/deposition rates.

The occurrence of metal sputtering only during the He glow may be related to the more uniform spreading of the glow in the vessel, and therefore the larger metal surface reached by the glow.

5c. Glow discharge cleaning results

The restart of JET operation in early 1994 has been troubled by the presence of large air leaks, and the conditioning procedures had to be repeated. The main events and procedures that occurred during the machine restart, from the point of view of conditioning, have been :

1. Leak repair
2. Baking + N purge + D GDC (80 Ah) + He GDC + Be evaporation
3. Short period of plasma operation
4. In-vessel intervention (opening to air)
5. Full conditioning cycle (2) repeated but D GDC for 180 Ah and He GDC for 100 Ah.

At the start of JET operation, the first D GDC cycle was interrupted prematurely (the D cleaning is usually stopped when CD_4 and C_2D_2 production due to chemical sputtering of graphite dominate over ion induced desorption of CO). The subsequent Be evaporation was not very effective and D GDC was repeated. Probably due to the Be coating on the surfaces, a large part of the "dirty" surfaces were not exposed to the glow and the cleaning efficiency was close to

zero. In total, only $5x10^{22}$ CO molecules were removed, that is only 30% of the typical amount of CO removed during the first conditioning after a shut-down.

A new D GDC cycle was carried out after baking and N purge (procedure 5). Good cleaning was achieved after 15 h of glow, or 180 Ah, at an average current of 13 A. The amount of CO and H_2O removed ($\cong 8x10^{22}$ CO molecules) is similar result to that obtained in 1991 after short a in-vessel intervention, but with the vessel walls at 350 °C.

The time evolution of H_2O and CO removal is dominated by the effects of the source depletion (accessible O in the near surface layers). It is found that at the end of the glow the partial pressure of CO scales with $t^{-0.5}$, compared to $t^{-0.85}$-$t^{-0.7}$ at the beginning. This indicates that a "diffusion dominated" release regime has been reached.

The fact that the removal rate depends at any time on the actual wall source (unknown) complicates the assessment of D GDC efficiency. Therefore a systematic discharge parameter scan was carried out in the phase of the glow dominated by hydrocarbon production ("infinite source"), to distinguish the variations in impurity removal efficiency due to changes of the glow parameters (I and p) from the source time evolution. The results are summarised in figure 4.

1. The removal rate increases very strongly with glow current, for $I<4$ A (figure 4a). For $I > 4$A the removal rate remains proportional to the glow current, but the dependence is weaker. Some increase in the removal rate is observed above 20 A, possibly related to the measured increase of V_f from 150 to 250 V.

2. No strong dependence of the removal rate on glow pressure is observed.

He GDC was carried out after the D glow. The main aim of the He glow is to remove the residual CO and H_2O in the walls while avoiding C sputtering (during He glow, the measured peaks 18 and 28 are due the release of CO and H_2O and are entirely determined by ion induced desorption), and also to deplete the wall from D. The CO removal rate was quite low, and consistent with "clean" surfaces. D is also removed during the glow, as shown by the presence of mass 6 in the residual gas analysis spectra and also indicated by the D_γ line measured by the visible spectroscopy . The results of the glow parameters scan are (figure 4 b and d):

1. The removal rate is independent of the glow current. This is consistent with the observation of diffusion limited CO release during the D glow preceding the He glow.

2. In contrast to D, the cleaning rate for both CO and H_2O shows a clear dependence on the glow pressure and it is maximised at low pressures, below about $4x10^{-3}$ mbar. The roll over of the impurity removal rate could be related to the measured sharp increase in the edge V_f (from 20 to 120 V), for $p > 4x10^{-3}$ mbar. The decrease in the CO removal rate associated to the increased energy of the bombarding ions could be related to a decrease of the desorption cross section with increasing ion energy, observed in some cases for light primary ions [4].

Be evaporation was carried out after the glow discharge cleaning sequence. The average thickness of the layer deposited in each 45 minutes evaporation is estimated to be around 20 nm (collector probe data). A further 9 Be evaporations have been carried out in the following 4 weeks of regular plasma operation, in same cases preceded by overnight He GDC. The vacuum conditions have slowly but continuously improved. The main impurity partial pressures have been reduced below the $1x10^{-8}$ mbar level, with an improvement of an order of magnitude over the pre-Be vacuum.

6. Overview of the first JET plasmas

The level of conditioning of a Tokamak is ultimately measured by the plasma performance and characteristics. Due to the very limited time of JET operation to date, only a preliminary assessment is presented here.

A good indication of the global level of impurities in a plasma is given by the radiated power levels. Figure 5 shows the levels of P_{rad} for previous operation and the current 1994 campaign. The 1994 values (0.44 MW) compare well with the typical values achieved in the 1991 campaign (0.52 MW). However, this initial 1994 database includes only 2 MA plasmas, while the 1991 pulses were mostly at 3 MA.

Additional information on the impurity content of the plasma is obtained by the analysis of the data obtained with a broad band soft x-ray spectrometer (impurity survey in the 1 to 100 A range) [5]. Although Be is rapidly eroded from the

plasma facing surfaces, the impurity ccntent (C, O, Cl and metals) remains fairly constant over a large number of pulses. Quantitative analysis is in progress, and first indications are that the levels of impurities in the 1994 plasmas are comparable to the past, with the exception of O, that appears to be somewhat higher.

7. Conclusions

1 The standard cleaning and conditioning techniques developed at JET in the past have been modified and adapted to the new machine characteristics. The improved GD system has been successfully commissioned and exploited for the 1994 restart.

2. The achieved impurity removal during conditioning is similar to that achieved in the past, in spite of the lower baking temperature and the presence of large cold and surfaces not in the reach of the glow.

3. The depletion of the near surface reservoir of O is successfully achieved by D GD, as shown by the diffusion limited release rate of CO.

4. For the first time at JET, the glow discharge cleaning has been extensively diagnosed and the glow current distribution, edge potential, density and temperature measured in conjunction with systematic scan of the glow gas, current and pressure. The overall cleaning efficiency and the impurity removal rate are related to the measured current density distribution and to the variation in the edge potential. These tests have also established that for a Tokamak of the size of JET the minimum number of GDC electrodes for an uniform glow coverage is 4, in particular for D GD. Location of the electrodes at the midplane could be beneficial for improved conditioning of the divertor target.

5 The "base level" impurity content of the plasma is low, and comparable to the 1991 levels. A possible exception is O, for which the source is likely to be the leaks that occurred during the restart of the machine while the vessel was hot.

References

[1] J Orchard, A T Peacock and G Saibene, J of Nucl Mat 200(1993) 395-399.

[2] S M Scott, A D High, G Saibene et al, 1994 Int Sym on Decontamination and Decommissioning, Knoxville, USA (1994).

[3] P Andrew, G Bosia, R Claesen et al, to be published.

[4] E Taglauer, Nucl Fus Special Edition 1994.

[5] R Barnsley, K D Evans, N J Peacock and N C Hawkes, Rev Sci Inctrum 57(8) (1986) 2159.

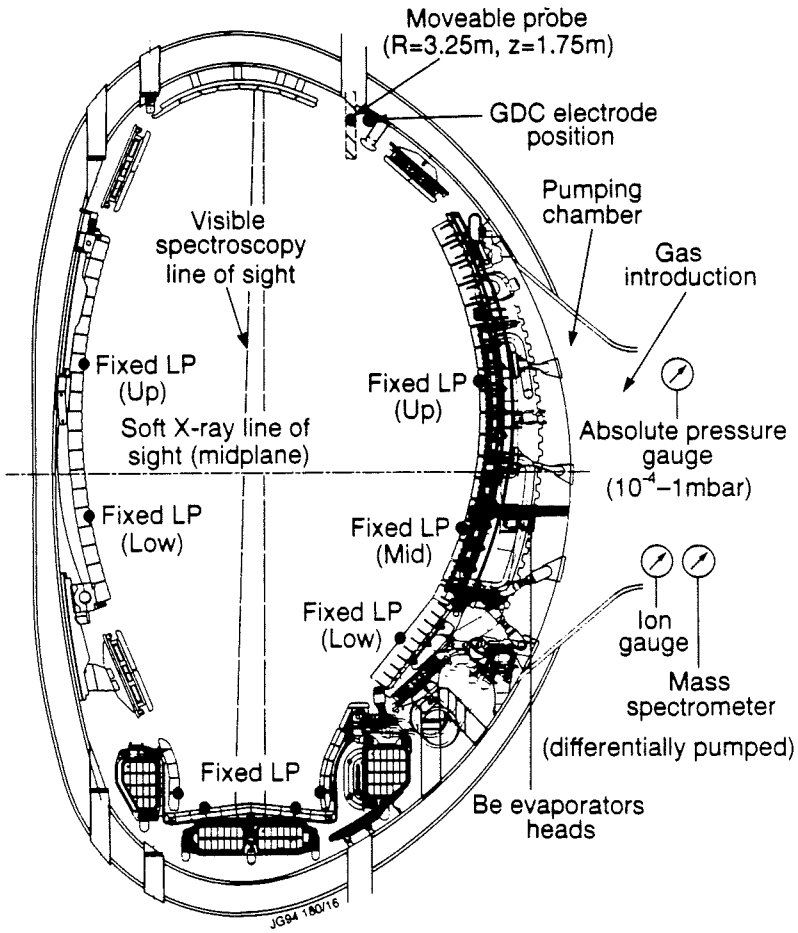

Figure 1 composite figure illustrating the poloidal location of the GDC electrodes, of the gas introduction system and of the diagnostics used for the characterisation of the glow discharge.

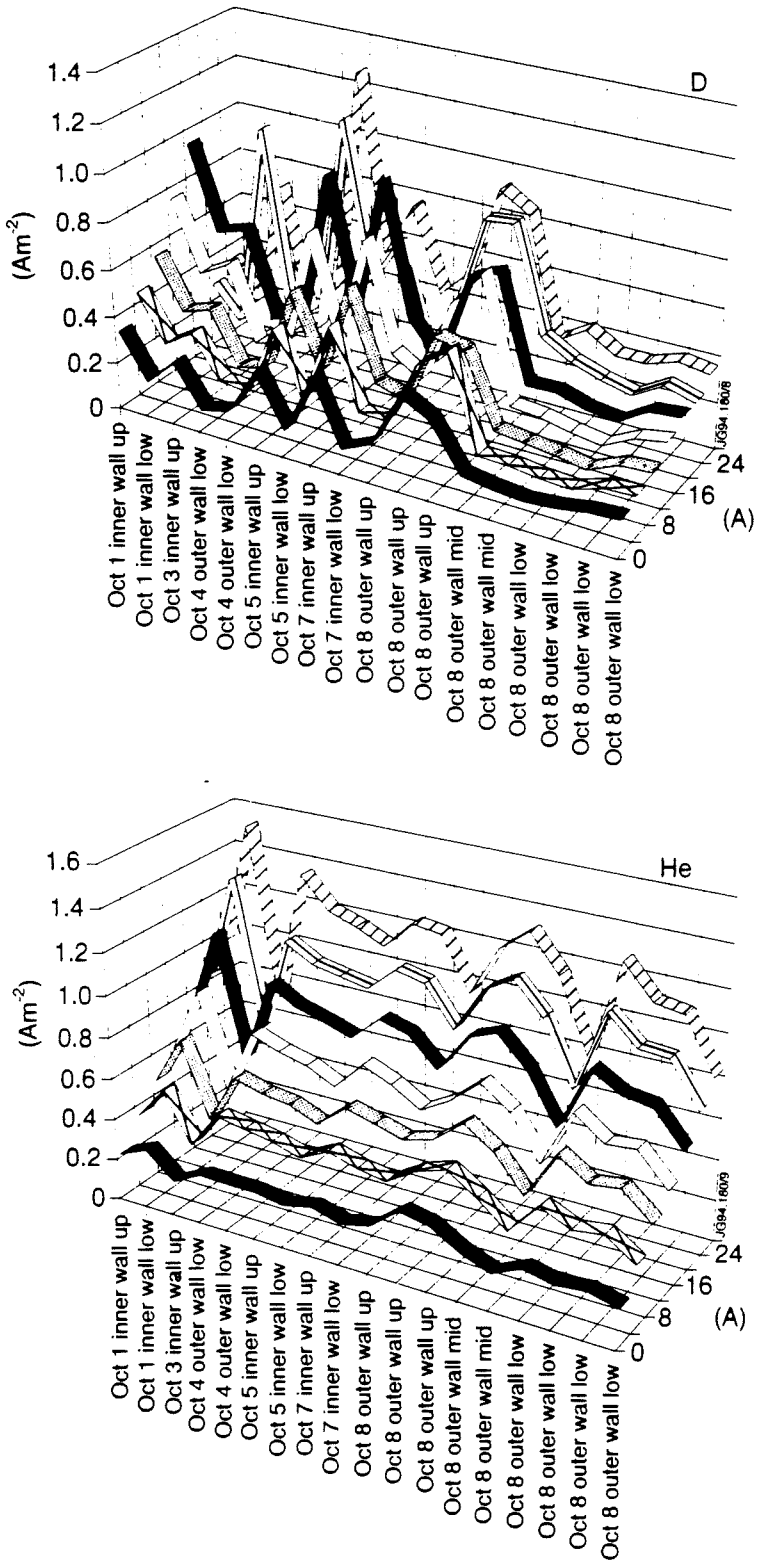

Figure 2 : poloidal and toroidal distribution of current density on the limiter probes as a function of current for D (a) and He (b) glow discharge at fixed pressure

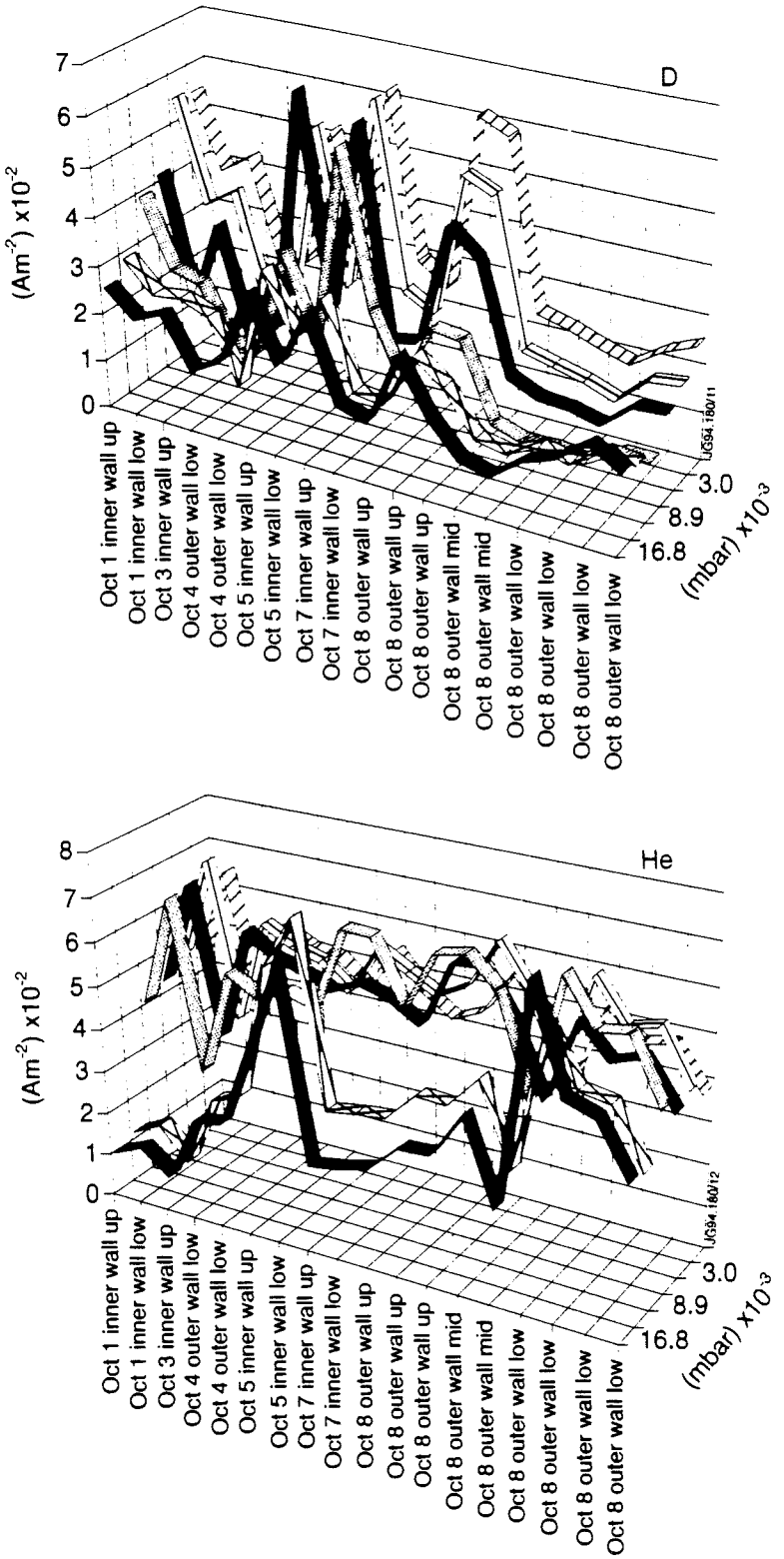

Figure 3 : poloidal and toroidal distribution of current density on the limiter probes as a function of pressure for D (a) and He (b) glow discharge at fixed current.

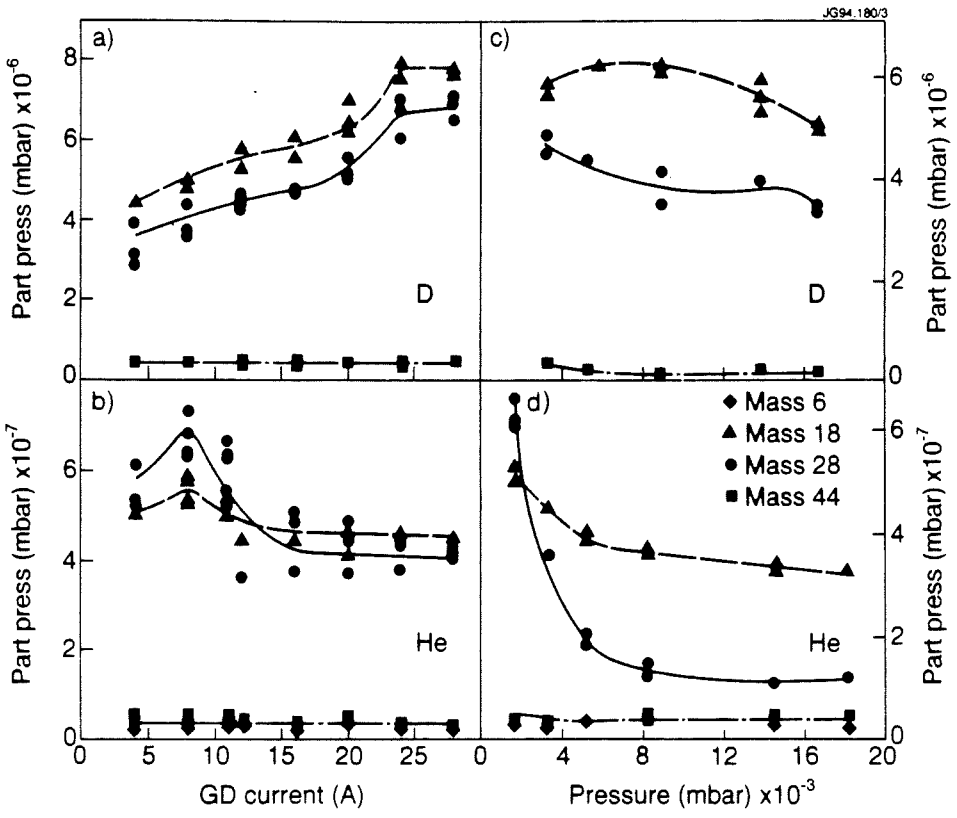

Figure 4 : current and pressure dependence of masses 18, 28 and 44 during D and He GDC. For D GD data, the masses 18 and 28 are hydrocarbon dominated. Data taken during the same parameter scan as for the Langmuir probe measurements.

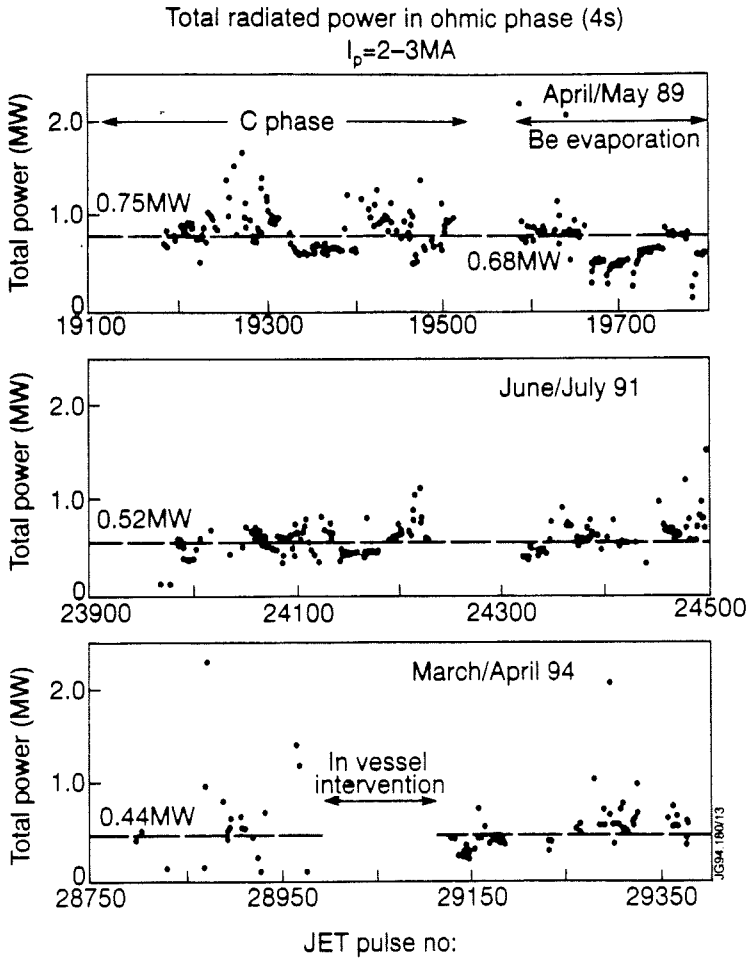

Figure 5 : Total radiated power in the Ohmic phase of JET plasma discharges : data from 1989 (C and Be), 1991 and 1994.

Modelling of Hydrogen Conditioning, Retention and Release in Tore Supra

C Grisolia[1], L D Horton, J K Ehrenberg.

JET Joint Undertaking, Abingdon, Oxon, OX14 3EA.
[1] Permenent address: Association EURATOM–CEA sur la Fusion Controlée, C E Cadarache, 13108 St Paul lez Durance Cedex, France.

Abstract : A model based on a local mixing model has been previously developed at JET to explain the recovery of tritium after the first PTE experiment. This model is extended by a 0-D plasma particle balance model and is applied to data from Tore Supra walls saturation experiments. With only two free parameters, representing the diffusion of hydrogen atoms and the volume recombination process between hydrogen atoms into molecules, the model can reproduce experimental data. The time evolution of the after-shot outgassing and the integral amount of particles recovered after the shot (assuming 13 m^2 of interacting surfaces between plasma and walls) are in good agreement with the experimental observations. The same set of parameters allows the model to simulate after-shot outgassing of 5 consecutive discharges. However, the model fails to predict the observed saturation of the walls by the plasma. Results from helium glow discharge (HeGD) can only be partially described. Good agreement with the experimental hydrogen release and its time evolution during HeGD is observed, but the model fails to describe the stability of a saturated graphite wall.

I) INTRODUCTION

The study of the retention and recycling of hydrogen in tokamak walls is of crucial importance in the understanding of particle inventory and of particle control.

The plasma particle balance in Tore Supra has been extensively studied using a special experimental procedure (Grisolia *et al.*, 1992). This procedure consists of doing a

long series of D_2 shots beginning with deeply desaturated graphite walls obtained after a very long helium glow discharge (HeGD). The essential results obtained during this special procedure are:

- The HeGD removed 4×10^{21} atoms/m^2 from the vessel walls with a decreasing rate falling as $t^{-0.5}$ (60 hours of HeGD; glow current=3 A; glow pressure=0.3 Pa of He; graphite surface=100 m^2).
- Throughout the series of tokamak shots, the hydrogen release in the 600s after the shot was 20% of the total gas input. For typical shots studied here, the total amount of particles recovered is 8×10^{20} atoms. During this time, the hydrogen release rate decreased as $t^{-0.775}$ (these results are typically observed in tokamaks with graphite or carbonised walls).
- After a certain number of consecutive shots (18-20), it is no longer possible to control the plasma density and the series ended with a density-limit disruption.

Data from the JET Preliminary Tritium Experiment (PTE) has been used to develop a model of recovery of tritium from vessel walls (Andrew *et al.*, 1994).

In this paper, following a concept introduced previously (Ehrenberg, 1992), this PTE model is extended by the addition of a 0-D plasma particle balance model which calculates for a given plasma density the flux impinging on the wall during a shot. In order to validate the JET PTE analysis, the new model is then applied to the Tore Supra experiments described above.

II) WALL MODEL

This model is based on the local mixing model developed to explain the ion-induced release of deuterium from carbon in laboratory experiments (Brice, 1990). In this model, hydrogen in the graphite walls is described by means of 2 populations, one which is trapped and another which is mobile and can diffuse in the material.

The time evolution of these populations is given by 2 coupled equations:

$$\frac{\partial C_s}{\partial t} = D\left(\frac{\partial^2 C_s}{\partial x^2}\right) + \Phi\delta(x - x_0) - \Gamma C_s^2 - \frac{\partial C_t}{\partial t} \qquad (1)$$

and

$$\frac{\partial C_t}{\partial t} = \frac{1}{\tau_a} C_s \left(1 - C_t / C_{0t}\right) - \frac{1}{\tau_a} \beta C_t - \sigma \Phi U\left(x - x_0\right) C_t \qquad (2)$$

where C_s (C_t) are the concentration of mobile (trapped) particles in the wall (m^{-3}). Here C_{0t} represents the trap concentration. In graphite, saturation is reached when the concentration of hydrogenic atoms is equal to 0.4 the carbon concentration. So $C_{0t}=4\times 10^{28}$ m^{-3}.

x (m) represents the depth into the material with x = 0 at the surface.

The first term of the right hand side of equation (1) is a diffusion term where D is the mobile particle diffusion coefficient (m^2s^{-1}).

The second term represents the particle source. Φ is the hydrogenic flux onto the surface and will be defined below ($m^{-2}s^{-1}$). The particles are assumed to be deposited at a depth of x_0 = 5 nm which corresponds to the average penetration depth of 100 eV deuterium ions in carbon.

The third term corresponds to a volume recombination process introduced by Andrew *et al.* to explain the JET PTE results. Here it is assumed that it applies between the surface and $x = 2x_0$ on the assumption that this volume recombination process occurs at interior surfaces created by ion induced damage to the bulk material within the range of their depth of penetration. Γ is the volume recombination rate coefficient (m^3s^{-1}) and is defined below (see boundary conditions).

The first term of the right hand side of equation (2) is a trapping term. This process is high when the traps are empty and it decreases when the concentration of occupied traps increases.

The second term is the thermal detrapping term. $\beta = \exp(-E_t/kT)$ where T is the wall temperature (450 K in these experiments) and E_t is the trapping energy. Different values of E_t can be found in the literature between 0.3 and 3 eV (Brice, 1990). However, if E_t is too high, the trapped particles cannot be detrapped by thermal activation and so the concentration of mobile (diffusing) particles is low as long as saturation has not been reached. This is inconsistent with the results from HeGD where the total number of

hydrogen atoms released is larger than that trapped in the material within the range of the bombarding helium ions. Hence a suitable reservoir of mobile hydrogen must be present. Therefore E_t is assumed to be small, here 0.3 eV, and thus $\beta = 5*10^{-4}$.

τ_a is the time constant for the trapping/detrapping process. Here it is assumed that the two populations are in quasi-equilibrium and so τ_a is small (here, $\tau_a = 10^{-2}$ s).

The third term of equation (2) represents the induced detrapping term where σ is the detrapping cross section (m^2).

Boundary conditions:

@ x = 0 $$D\left(\frac{\partial C_s}{\partial x}\right) = K_r C_s^2$$

At the surface of the material, the diffusion flux is equal to the surface recombination flux. Kr is the surface recombination coefficient ($m^4 s^{-1}$). In addition, the volume recombination coefficient, Γ, is chosen to be Kr/x_0. During all the experimental situations studied in this paper (except at the very beginning of the HeGD), the volume recombination process is much greater than the surface recombination one (see IV a))

@ x = ∞ $$D\left(\frac{\partial C_s}{\partial x}\right) = 0$$

Initial conditions :

At the beginning of the He GD procedure, the walls are saturated and $Ct = 0.99 \times Cot$. At this time, the two hydrogenic concentrations are in equilibrium $(\partial C_t/\partial t) = 0$ and $C_s = \beta C_t/(1-C_t/C_{0t}) = 4.95 \times 10^{-2} C_{0t}$.

Expression of Φ :

During HeGD, the re-implantation of deuterium is assumed to be nil and the source term for the hydrogenic content is set to zero. Therefore, Φ plays only a role in the induced detrapping term in equation (2).

$$\Phi = (I/q)/S_{tot} = 2 \times 10^{17} \text{ m}^{-2}\text{s}^{-1}$$

where I is the glow current (=3 A), S_{tot} is the total graphite wall surface (=100 m^2 in Tore Supra) and $q=1.6\times10^{-19}$ C.

During the shot, Φ is given by a classic 0-D plasma particle balance model between the plasma and the graphite wall. The time evolutions of the plasma (N_p) and wall (N_W) populations are described by the two following equations:

$$\frac{dN_p}{dt} = -Q_{in} + \varphi_{SOL}$$

and

$$\frac{dN_w}{dt} = -\varphi_{SW} + \Phi$$

Some hypothesis are made in this simple model:

- due to the very small particle residence time and volume of the SOL, this third reservoir is neglected.
- all the particles reflected by the wall are supposed to gain sufficient energy during their acceleration by the Langmuir sheath to be directly injected in the plasma.

All the fluxes involved in the two equations above are defined using the next drawing :

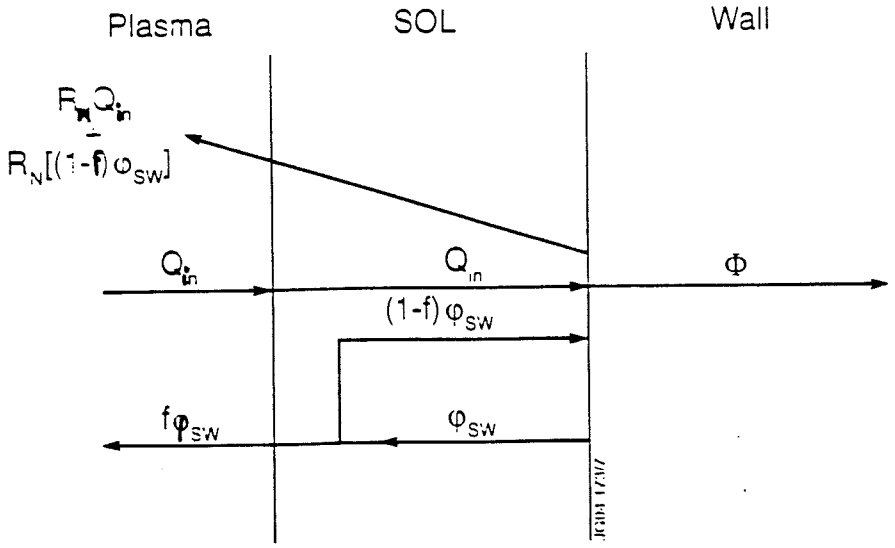

where:

• Rn is the particle reflection coefficient (=0.25) (see Eckstein, 1991)

• Qin represents the flux coming out the plasma = $(N_p/\tau_p)\times(1/S)$ where τ_p is the particle confinement time (=0.2s) and S is the wall surface area ($=5m^2$) interacting directly with the plasma . Here $Np=5.4\times10^{20}$ particles and $Qin=5.4\times10^{20}m^{-2}s^{-1}$.

• the particle flux coming out from the wall ($=\varphi_{SW}$) is given by the wall model. It is divided into two components. One which is directly injected into the plasma ($=f\times\varphi_{SW}$) and another one which falls back onto the wall ($=(1-f)\times\varphi_{SW}$). f is the fuelling efficiency and is supposed to be equal to 0.15.

• φ_S is the particle flux incident on the wall. $\varphi_S = Qin + (1-f)\times\varphi_{SW}$.

• Φ is the particle flux entering the wall and it is the input to the wall model. $\Phi = \varphi_S\times(1-Rn)$

• φ_{sol} is the particle flux entering the plasma = $Rn\times\varphi_S + f\times\varphi_{SW}$.

In this model, N_p is assumed to be constant.

Equilibrium is reached when the particle flux coming out the plasma is equal to the flux entering the plasma : $Qin = \varphi_{sol}$.

III) WALL DEPLETION OF HYDROGENIC PARTICLES BY HeGD

As indicated above, Φ is acting only by the induced detrapping term and $\sigma=8\times10^{-21}\ m^2$.

The hydrogen released by HeGD as calculated with the model is presented figure 1. The set of parameters used is:

$\Gamma = 10^{-28}\ m^3s^{-1}$ ($Kr = 5\times10^{-37}\ m^4s^{-1}$)

$D = 7.5\times10^{-19}m^2s^{-1}$

The hydrogen release quickly follows a $t^{-0.5}$ time evolution in agreement with the experimental observations. This suggests that the release is diffusion limited. The total amount of atoms removed from the walls during this long HeGD is 1.4×10^{21} atoms/m^2 which is within a factor of 3 of the experimental value.

However, the same results are obtained with $\sigma=0$ e.g. without particle induced detrapping which means that release of hydrogen would also take place without HeGD. This is because the volume recombination process is much larger than the particle induced detrapping one (even if much larger values of σ are used). Two attempts to remove this weakness in the model were unsuccessful:

- if τ_a is increased, the detrapped particles stay longer in mobile form. Then the ion induced detrapping term becomes more important during HeGD. But, under these conditions, it becomes impossible to simultaneously match the measured total release and the $t^{-0.5}$ time evolution.
- if C_{0t} is increased to mimic the high surface roughness of a tokamak graphite then again the ion induced detrapping term becomes more important in HeGD and a good fit for both experimental results (total release and time evolution) is obtained. But now it becomes impossible to fit the time evolution of the after-shot outgassing release (see below).

IV) AFTER-SHOT OUTGASSING

a) Wall conditions before outgassing

Before the first shot, the trapped and mobile particle profiles in the wall are given by results obtained after the HeGD.

During the shot, the trapped and mobile particle profiles are calculated using the 0-D plasma model and the 1-D wall model described above.

In figures 2 and 3, trapped and mobile particle profiles are presented before and after a discharge. During the discharge, Q_{in} is high and the wall traps are quickly saturated. By the end of the discharge, the mobile particle concentration reaches a high value (see figure 3) which is almost reproducible from shot to shot for a given value of N_p. This reproducibility of the mobile particles profile leads to the reproducibility of the after-shot outgassing production (see point V).

With this mobile particle profile, it is obvious that the volume recombination process is much greater than the surface recombination one.

In figure 4, the time evolution of φ_{SOL} (the flux entering the plasma) during a shot is presented. With constant plasma density, it takes only 3 to 4 s to get the equilibrium between Qin and φ_{SOL}.

b) After-shot outgassing

During the first 20s after the shot, the calculated after-shot outgassing release is much higher than the experimental observed release.

To improve this during the first 20s, a "current ramp down" phase is introduced at the end of the shot for 5s during which Φ, the particle entering the wall, is set to 0. During this "current ramp down", particles outgassing from a high flux implanted surface are supposed to be sprayed onto a much larger surface. This larger surface is far from saturation (e. g. $\varphi_{SOL} << Q_{in}$) and pumps particles which are released from the highly implanted surfaces during the rampdown. After transferring particles, the after shot outgassing releases from the two surface areas are identical. This transferring process homogenises the tokamak surface conditions in terms of hydrogen content of surfaces which are near the last closed flux surface.

The same set of parameters (Γ and D) gives good agreement with the experimental results (see figure 5) :

- the calculated after-shot outgassing rate follows a $t^{-0.73}$ evolution which is very close to the experimental one.
- the total number of particles recovered is between 5×10^{19} and 6×10^{19} particles/m^2. Therefore, 13 m^2 of wall surfaces have to be involved to obtain the total measured production which is in good agreement with estimates of surface areas interacting with the plasma given by H_α measurements.

V) SERIES OF TOKAMAK DISCHARGES

In figure 6. the after-shot outgassing releases for a series of consecutive shots are presented (for the sake of clarity, only the after-shot outgassing after the first, the second and the fifth shot are shown)

During this series, the releases follow almost the same time dependence which is in agreement with experiment. For the same shot conditions, the total number of particles recovered during after-shot outgassing is identical ($6*10^{19}$ particles/m^2).

The calculated particle balance during and after the 4^{th} shot is (all the quantities expressed per m^2) :

+ 2.28×10^{20} which is the total amount of particles deposited in the wall during the shot.

- 1.60×10^{20} is the quantity of outgassed particles during "current ramp down".

- 6.00×10^{19} corresponds to the outgassed particles during the following 600 s.

This gives a net result of + 5.40×10^{18} particles left in the wall at the end of one cycle.

This low deposited amount obtained for every simulated shot cannot be used to reproduce the small number of experimental shots done before reaching the density limit.

The description could be improved if the model included implantation of energetic neutrals during a shot (e.g. particles whose energy is higher than 100 eV). These neutrals penetrate deeper into the material, beyond the zone where the volume recombination process takes place and thus would be trapped in the material. This new deposition process could increase the wall loading and has to be included in future studies.

VI) CONCLUSIONS

The JET PTE local mixing model including volume recombination process has been applied to a TORE SUPRA wall saturation experiment.

With $\Gamma = 10^{-28}$ m^3s^{-1} ($Kr = 5\times10^{-37}$ m^4s^{-1}) and $D = 7.5\times10^{-19}$ m^2s^{-1}, this model gives a reasonable fit to the measured after shot outgassing release. This value of D compares well with those previously published (see Grisolia, Grosman and Bardon, 1992). Γ represents here a new process only introduced by Andrew and coworkers. However, $\Gamma = K_r/x_0$ and $Kr = 5\times10^{-37}$ m^4s^{-1} is in the range of the values found in the literature. A t

0.73 time evolution of the outgassing production is calculated which is very close to the experimental one. The total amount of particles recovered after a shot is 6×10^{19} atoms/m^2 and 13 m^2 of interacting walls have to be used to match the total experimental outgassing after a discharge.

Using the same set of parameters, the experimentally observed reproducibility of after shot outgassing is also simulated in a series of 5 consecutive shots.

The model fails to describe the experimentally observed saturation of the walls by consecutive discharges. Energetic charge exchange neutrals that penetrate deep into the surface beyond the recombination zone may need to be included.

Again using the same parameters, the model is only in partial agreement with HeGD experimental results:

- the calculated total release of hydrogen by HeGD is a factor of 3 smaller than the experimental one, whereas
- a $t^{-0.5}$ time evolution hydrogen release rate is calculated similar to the experimental one.

The model fails to describe the stability of a hydrogen saturated graphite wall in the absence of ion induced detrapping.

REFERENCES

Grisolia, C., *et al.* J. Nucl. Mater. **196-198** (1992) 281.

Andrew, P., *et al*, Nucl. Fusion **33** (1994) 1389.

Ehrenberg, J , *et al.* J. Nucl. Mater. **196-198** (1992) 992

Brice, D.K., Nucl. Instrum. Methods Phys. Res., Sect B **44** (1990) 302.

Eckstein, in Atomic and plasma material interaction data for fusion, supplement to Nuclear Fusion. IAEA, Vienne, 1991.

Grisolia, C. ,Grosman, A. and Bardon, J., J. Nucl. Mater. **187** (1992) 74

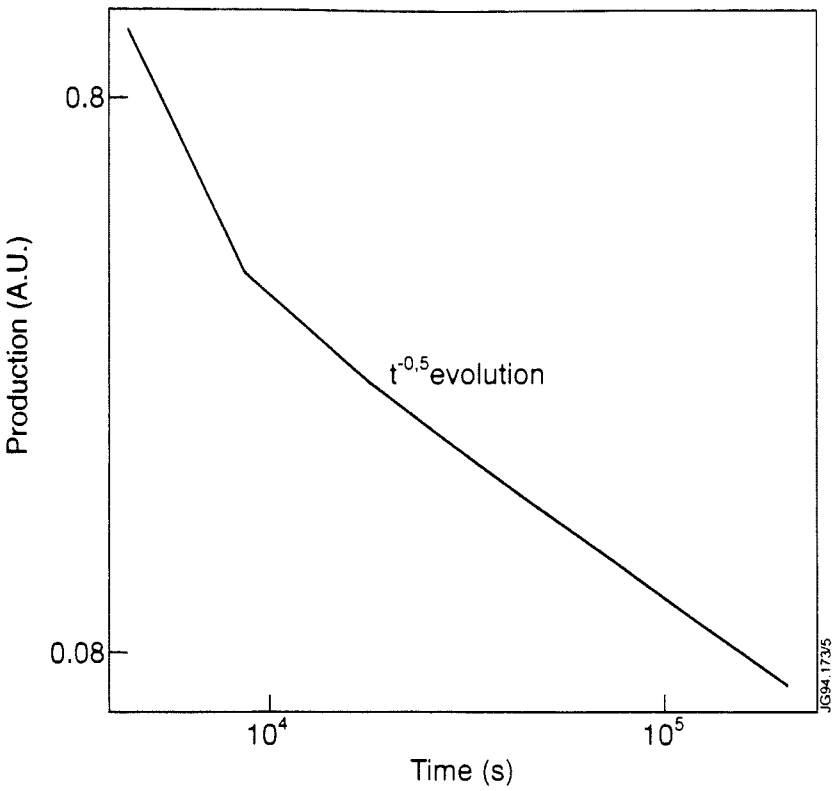

Figure 1 : Time evolution of calculated HeGD production.

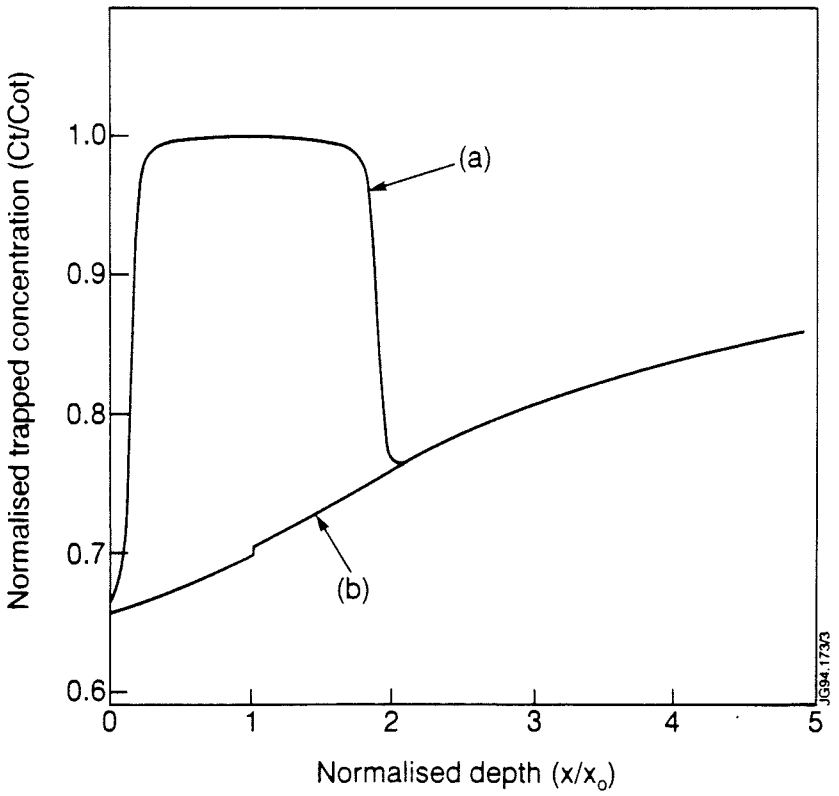

Figure 2 : Normalised trapped concentration profiles (b) before and (a) after the shot.

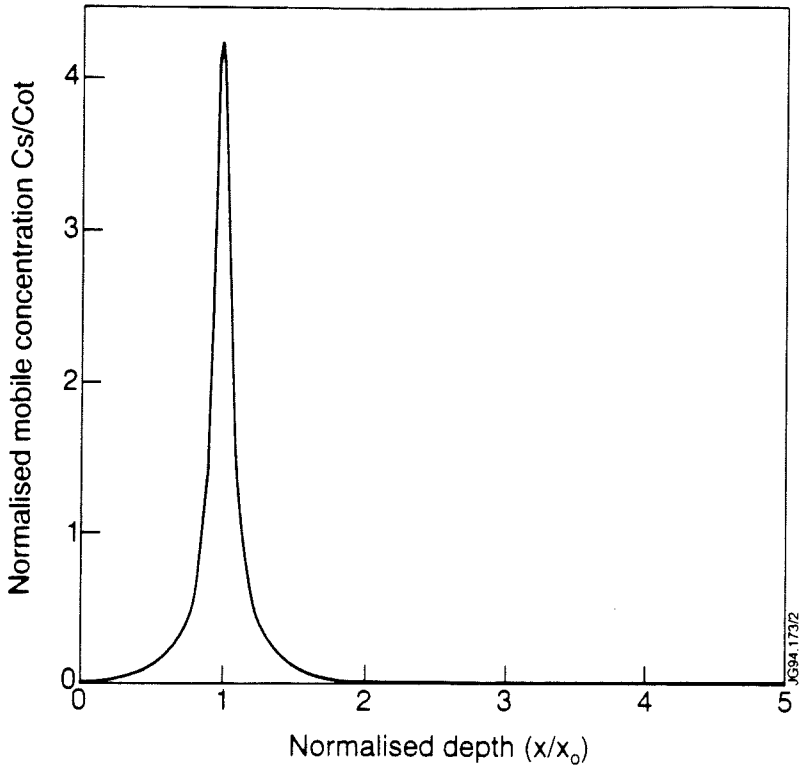

Figure 3 : Normalised mobile particle concentration profile after a shot (the profile before the shot is too low to be seen on the scale).

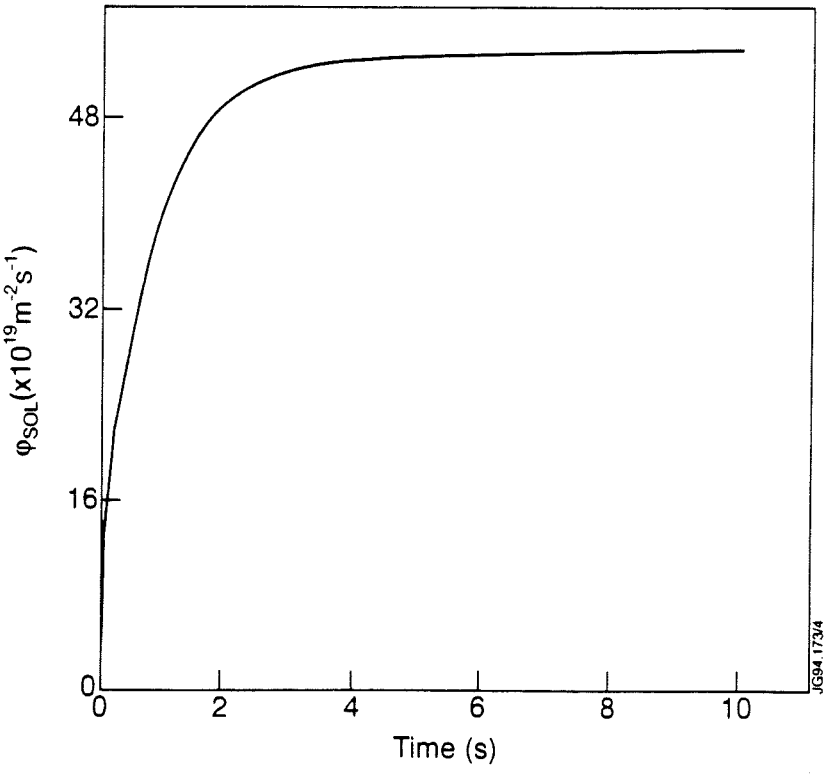

Figure 4 : Time evolution of the particle flux entering the plasma (φSOL) during one shot.

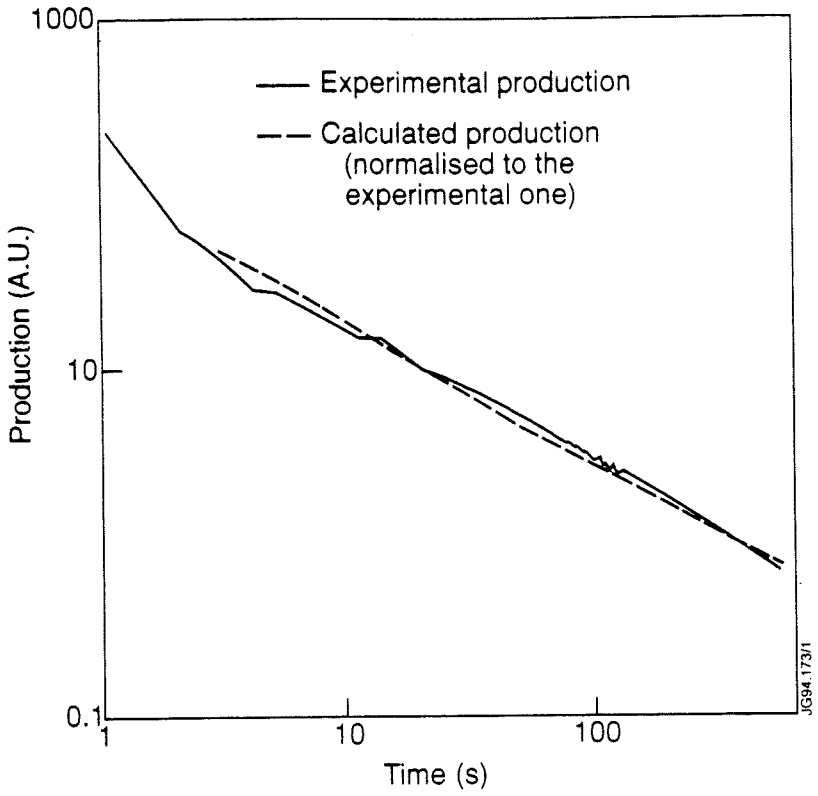

Figure 5 : Time evolution of the experimental and calculated after-shot outgassing release.

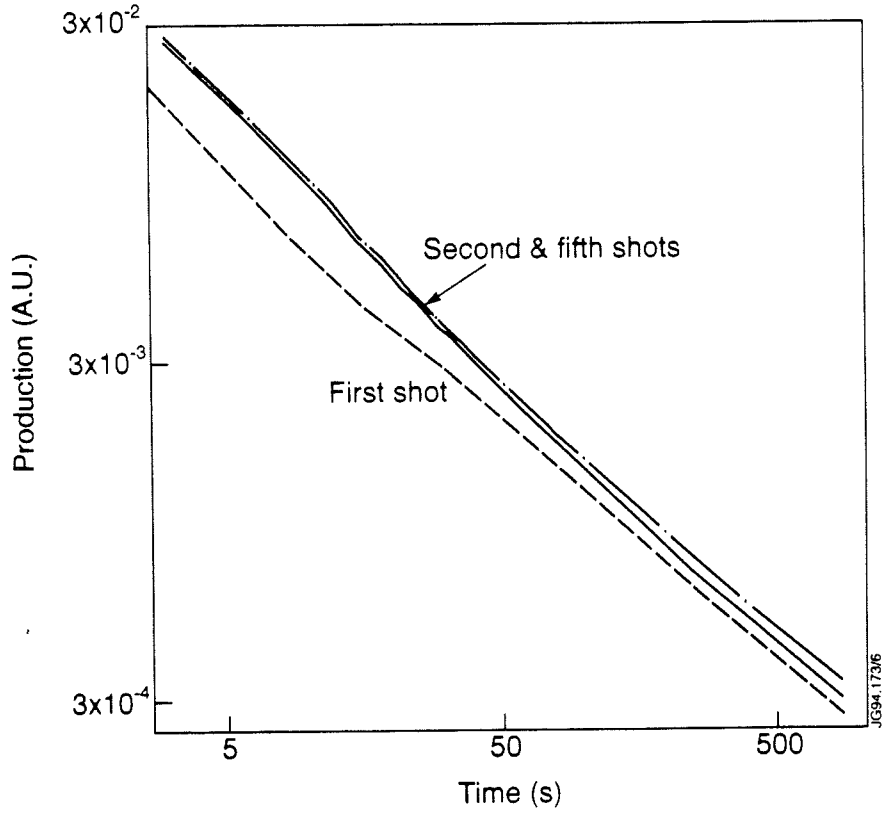

Figure 6 : Time evolution of after-shot outgassing production during a series of shots.

Large Carbon Fibre Reinforced Carbon Tiles for a Mark II Divertor in JET

M A Pick, H Altmann, D Ciric, E B Deksnis, H D Falter,
J Fanthome, C Lowry, P Massmann, R B Mohanti,
A T Peacock, R B Tivey.

JET Joint Undertaking, Abingdon, Oxon, OX14 3EA.

1. Introduction

JET has successfully operated since 1983 with plasma facing components comprising fine grain graphite tiles, a wide variety of carbon fibre reinforced graphite (CFC) tiles as well as beryllium tiles. The experience at JET has highlighted the advantages and disadvantages of the various materials from a point of view of plasma wall interactions, plasma disruptions, as well as design and procurement. The new Mark II Divertor for JET has been designed to investigate the effects of divertor geometry on plasma performance. Actively cooled divertor target systems are difficult to exchange easily, quickly and, in particular, using remote handling tools. The new Mark II divertor incorporates large CFC tiles (approximately 400 x 180 mm) which are shaped and supported in a way that ensures maximum power handling capability and the elimination of carbon blooms caused by hot spots. The Mark II design relies on the thermal inertia of the target tiles in order to maintain acceptable target surface temperatures.

2. Mark II Design

The Mark II divertor, shown in Fig. 1, consists of a toroidally continuous U-shaped structure which is internally stable, and a set of three rings of tile carriers bolted onto the bottom and sides of the structure. The structure itself consists of 24 individual water cooled modules bolted together into a continuous ring in the vessel and attached to the vessel via the 36 main clamps of the two central divertor coils. It provides a flat and rigid base and cylindrical inner and outer sides for the attachment of the tile carriers. The tile carriers can vary depending upon the chosen divertor shape and are fully equipped with tiles and any associated diagnostic systems prior to being installed in the vessel. The exchange of tile carriers, which is an easy and rapid procedure, can be performed by the remote handling tools available in JET.

The tile carriers to be initially installed, Fig 1, allow the investigation of a large variety of

plasma configurations including high power discharges and discharges with the separatrix intercepting either the side or the lower target tiles. In order to allow for a high power handling capability the total area wetted by the plasma has been increased as far as practicably possible, in both toroidal and poloidal direction. The design has resulted in a calculated maximum power density of less than $5MW/m^2$ on the tiles for most plasma configurations and up to $15MW/m^2$ for particular discharges envisaged, assuming full power operation of which 50% is conducted to the divertor target.

The toroidal wetted length is optimised by using target tiles which are long in the toroidal direction and mounted in a way which guarantees a minimum tile-to-tile misalignment. The tiles are attached to the tile carrier by a single spring loaded central bolt attached to a dumbbell shaped rod inserted in a hole drilled into the tile, and supported on four corner pads, Fig. 2. Each tile carrier is fitted with tiles but adjacent tiles always share the corner support pads. The tile-to-tile step accuracy is not therefore dependent on the exact alignment of adjacent tile supports but only upon the tolerance of the tile thicknesses.

The poloidal inclination of the target tiles was chosen so that the poloidal area wetted by the plasma scrape-off is increased as far as possible for the plasma configurations envisaged. Tile-to-tile steps, designed to protect tile edges, are also included in the poloidal direction and shown in Fig. 1.

The front surfaces of the tiles are, without exception, free of holes or cut-outs either for tile attachment or for diagnostic purposes.

3. Tile Material Requirements

The 400 x 180 x 40mm Mark II divertor tiles can be made of either beryllium or carbon fibre reinforced carbon (CFC) material. CFC was chosen as the tile material for the first installation because it provides a robust and forgiving solution. It can be followed up by a beryllium tile design once the optimum divertor geometry has been identified.

The design was based on material properties such as thermal conductivity, thermal expansion coefficient and flexural strength that were know to be readily achievable by CFC manufacturers.

3.1 Thermal Conductivity Requirements

A high thermal conductivity into the thickness of the tile is an important factor for the choice of material as it is the surface temperature of the plasma facing tiles that limits the operation. When CFC tiles over-heat they are likely to cause a run-away influx of carbon, a 'carbon bloom'. The design of the Mark II divertor has been based on the requirement that no tile or part thereof should be heated to more than 1600°C under the expected heat load.

3.2. Thermal Expansion Coefficient Requirements

The power handling capability of a tile in the Mark II divertor depends not only on the value of the thermal conductivity but also on the thermal expansion coefficient. This is because as a tile is exposed to a heat flux a temperature gradient will be set up and the tile will tend to bow. This will locally increase the power density still further. The optimum solution corresponds to a high thermal conductivity into the tile and a low thermal expansion along the tile.

3.3. Mechanical Strength Requirements

The divertor tiles are exposed to a variety of mechanical and thermal stresses that they must withstand. Mechanical loads are applied to the tiles due to the method of attachment and the pull down force (1 kN) as well as during disruptions when it is likely that large currents ('halo currents') pass through the tiles and interact with the magnetic field in the torus. Thermal stresses arising in the tiles will be high in particular at the intersection with the separatrix.

4. Tile Material Tests

JET undertook an extensive testing program of available (CFC) tile materials simulating the expected tile loading. The suitability of the various materials was tested empirically in order to find the best and most cost effective solution to the JET requirements including a delivery time no longer than six months. Firms were required to provide specimen tiles for testing purposes with guaranteed properties representative of those expected for the production tiles, as shown in Table 1.

JET investigated ten different tile materials including quasi uni-directional material, two-dimensional materials, and quasi three-dimensional or random materials, Fig. 3. Materials

were tested in the JET neutral beam test bed at fluxes of between 5 and 30 MW/m^2. Testing concentrated on the thermal conductivity, bowing and mechanical integrity of the tiles.

4.1. Thermal Conductivity

The surface temperature rise of the sample surface was observed with an IR camera. The camera was calibrated by comparing the signals it gave at temperatures up to 800°C with thermocouples placed in the body of the tile. The sample surfaces were also viewed with a CCD camera.

The time taken for the surface temperature to reach 1600°C was regarded as the first figure of merit for the materials, Fig. 4. This was determined for 5, 10 and 15 MW/m^2. An overview of the results is presented in Table 2.

1D and 2D modelling was performed to try to fit the curves generated by the I.R camera. Typically, when the surface effect (see point 4.4) was subtracted, a good fit was obtained between the data and the manufacturers supplied thermal conductivity.

4.2. Tile Bowing

The test piece sample holder was fitted with 10 Linear Voltage Displacement Transducers (LVDT's) to measure the bowing of the tiles during power deposition to determine whether the models used for determining the MKII performance were valid. Bowing up to 1 mm was observed in the test pieces and using Finite Element Modelling this was matched within the experimental accuracy of the data, Fig. 5.

4.3. Mechanical Integrity

The thermal tests indicated that, due to the large thermal stresses, some of the large tiles tended to crack along the fibre planes. Such cracking had previously not been seen for similar materials in smaller sizes exposed to the same power fluxes. 2D materials all cracked after one or a few pulses at ~20 MW/m^2. The quasi 3-dimensional or random materials performed well up to the maximum flux density. The cracked tiles did not fall apart during the tests and after the initial crack formation the tiles appeared to be stable.

As a result of these failures, tests were performed on tiles which were mechanically constrained against cracking by the insertion of inconel 718 tie bars, as shown in Fig. 6. Such tiles performed well with no degradation at 200 pulses at 15 MW/m^2.

4.3. Density considerations

A detailed study of DMS 704 material supplied under the contract for the MKI target plates showed a linear relationship between the thermal conductivity and the density, Fig. 7. Grouping the tiles in terms of their thermal conductivity by measuring their density allows the performance of the target plate tiles to be increased from that of the sample with the lowest conductivity to that of medium conductivity.

4.4. Hot spots

All the samples tested showed, to a greater or lesser extent, a jump in the temperature of the surface within milliseconds of power deposition, Fig. 8. This jump is due to the rapid over-heating of particles on the tile surface, which are not inherently thermally connected to the bulk of the material, to temperatures in excess of 1000°C. This effect can potentially cause a 'carbon bloom' at relatively low power loads. Graphite dust on the surface explains the effect only partially as careful cleaning in an ultrasonic bath only reduced the effect on some of the materials. Some materials exhibited the effect more strongly than other materials. The effect is clearly related to details of the material properties and manufacturing process, the surface cleanliness as well as the machining procedure used on the surface.

5. Conclusions

The power deposition tests performed at JET on large CFC tiles from a variety of manufacturers have provided support for the Mark II divertor design. In general the tests showed most of the materials to have properties within the limits specified by the manufacturer. Fig. 9 shows a summary of the data evaluated in such a way as to provide a figure of merit for the various tiles for use in the Mark II divertor. The figure shows the time it takes for the tile, or a part of it, to reach a surface temperature of 1600°C assuming a 4.5 MA plasma with a conducted power of 10MW per divertor leg and a two degree angle between the field lines and the surface of the tiles. The figure takes into account both the thermal conductivity and the thermal expansion coefficients of the materials and shows that, within the given boundary conditions, there are only small differences in the performance of tiles T2,T6, T15, T16 and T18. The tests pointed out that some tile types tend to exhibit more or larger particles on the surface which over-heat as well as the importance in the

choice of the tile surface machining method and of the tile surface cleaning. The cracking of the 2D and uni-directional tiles due to thermal stress indicated the requirement for tie bars in the tiles. The final choice of DMS 704 (T02) as the material for the Mark II divertor was made on the basis of the tests as well as on price and delivery.

Guaranteed Properties	Direction	Units	300 °C	1000 °C
Thermal conductivity	x	$Wm^{-1}K^{-1}$	>140	>75
	y,z	$Wm^{-1}K^{-1}$	>40	>25
Thermal expansion	x,y	K^{-1}	$<6x10^{-6}$	$<6x10^{-6}$
Flexural strength	in all directions	$MN\ m^{-2}$	as high as possible	as high as possible
			Room Temperature	
Porosity		%	<15	
Density		$g\ cm^{-3}$	>1.75	
Homogeneity of density		%	<+/-5	
Impurity content		ppm	<200	
Nominal Properties				
Electrical resistivity	x,y,z		to be provided	
Young modulus	x,y,z	"		
Poissons ratio	x,y,z	"		
Interlaminar shear strength		"		

Table 1 Material properties required for Mark II divertor tiles. For x, y, z directions see Fig. 5.

Test	Material name	Type	Density [g/cm^3]	250-1500°C at 5MW/m^2 [s]	250-1500°C at 10MW/m^2 [s]	300-1500°C at 15MW/m^2 [s]
T02	DMS 704	2D	1.79	11.81	2.84	1.19
T03	DMS 704	2D	1.85	12.94	4.22	1.49
T06	DMS 704 Alt2	~ 1D	1.89	15.84	5.14	1.91
T08	DMS 705P	~ 1D needled	1.73	7.79	1.98	0.86
T12	N11	~3D	1.82	9.83	2.44	0.99
T14	1002ZV22	2D	1.53	7.72	1.85	0.86
T15	1502ZV	2D	1.76	7.85	2.44	1.19
T16	1502ZV22	2D	1.73	10.30	2.54	0.99
T17	AO35	~3D	1.76	6.86	1.55	0.73
T18	MFC-1	1D	1.97		7.5	

Table 2 Overview of results of high heat flux tests on Mark II tiles.

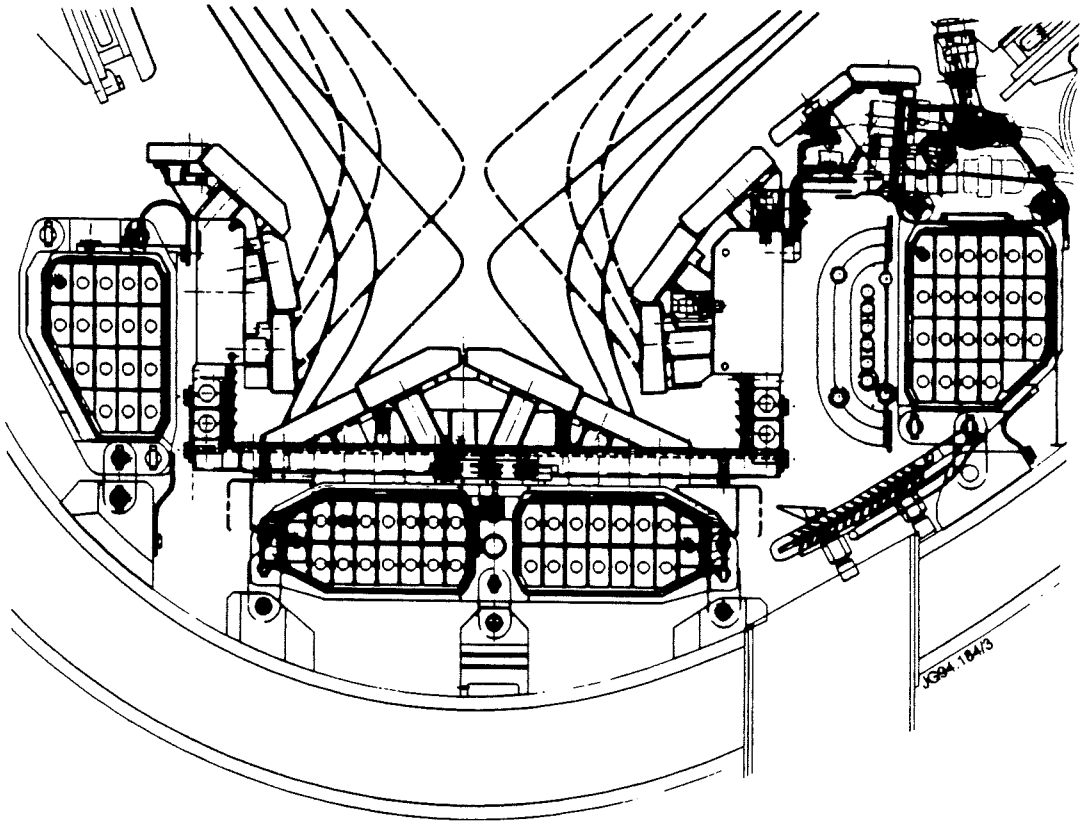

Fig. 1 Mark II divertor showing plasma configuration with separatrix on lower target tiles and side tiles.

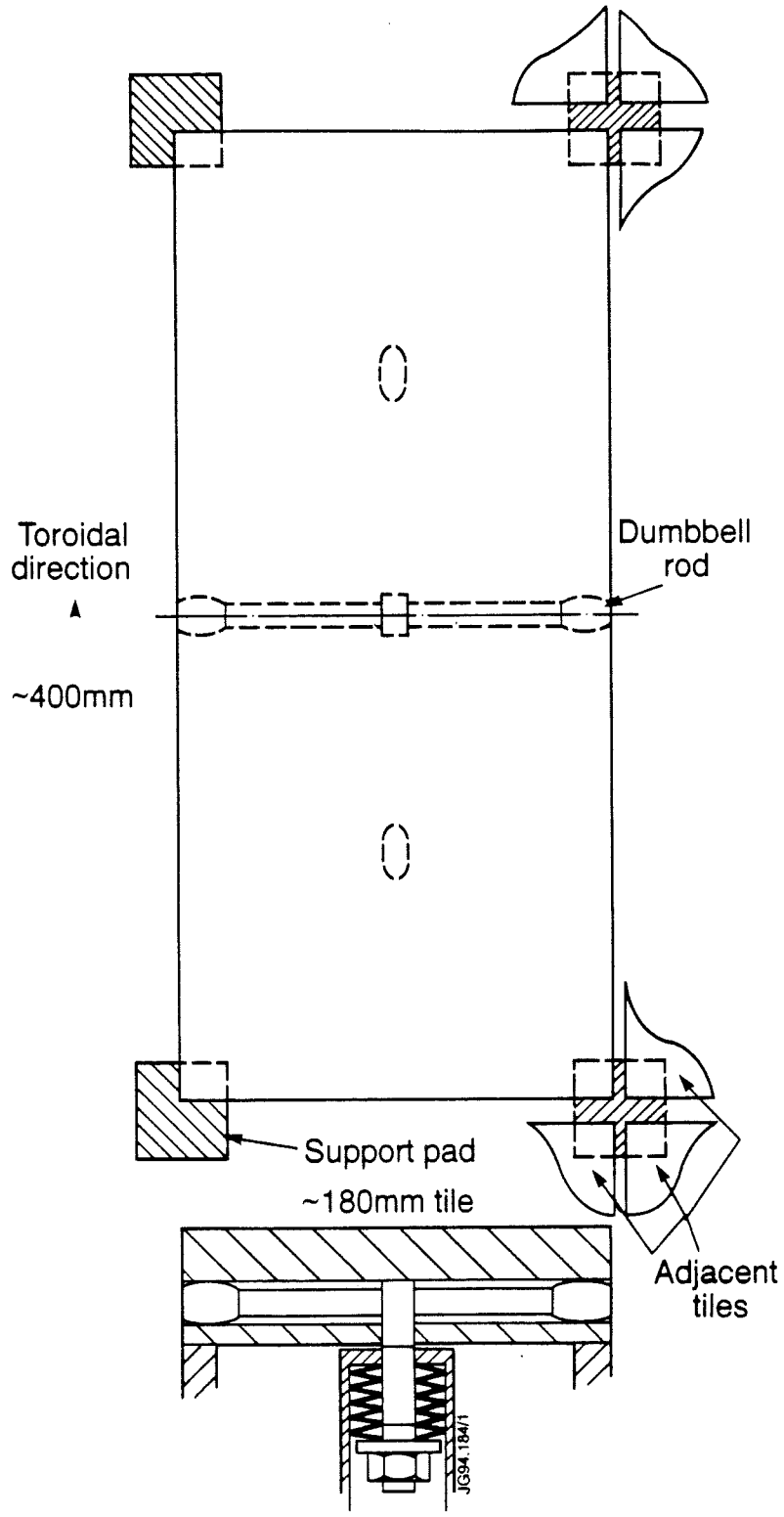

Fig. 2 Target tile support system and attachment system.

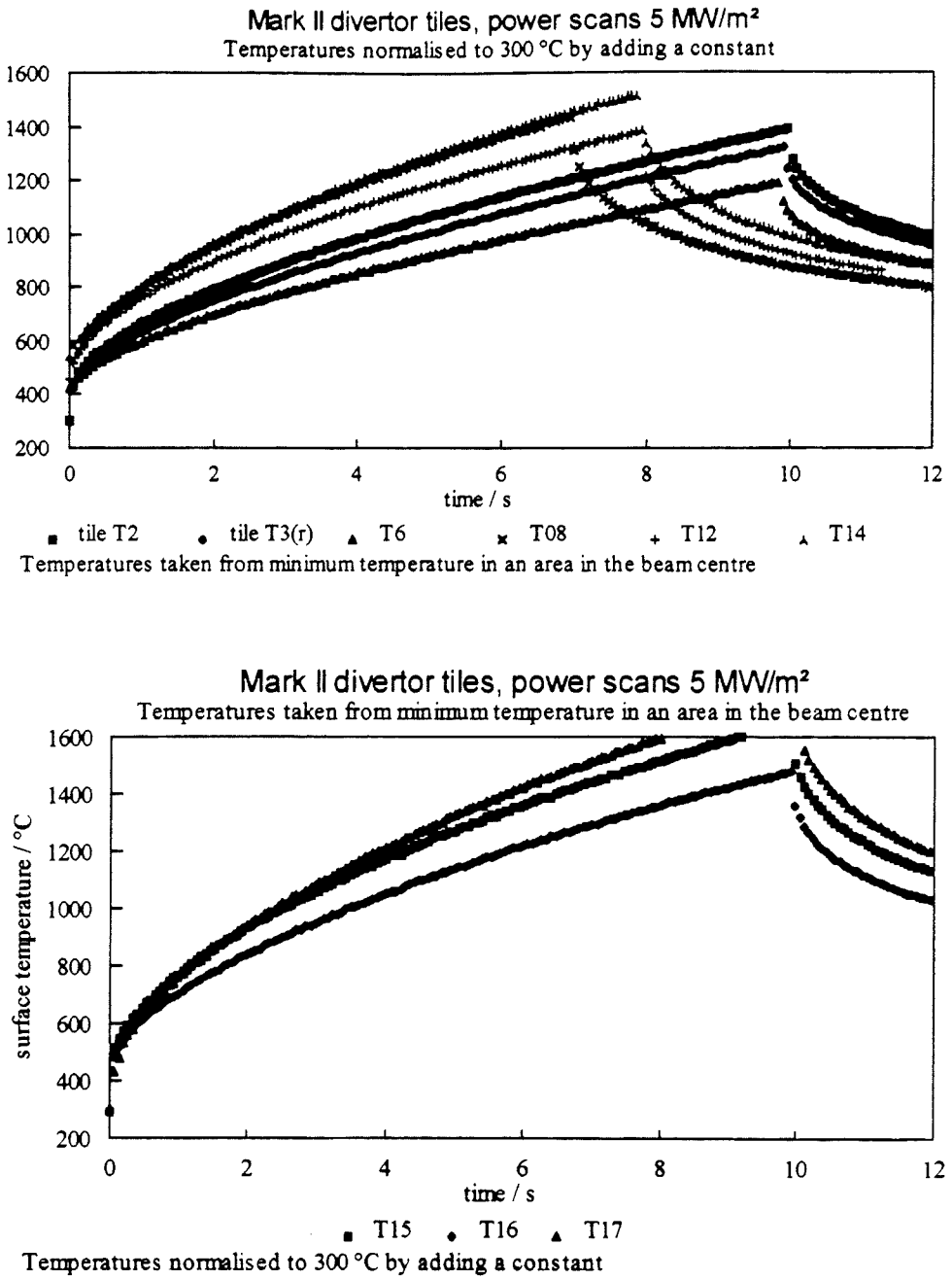

Fig. 3 Examples of power deposition scans onto Mark II divertor specimen tiles.

Sketch of required tiles and samples

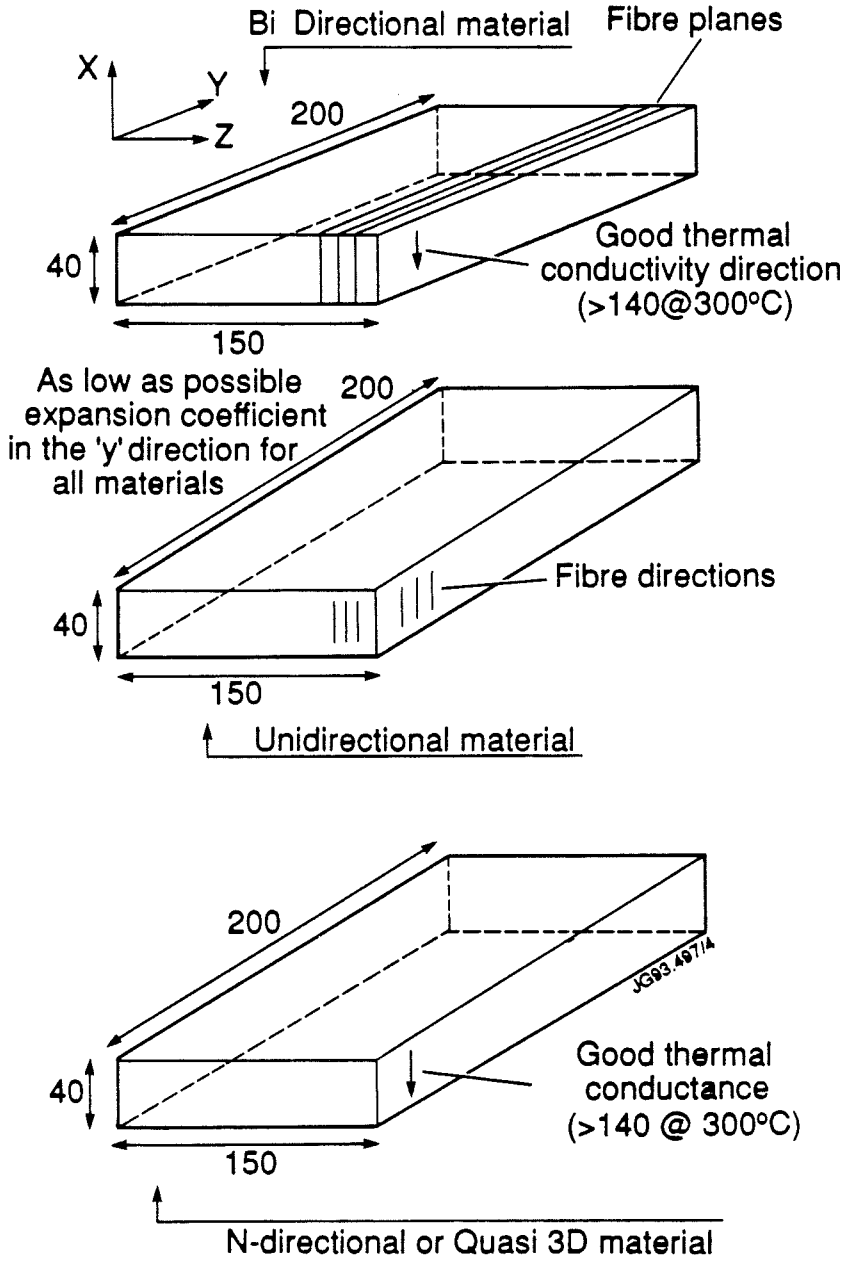

Fig. 4 Required tile material for Mark II divertor.

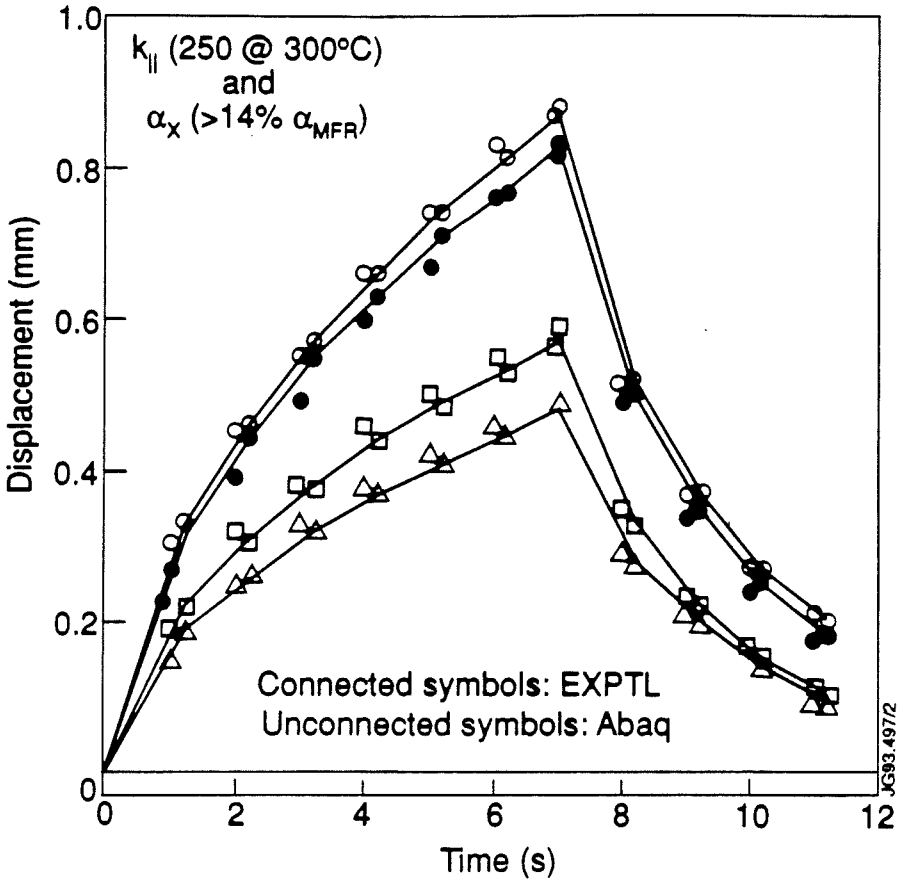

Fig. 5 Bowing measurement at several points along tile T06 exposed to 10 MW/m^2. A good fit to the model was achieved with a 14% higher value of the thermal expansion coefficient than that given by the manufacturer.

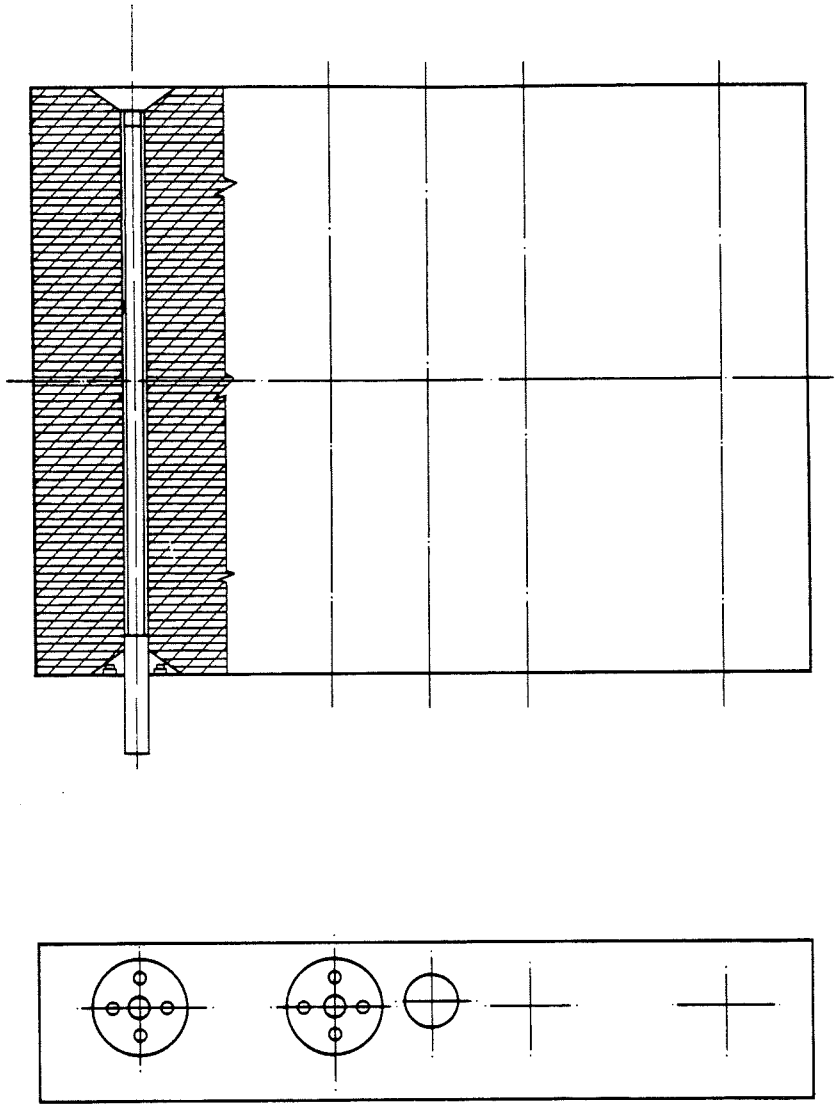

Fig. 6 CFC tile showing inconel 718 tie bars designed to mechanically constrain tile against cracking.

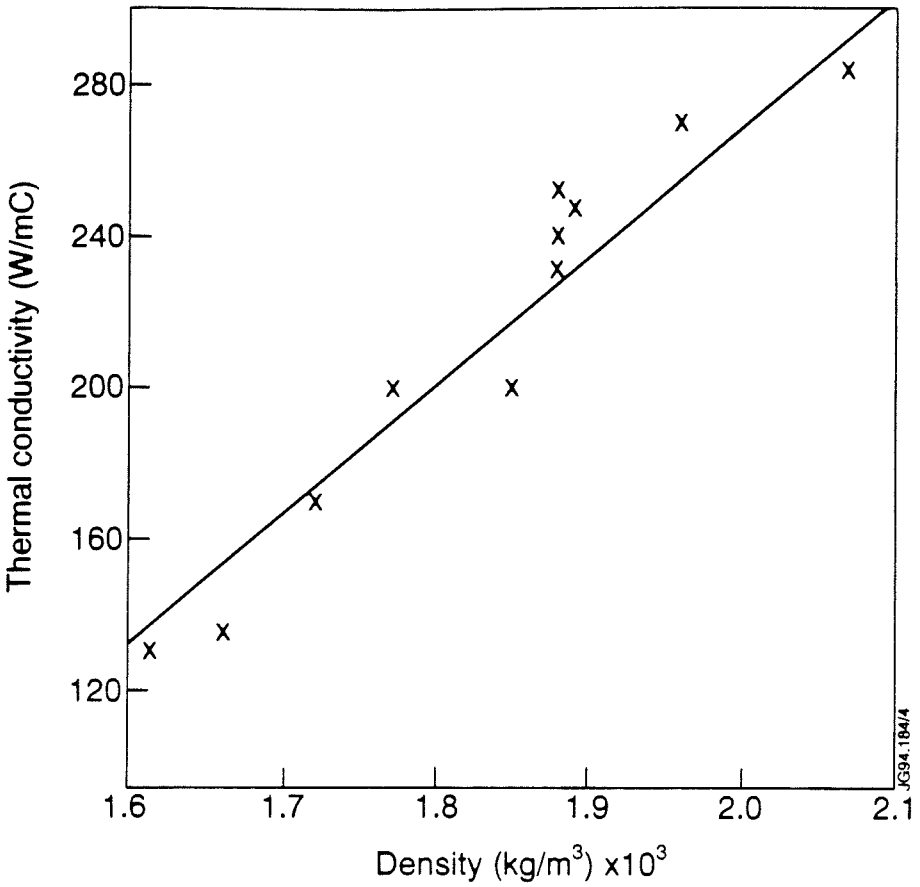

Fig. 7 Density dependence of thermal conductivity of DMS 704 used for Mark I divertor.

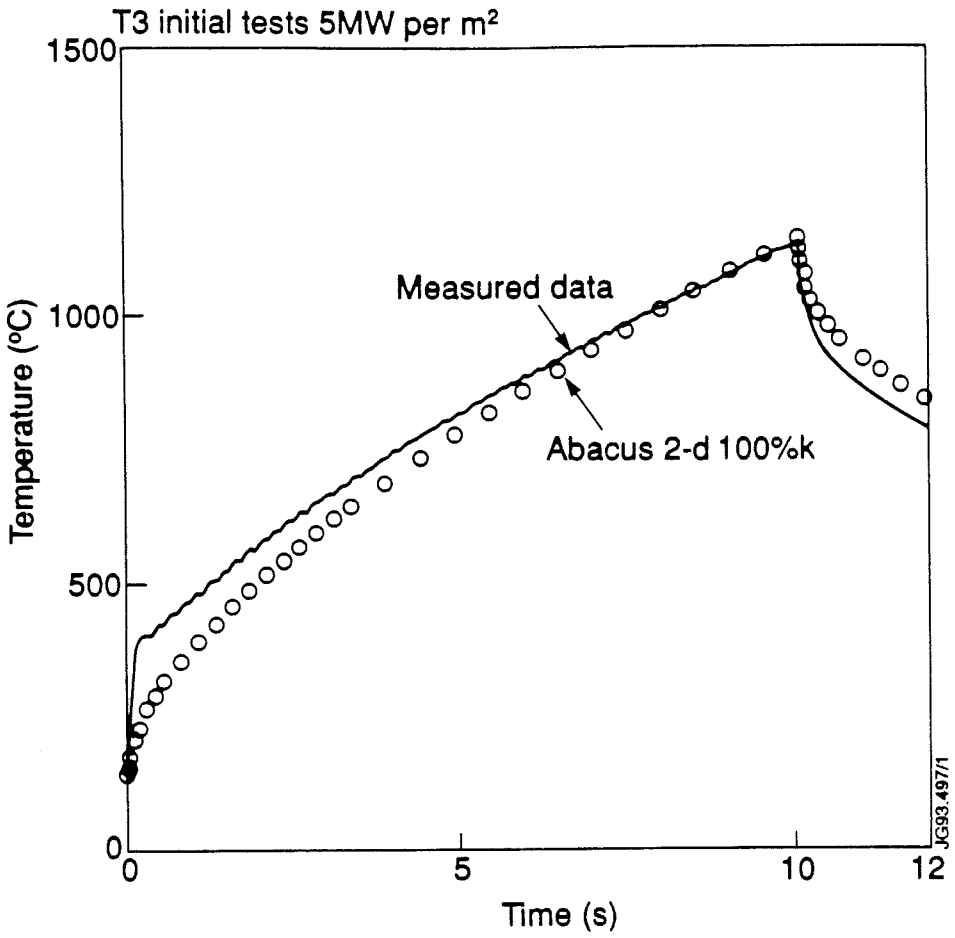

Fig. 8 5 MW test of T3 tiles showing jump in temperature at start of test compared to calculated heating rate.

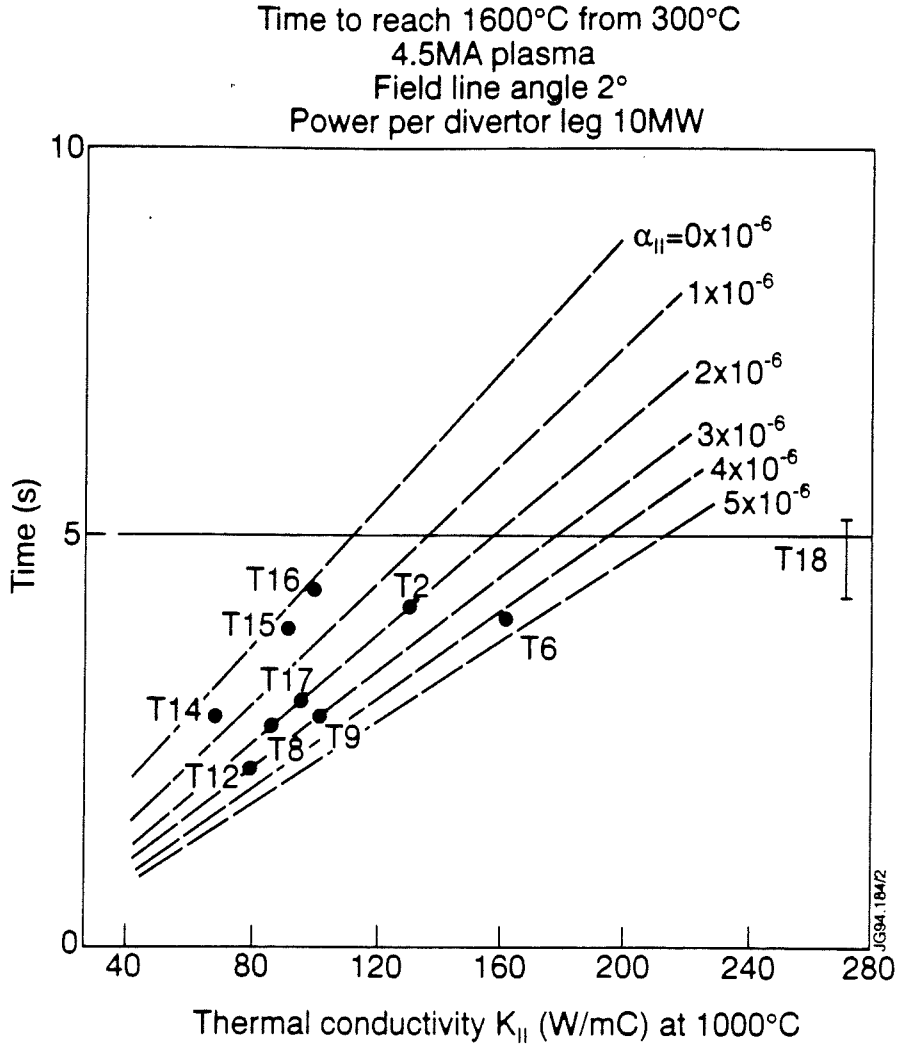

Fig. 9 Calculated time to reach 1600 °C from 300 °C for tiles exposed to a 4.5 MA plasma in JET with 10 MW per divertor leg and a field line angle of 2° to the tile surface, taking into account tile bowing.

Hydrogen Retention in the First Wall

P Andrew, M A Pick.

JET Joint Undertaking, Abingdon, Oxon, OX14 3EA.

Abstract

A general model for hydrogen retention in tokamak walls is presented which assumes that a discharge results in a hydrogen saturated layer over a large fraction of the first wall, well beyond the main limiter or divertor. The outgassing of this layer between discharges is modelled using mechanisms previously applied to ion beam experiments. This short-term outgassing rate is determined by only two parameters: 1) the number of absorption sites and 2) a parameter which describes the overall hydrogen release rate given that a quasi-equilibrium exists between atoms in solution and in traps. To explain the long term build-up of hydrogen isotopes in the first wall, it is necessary to extend the simple two-parameter model to include the effects of diffusion of hydrogen into the bulk of the material and co-deposition.

Introduction

The capacity for the plasma facing surfaces of a tokamak to retain hydrogen determines the quantity of tritium which will be lost from the fuel cycle. The purpose of this paper is to explain the hydrogen retention observed in tokamaks in terms of the physical processes which have been used to describe the behaviour of hydrogen implanted in solids.

In tokamaks, although hydrogen is observed to be lost to the first wall during a discharge (wall pumping), some of this gas is observed to be released from the walls after the discharge [1]. This effect is referred to as dynamic retention. In ion implantation experiments however, it is observed that temperatures much higher than those in a tokamak first wall are needed to release

hydrogen from graphite. In this paper, we will show that both the above observations are consistent with the model presented.

The outgassing rate ϕ as a function of time after a discharge, t, has been described as $\phi = At^{-n}$ with $n \sim 0.5 - 1.0$ [2 - 5]. It has been shown that a summation of different processes can explain such behaviour [6]. Diffusion of a uniformly distributed source from a semi-infinite wall gives $n = 0.5$ [7]. It should be noted that for a finite source, the power law must eventually breakdown as the time integrated release does not converge. It will be shown that mechanism for outgassing considered here leads to $n \simeq 0.7$.

Analysis of first wall tiles removed from tokamaks show that a large concentration of hydrogen remains in the material, even through the outgassing had been observed to virtually cease, [8, 9]. The model presented in this paper allows for the outgassing rate to decrease by orders of magnitude while the concentration in the material only varies by a factor of 2.

The Model

The two aspects of a model which must be considered separately are the mechanisms, such as diffusion and charge exchange and the actual rate constants, such as diffusion coefficients and cross sections. Because the plasma facing surfaces in tokamaks are often a mixture of materials, using material constants measured in laboratory experiments may not be the best starting point. However, if material properties are taken to be adjustable parameters we can examine which mechanisms can describe the temporal behaviour of the outgassing. Once the mechanisms have been identified, the values of the fitting parameters can be compared to material constants.

The release of hydrogen from the surfaces, as well as controlling the outgassing between discharges, has an effect during the discharge. However, to be sure we are actually studying

the effects the surfaces as opposed to the plasma, we will focus on data pertaining to periods between pulses.

i. Loading The First Wall With Hydrogen

Before the problem can be reduced to one of hydrogen in a solid, we must first consider how the surfaces are loaded with particles by the plasma. We know that the major particle flux is concentrated on a very small fraction of the total vessel wall, specifically where the surfaces intercept the scrape-off layer. In addition to this there is a relatively more uniform, but smaller flux which results from charge exchange.

If the amount of hydrogen retained is proportional to the incident fluence, then surfaces would be very non-uniformly loaded. However, it is well known from ion beam experiments that above a critical fluence the amount of hydrogen implanted saturates. For 100eV deuterium in graphite the saturation fluence would be ~3 x 10^{20} D/m^2. The fluence needed to saturate the implantation layer will be less than this since the layer will already be partially filled with hydrogen prior to a discharge. Charge exchange atoms will actually have a distribution of energies which results in the level of retention increasing weakly with fluence, instead of a fixed saturation level [10]. Calculations of charge exchange fluxes using the NIMBUS Monte-Carlo code [11] for a typical JET discharge indicate that the critical fluence for saturation is attained over ~50% of the total vessel surface area. Therefore as a first approximation, the effect of the discharge is to load the whole of the plasma facing surfaces (not just the plasma contact surfaces) with atoms to saturation. In this case, the walls of the tokamak may be treated as a single surface. That the whole wall area is available to "pump" out the plasma helps explain the observation that in JET~4 x 10^{22} D atoms ($\geq$ 10 x the plasma content) can be fuelled to a plasma with only a few square metres of direct contact area [2].

For JET discharges, it was observed that the quantity of gas pumped by the first wall during a discharge increased following the incorporation of beryllium [12]. One would not expect the

deuterium capacity of the saturated layer nor the charge exchange flux distribution to be very different under these first wall conditions. We postulate that the different behaviour arises due to different degrees of depletion of the saturated layer by outgassing between discharges.

ii) Release Of Hydrogen Between Discharges

The above concept of loading surfaces to saturation is described by the local saturation model [10, 13]. However, only recently has this model been extended to include physical processes which describe how atoms entering a saturated layer may be released [14 - 17]. Although there are some minor difference between these models, the important features are common to all of them. First it is assumed that there are two possible bound states for atoms: one in solution and one in deep traps. The exchange of atoms between traps and solution is described by

$$\frac{\partial c_t}{\partial t} = -K_{ts}c_t + K_{st}c_s\left(1 - \frac{c_t}{c_o}\right) \qquad (1)$$

where K_{ts} and K_{st} are the rate constants associated with thermal detrapping and retrapping respectively. The concentration of atoms in solution and traps are given by c_s and c_t. The finite number of traps, c_o, results in a saturation effect: $c_t < c_o$. In principle c_s will saturate at some level [16] but we will assume that c_s is always small. Loss of atoms from the whole system (traps and solution) is assumed to be due to recombination of atoms into molecules, with the recombination rate proportional to the square of the concentration of atoms in solutions:

$$\frac{\partial(c_s + c_t)}{\partial t} = -K_r c_s^2 \qquad (2)$$

where K_r is the recombination rate coefficient.

If both the detrapping and retrapping are rapid compared to the net loss from the system (i.e., each term in the RHS of Eqn. 1 is large compared to the RHS of Eqn. 2) then a quasi-equilibrium will exist between the trapped hydrogen:

$$c_s = \beta \frac{c_t}{1 - c_t / c_o} \tag{3}$$

where $\beta = \frac{K_{ts}}{K_{st}} = \beta_o \ e^{-E/KT}$ and E is the potential energy difference between solution sites and traps. The quasi-equilibrium assumption implies that release is limited by recombination, not by detrapping.

If $c = c_s + c_t \sim c_t$, then the outgassing in the absence of implantation is given by

$$-\frac{dc}{dt} = K \frac{c^2}{\left(1 - c/c_o\right)^2} \tag{4}$$

where $K = K_r \beta^2$.

The solution to the above equation for $c = c_o$ at $t = o$ is

$$Kc_o t = \frac{c_o}{c} - \frac{c}{c_o} + 2 \ln\left(\frac{c}{c_o}\right) \tag{5}$$

This is a special case of the more general equations derived by Richards et al. [18], Brice [16], and Morita et al. [17].

Using equations (4) and (5), the outgassing flux, $\phi = -Ax_o \frac{dc}{dt}$, where A and x_o are respectively the volume and depth of the implantation layer is shown in Fig.1.

In this example, $c = 0.89\ c_0$ after ~10 min., but $c \sim 0.25 c_0$ is only reached after twelve days. It is therefore misleading to think of $(Kc_0)^{-1}$ as a characteristic time for release. It is the sensitive dependence of outgassing on concentration (eqn. 4) that makes the retention of hydrogen appear static in certain conditions and dynamic in others.

Effect Of Wall Initial Conditions

In the above model, the action of the plasma over one tokamak discharge is to re-saturate the implantation layer. The quantity of gas required to fuel the plasma will simply depend on the length of time since the previous discharge. The amount of gas released after hydrogen discharges, according to the model, will always be the same since the plasma returns the wall to the same saturated condition. Fig. 2 shows the gas fuelling requirement and amount of outgassing for a sequence of similar JET discharges. The gas injection rate is controlled by feedback to give a constant plasma density, so that the fuel requirement is a measure of the wall pumping. The first discharge requires more gas input since the walls are initially more depleted of deuterium due to the extra long outgassing period. The model calculation shown in Fig. 2 reproduces the basic trends.

The number of traps used to fit the data in Fig. 2 was $Ax_0c_0 = 1.65 \times 10^{23}$ traps. This should be compared to the saturation fluence over the whole vessel surface area, $3 \times 10^{20}\ D/_m{}^2 \times 200 m^2 = 6 \times 10^{22}$ traps. The discrepancy between these two values could easily be accounted for by the uncertainty in the mean energy of the charge exchange neutrals.

He-conditioned walls are observed to pump deuterium more rapidly, but the effect is quickly lost as the wall subjected to further deuterium discharges [19]. This can be understood with the present model since helium conditioning discharges deplete the walls of hydrogen faster than thermal outgassing, providing more empty traps to pump deuterium.

Effect Of Wall Material And Temperature

Larger values of the release rate parameter, Kc_0, will result in more empty trapping sites for the next discharge, hence strong wall pumping. In the diffusion/recombination model usually applied to metals [20], the magnitude of wall pumping has the opposite dependence on the rate of recombination.

Fig.3 shows data for the fraction of the gas fuelled to a JET discharge recovered in the 540 second period following discharges. The data are grouped according to what materials made up the first wall. The curves show lines of constant gas recovery, and the corresponding values of the Kc_0 for a common number of traps ($Ax_0c_0 = 1.65 \times 10^{23}$). The effect of adding beryllium to the JET first wall has been accelerated outgassing resulting in more empty traps to pump deuterium out of the next discharge.

Eqn. 5 was fitted to isochronal anneal data [21, 22] by allowing Kc_0 to be temperature dependent: $Kc_0 \propto \exp(-1/T)$. These fits, together with values of Kc_0 measured by Morita et al., [17] are compared with the values for JET in Fig. 4. The values of Kc_0 from the isochronal anneal experiments are consistent with those for the JET all-carbon data.

Extended Sequences Of Discharges

Hydrogen is observed to build-up in the first wall, over months of operation, well beyond the implantation depth x_0. This is possible either by 1) diffusion of H atoms into the bulk or 2) growths of new material over the wall (co-deposited films) which bury previously implanted material.

i) Diffusion Of Hydrogen Atoms

Following the suggestion of Möller [15] we will consider the possibility of atoms diffusing within the material, beyond the implantation layer. This makes the problem one-dimensional and adds a third adjustable parameter, the diffusion coefficient, D:

The diffusion is taken to be sufficiently slow that no significant diffusive transport occurs during the discharge, only the relatively long periods between discharges. To account for diffusion of atoms in solution, eqn. 4 must be replaced with:

$$\frac{\partial c_i(x)}{\partial t} = - K \frac{c_i(x)c(x)}{\left(1 - \frac{c(x)}{c_o}\right)^2} + D_{eff} \frac{\partial^2}{\partial x^2} \left(\frac{c_i(x)}{1 - \frac{c(x)}{c_o}} \right) \qquad (6)$$

where $D_{eff} = \beta D$ and the subscript i denotes isotopes i and $\sum_i c_i(x) = c(x)$.

The magnitude of the diffusion coefficient is set by modelling the results of the tritium release per discharge long after limited tritium fuelling [23] (Fig. 5). The concentration of the old isotope does not drop off exponentially with increasing shot number. This is because the concentration of the old isotope in the implantation layer, although being diluted by repetitive discharges, is being replenished by diffusion from the bulk of the material. This effect has previously been noted in TFTR [24] and DITE [25] isotope exchange experiments.

ii) Co-deposition

To extend the two parameter model to include co-deposition, we add a thickness Δx of hydrogen saturated material to the surface after each discharge. The source of this material is erosion from a small minority of the total plasma-facing surface. Co-deposition is known to occur in tokamaks. The thickness of the film deposited in a single discharge, however, is smaller than the implantation depth x_o.

The amount of substrate material deposited during a discharge will be directly proportion to the incident fluence: it will not saturate in the way the retained hydrogen saturates with fluence.

However, for simplicity, the problem will be kept one dimensional when considering the effect of co-deposition.

Fig. 5 shows a calculation for a codeposited film growing $\Delta x = 0.1\ x_0$ each discharge. It was found that as soon as a layer was buried to a level $x > x_0$, hydrogen from that layer outgassed at a dramatically slower rate. Although the calculation including diffusion gives a much better fit to the JET data, co-deposition would be expected to dominate in a relatively cold walled graphite tokamak such as TFTR.

Conclusions

It is possible to understand a large variety of hydrogen release data using a two parameter model which assumes:

1) a tokamak discharge results in a H-saturated layer over a large fraction of the first wall.

2) Outgassing occurs accordings to the mechanisms usually applied to graphite. The value of the release rate parameter, Kc_0, depends on material and temperatures.

The value of Kc_0 needed to fit ischronal anneal data for graphite is in good agreement with the magnitude and time dependence of JET outgassing during its all carbon phase. The increased wall-pumping effect observed in JET upon incorporation of beryllium, is understood as a larger number of empty trays becoming available before the next discharge due to enhanced outgassing.

The two parameter model needs to be extended to include the effects of either co-deposition or diffusion to explain the gradual build-up of hydrogen deep in the material. Including diffusion gave a superior fit to outgassing of tritium from JET, yet co-deposition would be expected to dominate in a machine with cold graphite walls.

References

[1] R. Sartori, G. Saibene, D.H.J. Goodall, E. Usselmann, P. Coad and D. Holland, J. Nucl. Mater. 176 and 177 (1990) 624.

[2] J. Ehrenberg, V. Philipps, L. deKock, R.A. Causey and W.L.Hsu, J. Nucl. Mater. 176 and 177 (1990) 226.

[3] D.H.J. Goodall, P. Andrew, J. Ehrenberg, G.M. McCracken, A.T. Peacock, G. Saibene, R. Sartori, P. van Belle, J. Nucl. Mater. (PSI-10).

[4] G. Martin and G. Lewin, J. Vac. Sci. Tech. 3(1) (1965) 6.

[5] H.F. Dylla, J. Vac. Sci. Tech. A6(3) (1988) 1276.

[6] V. Philips and J. Ehrenberg, J. Vac. Sci. Tech.

[7] J. Crank, "The Mathematics of Diffusion", 2nd Ed., Clarendon (1975).

[8] J.P. Coad, R. Behrich, H. Bergsaker, J. Ehrenberg, B. Emmoth, J. Partridge, G. Saibene, R. Sartori, J.C.B. Simpson and Wen-Min Wang, J. Nucl. Mater. 162-164 (1989) 533.

[9] A.T. Peacock, J.P. Coad, F. Lama, R. Behrisch, A.P. Martinelli, B.E. Mills, M. Pick, J. Partridge, J.C.B. Simpson, and Y.K. Zhu, J. Nucl. Mater. 176 and 177 (1990) 326.

[10] S.A. Cohen and G.M. McCracken, J. Nucl. Mater. 84 (1979) 157.

[11] E. Cupini; A. de Matteis, R. Simonini, Rep. EUR XIII, 329/9, ENEA Bologna (1985).

[12] P.R. Thomas and the JET team, J. Nucl. Mater. 197 & 177 (1990)3.

[13] B.L. Doyle, W.R. Wampler, D.K. Brice and S.T. Picraux, J. Nucl. Mater. 93 and 94 (1980) 551.

[14] K.L. Wilson, R. Bastasz, R.A. Causey, D.V. Brice, B.L. Doyle, W.R. Wampler, W. Möller, B.M.V. Scherzer and T. Tanube, Supplement to Nucl. Fus. vol.,1 (1991) 31.

[15] W. Möller and B.M.U. Scherzer, J. Appl. Phys. 64(10) (1988) 4860.

[16] D.K. Brice, Nucl. Instrum. Methods, Sect. B.44 (1990) 302.

[17] K. Morita and Muto, J. Nucl. Mater. 196-198 (1992) 963.

[18] P.M. Richards, S.M. Myers, W.R. Wampler and D.M. Follstaedt, J. Appl. Phys. 65(1) (1989) 180.

[19] J. Ehrenberg et al., J. Nucl. Mater., 162-164 (1989) 63.

[20] P. Wienhold, F. Waelbroeck, J. Winter, E. Rota, T. Banno and R. Yamada, J. Nucl, Mater. 122 and 123 (1984) 1180.

[21] B.L. Doyle, W.R. Wampler adn D.K. Brice, J. Nucl. Mater. 103 and 104 (1981) 513.

[22] R. Jimbou, M. Saidoh, N. ogiwara, T. Ando, K. Morita and Y. Muto, J. Nucl. Mater. 196-198 (1992) 958.

[23] P. Andrew, J.P. Coad, J. Ehrenberg, D.H.J. Goodall, L.D. Horton, O.N. Jarvis, P.J. Lomas, M. Loughlin, G.M. McCracken, A.T.Peacock, M.A. Pick, G. Saibene, R. Sartori and P.R. Thomas, Nucl. Fus. 33 (1993) 1389.

[24] P.H. LaMarche, H.F. Dylla, P.J. McCarthy and M. Ulrickson, J. Vac. Sci. Tech. A4(3) (1986) 1198.

[25] G.M. McCracken et al., Nucl. Fus. 18 (1978) 35.

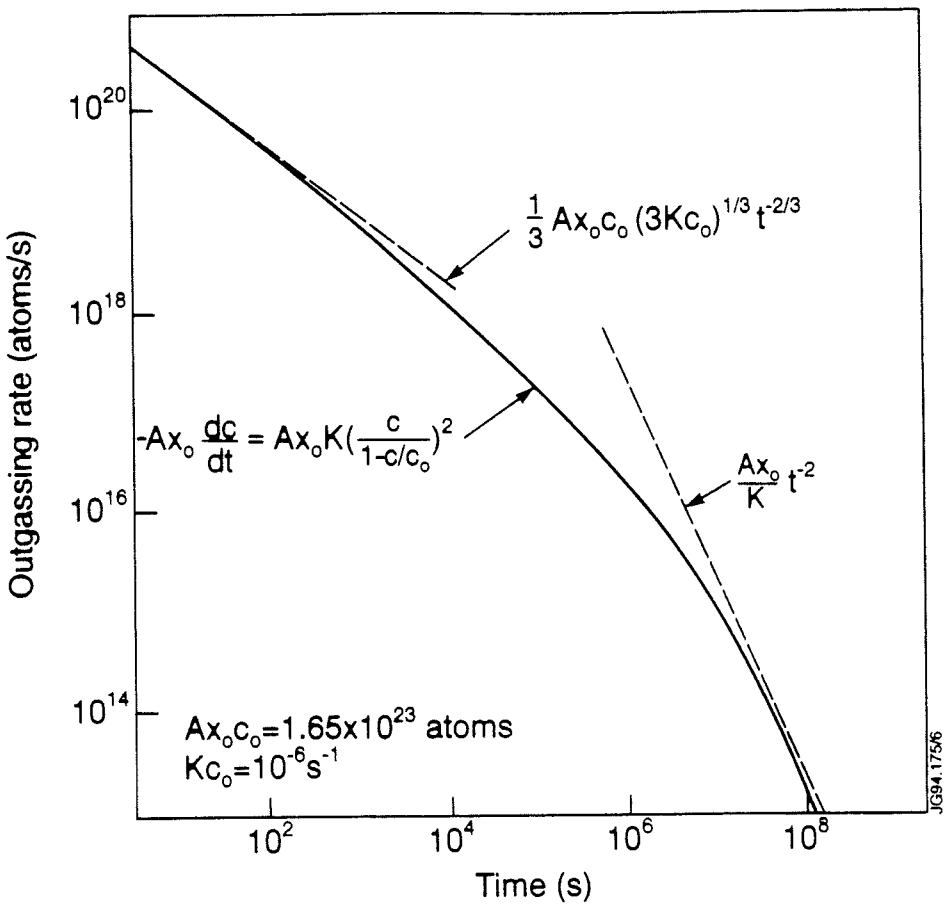

Fig. 1 Outgassing of an initially saturated surface layer as a function of time.

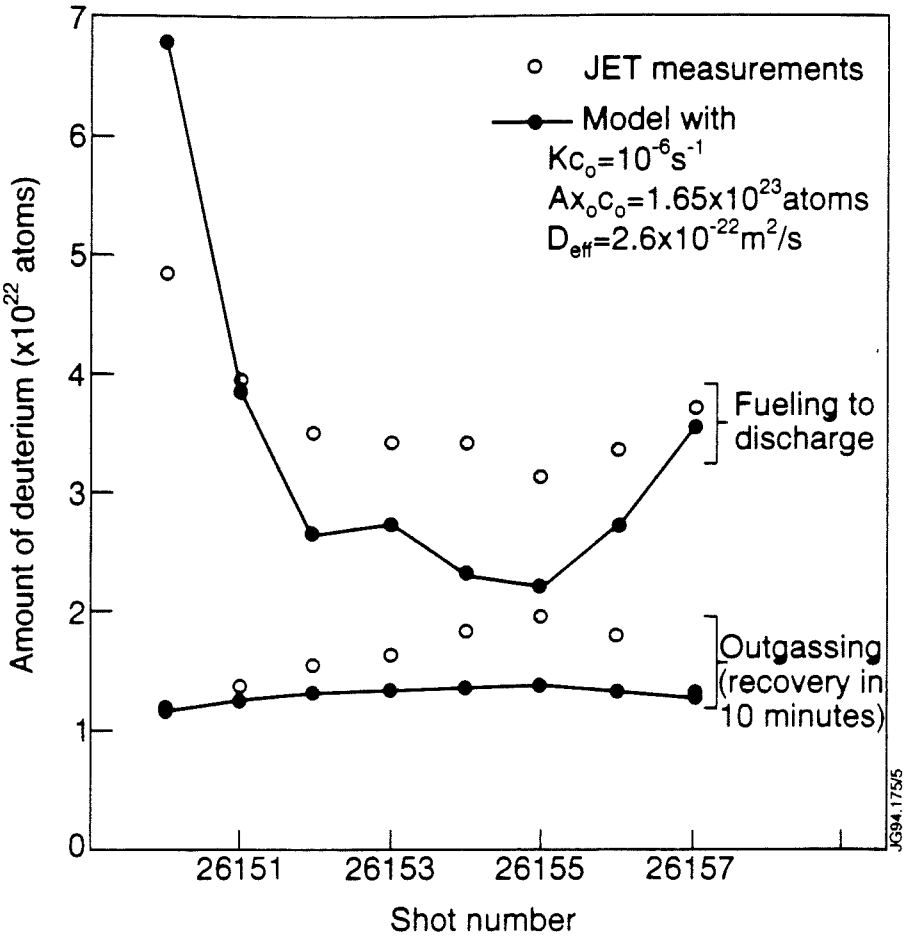

Fig. 2 The total gas input to a discharge and the gas recovery in the following 560 second period. The sequence of JET discharges starts following a 40h period without plasmas, while the time between discharges in the sequence is typically 0.5h.

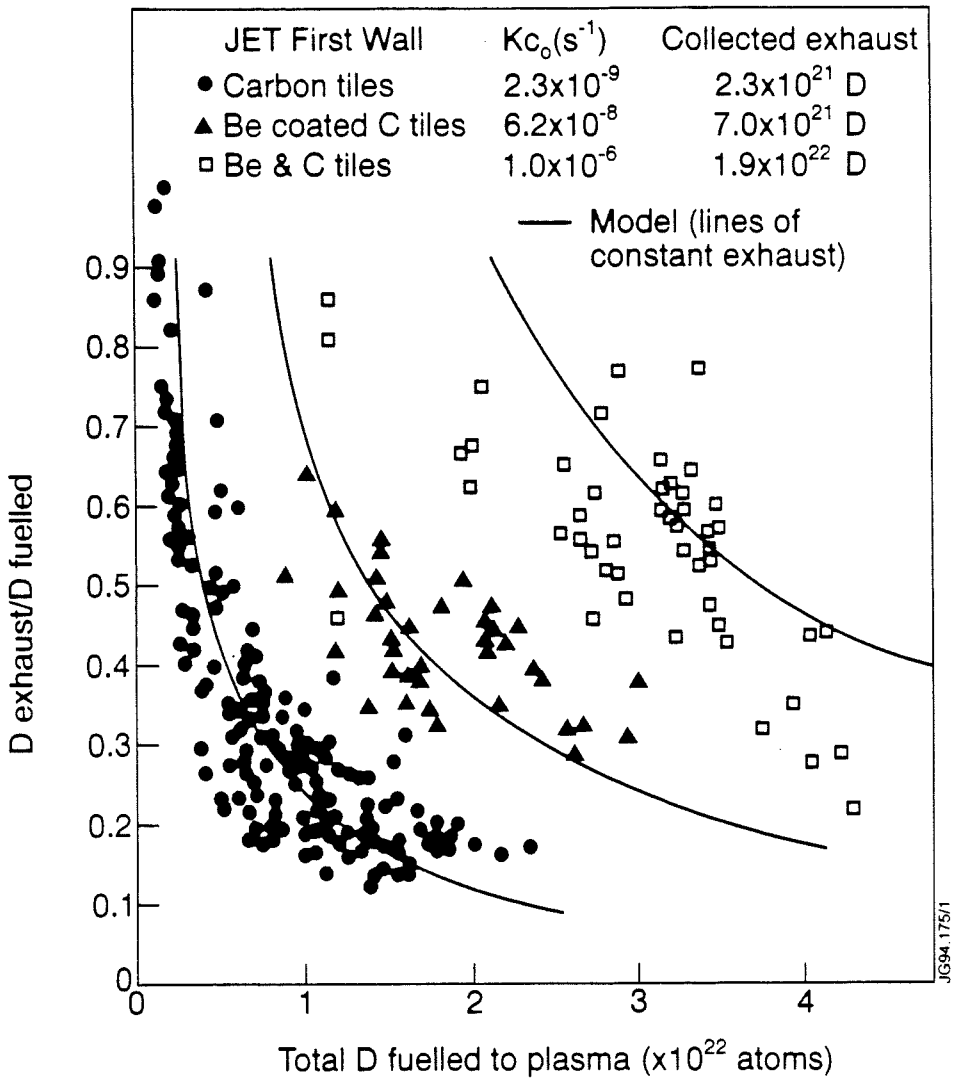

Fig. 3 JET data (Sartori et al. [1]) on the recovery of gas during the 10 minute period after the plasma (T = 300°C). A different value of Kc_0 is used to fit the data for each different wall material group (Ax_0c_0 = 1.65 x 10^{23} atoms).

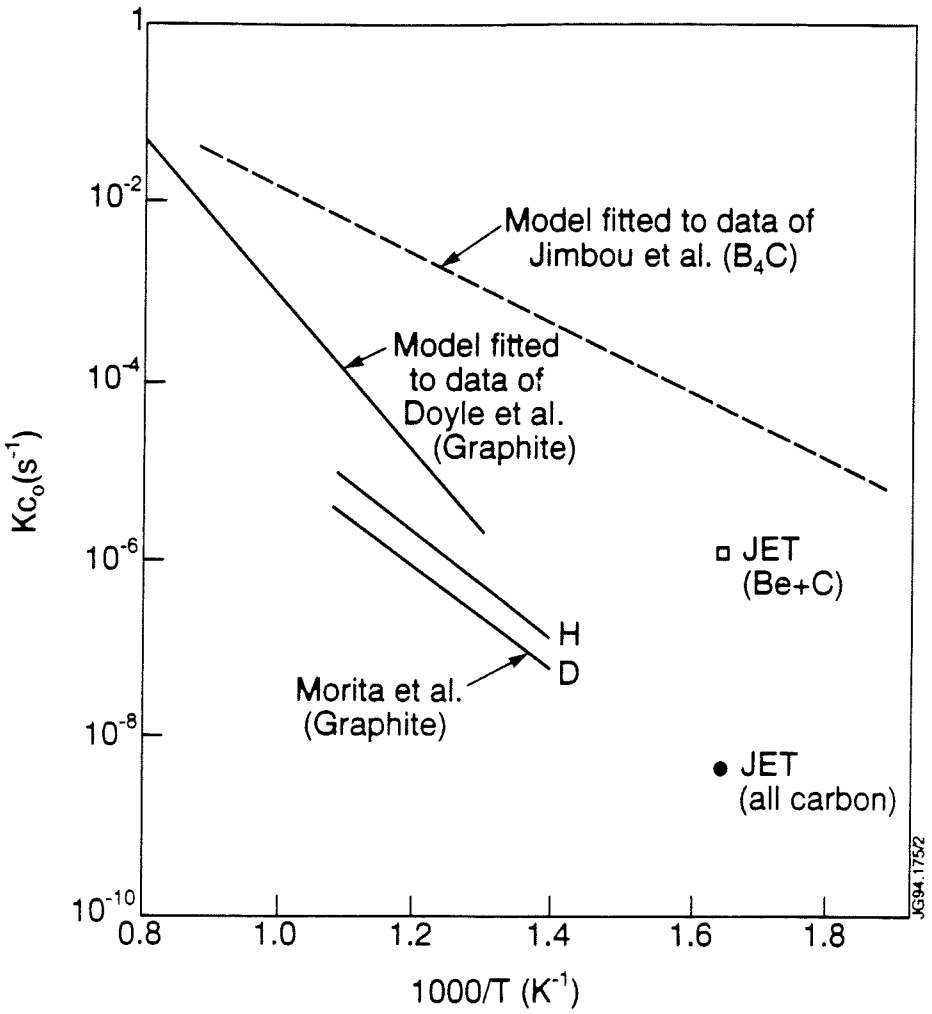

Fig. 4 Arrhenious plot of Kc_o for graphite and B_4C [22] samples saturated with D ion beams. Values for JET data (Fig. 3) shown for comparison.

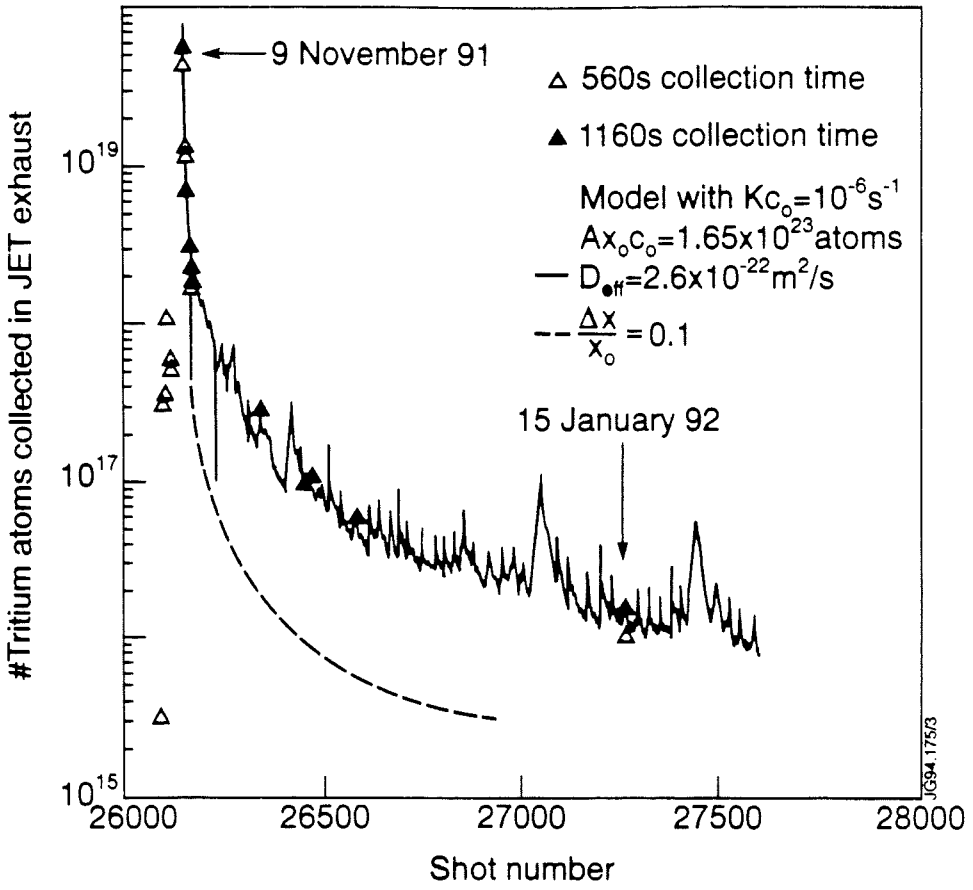

Fig. 5 Quantity of tritium in the exhaust gas following tritium fuelled discharges in JET [23]. Two model calculations are shown: 1) Diffusion included. 2) Co-deposition included.

Determination of JET Scrape-Off Layer Transport Coefficients using an Interpretive "Onion-Skin" Plasma Model

R D Monk[1], L D Horton, A Loarte, G F Matthews, P C Stangeby[2].

JET Joint Undertaking, Abingdon, Oxon, OX14 3EA.
[1] Department of Physics, Royal Holloway University of London, Surrey, TW20 0EX, UK.
[2] Institute for Aerospace Studies, University of Toronto, Downsview, Ontario, M3H 5T6, Canada.

Currently there is much interest in the application of sophisticated 2D codes to model the scrape-off layer (SOL) plasma in divertor tokamaks. These models generate the plasma solution at the divertor target starting from boundary conditions defined on a closed flux surface near the separatrix. An alternative approach, used within the DIVIMP code [1], is to anchor the boundary conditions at the divertor target using experimental Langmuir probe measurements and then solve the 1D fluid equations along each flux tube in the SOL generating an "onion-skin" model. Interaction of the plasma with recycled neutrals is included by coupling to a 2D neutral transport code. Such a model has been applied to analyse the SOL plasma transport in JET divertor discharges from the previous experimental campaign. Following the approach of Shimizu et al. [2], the radial variation of the anomalous cross-field transport coefficients ($D_\perp, \chi_\perp$) are evaluated over a range of discharges and compared with results from a 2D predictive code. In addition, preliminary divertor Langmuir probe measurements from the new pumped divertor phase of JET will be presented.

1. Introduction

In recent years much effort has been devoted to applying sophisticated two-dimensional fluid codes to model the tokamak scrape-off layer (SOL) plasma [3]. This approach relies upon specifying the boundary conditions on a closed flux surface near the separatrix and assuming values for the anomalous cross-field transport coefficients. Results from the model can then be compared with experimental data, the code assumptions varied, and iterated until good agreement is obtained.

An alternative approach, central to the plasma model used within the DIVIMP (**Div**ertor **Imp**urity) code [1], is to define the boundary conditions at the divertor target using experimental Langmuir probe data. The fluid equations are then solved in one-

dimension along each flux tube assuming that the plasma transport is dominated by flow parallel to the magnetic field lines. Interaction of the plasma with recycled neutral particles and the associated source terms are included by coupling to a 2-D neutral transport code. By repeating this procedure over all the SOL flux tubes, one then constructs a pseudo-2D model that resembles an "onion skin" (O-S). Several advantages of this interpretative modelling approach over the conventional predictive approach become apparent :-

- Uncertainty at the most physically important and numerically sensitive end of the system is minimised.
- Cross-field transport is implicitly included in the experimental data used to define the boundary conditions.
- Convergent solutions are rapidly obtained since the plasma conditions at the divertor plate (the main source of recycled neutrals) are fixed.

2. The Interpretative "Onion-Skin" Plasma Model

The one-dimensional plasma model is based upon the steady-state Braginskii conservation equations [4] for classical transport parallel to the magnetic field with the following assumptions :-

- Electron and ion temperatures are equal.
- Ion viscosity and momentum sources are neglected.
- Heat transport is dominated by electron conduction.

Boundary conditions are provided by Langmuir probes ($T_e^{target}, n_e^{target}$) at the divertor target and the parallel heat flux to the divertor target is calculated using the standard sheath condition $q_{\parallel}^{target} = 7 n_e^{target} c_s k T_e^{target}$ where c_s is the ion acoustic sound speed. The conservation equations are integrated and numerically solved for $T(s), n(s)$ and $v(s)$ along each flux tube. The plasma model is generated on a non-orthogonal mesh which is derived from the MHD calculation of JET magnetic equilibria.

NIMBUS [5], the full 2D Monte Carlo neutral transport code, is used to define the spatial distribution of ionisation sources due to recycled particles. Real wall geometry

is used and perfect recycling is assumed. The plasma model is iterated with the NIMBUS code to solve the continuity equation for the particle source terms. Figure 1 illustrates that, following the initial analytic approximation to the ionisation distribution, the convergence is very rapid and requires few iterations compared to the predictive codes. Fast convergence is obtained because, unlike the predicitive codes, the particle flux to the divertor target plates (the main source of recycled neutrals) is fixed. At present, the energy source terms due to ionisation are not iterated with the energy conservation equation for the calculation of the temperature profile. Both inboard and outboard sides of the plasma are solved separately by imposing stagnation of flow velocity at the point midway along the field lines connecting the divertor targets.

3. Experimental Measurements

Given that the modelling approach relies upon fixing the boundary conditions at the divertor target good Langmuir probe measurements are required. Table 1 outlines the discharges [6] selected for this study and the corresponding global plasma parameters. All the discharges were carried out in hydrogen with an upper x-point configuration (carbon fibre target plates) and 3MA plasma current. Unfortunately, CCD camera information on divertor particle fluxes or reciprocating probe SOL profiles were not available during these discharges. It is estimated that the spatial agreement between the probes and equilibrium reconstruction is $\leq 1cm$ at the divertor target [7]. However, one should also be aware of the following difficulties with Langmuir probe measurements

- Electron density is calculated using the assumption that $T_i = T_e$.
- Projected area may be uncertain for some probes due to erosion by the plasma.
- During H-mode discharges the probes underestimate the power deposited to the divertor target [8].

4. Model Results

Following Loarte and Harbour [9], exponential profiles are fitted to the Langmuir probe data in midplane flux co-ordinates and then mapped back onto the target

resulting in Gaussian profiles. These are then used as input to the code which uses approximately 15 minutes of computational time on a dual-processor IBM 3090 to generate the plasma model. This compares with typical computational times of >1hr to obtain convergence using the EDGE2D/U [10] predictive code. Profiles of electron temperature and density for the H-mode discharge #24174 are illustrated in figure 2. The radial profiles are plotted in midplane co-ordinates and the profiles along the field line are for the first flux tube outside the separatrix.

5. Calculation of the SOL Transport Coefficients

In moving toward next-step tokamak devices it is important to have more information on the scaling of cross-field transport in the SOL, particularly the anomalous heat diffusion coefficient ($\chi_\perp$) which influences the distribution of power deposited at the divertor target. Direct calculation of the transport coefficients (particularly $D_\perp$) from the width of the SOL relies upon there being negligible particle sources due to ionisation, which is a poor assumption for divertor tokamaks.

As demonstrated by Shimizu et al. [2], the O-S model provides a useful means by which the cross-field heat transport coefficient can be estimated. The technique is illustrated by considering the balance of energy or particles in the flux tubes ($i = 1 \rightarrow n$) adjacent to the separatrix, see figure 3. Assuming that volume energy losses in the SOL can be neglected, the total heat flow crossing the separatrix, $Q_\perp(0)$, is equal to the sum of the parallel heat fluxes in the magnetic flux tubes.

$$Q_\perp(0) = \sum_{i=1}^{n} Q_\parallel(i) \tag{1}$$

Therefore, the perpendicular heat flux flowing from the first tube outside the separatrix to the second is given by $Q_\perp(1) = Q_\perp(0) - Q_\parallel(1)$. This cross-field transport is driven by a temperature gradient and associated heat diffusion coefficient such that

$$\chi_\perp(1) = \frac{Q_\perp(1)}{A_{surf}\, 0.5(n_1 + n_2)} \left(\frac{(T_1 - T_2)}{\Delta r} \right)^{-1} \tag{2}$$

where Δr is the radial separation between the flux tubes and A_{surf} is the surface area of the plasma. However, to extend the technique and evaluate the particle diffusion coefficient ($D_\perp$), the neutral sources within the SOL cannot be ignored and must be used to evaluate the particle flux crossing the separatrix

$$\Gamma_\perp(0) = \sum_{i=1}^{n} \{\Gamma_\parallel(i) - S_{ion}(i)\} \tag{3}$$

where $\Gamma_\parallel(i)$ is the particle flux to the divertor target, and $S_{ion}(i)$ is the integrated particle source due to recycled neutrals within the flux tube. The perpendicular particle fluxes passing between the flux tubes is then calculated as for the heat flux (see above), and applying Fick's law

$$D_\perp(1) = \frac{\Gamma_\perp(1)}{A_{surf}} \left(\frac{(n_1 - n_2)}{\Delta r} \right)^{-1} \tag{4}$$

The radial variation of these transport coefficients can be determined by repeating the above procedure for the remaining flux tubes. Considering the m'th radial value (from $m = 1$ to $n-1$), equations (2) and (4) can be generalised to

$$\chi_\perp(m) = \frac{\sum_{i=m+1}^{n} Q_\parallel(i)}{A_{surf}\, 0.5(n_m + n_{m+1})} \left(\frac{(T_m - T_{m+1})}{\Delta r} \right)^{-1} \tag{5}$$

$$D_\perp(m) = \frac{\sum_{i=m+1}^{n} (\Gamma_\parallel(i) - S_{ion}(i))}{A_{surf}} \left(\frac{(n_m - n_{m+1})}{\Delta r} \right)^{-1} \tag{6}$$

The resulting radial profiles of $D_\perp, \chi_\perp$ are shown in figure 4 for pulse #24174 during L-mode and H-mode regimes. The values are small and appear to be radially constant taking into account the uncertainties involved in the calculation.

In determining the cross-field transport coefficients, two methods of calculating the density and temperature gradient have been employed :-

- Taking the gradient at the respective midplane such that the diffusion coefficients $(\hat{D}_\perp, \hat{\chi}_\perp)$ are effectively constant in magnetic flux co-ordinates .
- Taking the average gradient between adjacent flux tubes around the main plasma so that the diffusion coefficents $(D_\perp, \chi_\perp)$ are sensitive to the variation in the radial separation of the flux surfaces .

Using the first method we obtain comparable results (see table 2) to the transport coefficients required by Loarte et al. [11] to model a similar subset of JET discharges using the full 2D predictive code, EDGE2D/U (outer side only). Applying the second gradient calculation method yields transport coefficients that are approximately twice as large as the midplane values (i.e. $D_\perp, \chi_\perp \sim 2(\hat{D}_\perp, \hat{\chi}_\perp)$), also in agreement with reference [11].

6. Conclusions

"Onion-skin" modelling is a potentially useful approach for interpretative analysis of the scrape-off layer plasma using experimental data for the boundary conditions. Due to the rapid convergence of the code solution, the computational times are greatly reduced compared to the full 2-D predictive code calculations. Cross-field transport coefficients are evaluated for JET divertor discharges and found to be small for all confinement regimes, particularly in H-mode discharges (over one order of magnitude smaller than Bohm scaling) and appear to be radially constant. The values are in good agreement with those required to match similar experimental data using a full 2D predictive fluid code [11]. The transport coefficients are calculated to be typically 2-4 times larger on the inner side of the plasma than on the outer side (particularly for $D_\perp$). This is associated with the broader scrape-off width observed on the inner side [12]. At present this phenomenom is not well understood and further experimental measurements are required.

7. Future Work

Improvements planned for the 1D plasma model include :-

- Separate Ion and Electron temperatures with energy equipartition
- Fully self-consistent treatment of hydrogenic and impurity radiation.

which will be implemented in conjunction with work to establish the limits of validity for the technique using simulated probe data from EDGE2D. Clearly, in the event of volume recombination at the divertor, the boundary conditions cannot be defined by target Langmuir probes, but it may be possible to use upstream profiles from other diagnostics (such as reciprocating probes or Lithium beams). However, in less extreme divertor regimes, such as high recycling, the two-point model illustrates the advantage in defining the boundary conditions at the divertor target from which the calculated upstream parameters are relatively insensitive [13].

During the installation of the JET pumped divertor many new and upgraded diagnostic systems have been implemented. These will allow the detailed comparison of SOL and divertor parameters to cross-check against the OS model. In addition, the new in-vessel divertor coils are routinely used to sweep the plasma across the target to reduce the average power density with the additional benefit of providing high resolution profiles, see figure 5, for the large array of fixed single/triple Langmuir probes. Such measurements will prove invaluable for defining the boundary conditions for model calculations without the requirement to fit analytic profiles.

Acknowledgements

RDM acknowledges financial support from the Engineering and Physical Sciences Research Council and the JET Joint Undertaking.

References

[1] P. C. Stangeby, J. D. Elder, J. Nucl. Mat. **196-198** (1992) 258
[2] K. Shimizu, K. Itami, H. Kubo, N. Asakura and M. Shimada, J. Nucl. Mat. **196-198** (1992) 258
[3] D. Reiter, J. Nucl, Mats **196-198** (1992) 80
[4] S. I. Braginskii, in Reviews of Plasma Physics (Consultants Bureau, New York, 1965), Vol I, 205
[5] E. Cupini, A. De Matteis, R. Simonini , NET Report EUR XII-324/9 (1984)

[6] P. J. Harbour, et al., J. Nucl Mat. **196-198** (1992) 386
[7] D. P. O'Brien, J. J. Ellis, J. Lingertat, Nucl. Fusion **33** (1993) 467
[8] G. Vlases and The JET Team, Proc. 20th Conf. on Plasma Physics and Controlled Nuclear Fusion Research, Würzburg, 1992, IAEA-CN-56/A-5-1
[9] A. Loarte, P. J. Harbour, Nucl. Fusion **32** (1992) 681
[10] A. Taroni, G. Corrigan, R. Simonini, J. Spence and G. Vlases, Contrib. Plasma Phys. **34** (1994) 448
[11] A. Loarte, et al., this conference (PSI-11).
[12] P. J. Harbour and A. Loarte, JET-P(93) 96
[13] P. C. Stangeby, Institute for Aerospace Studies, University of Toronto, Private communication, 1993.

Pulse No.	Time (s)	Confinement Regime	Bϕ (T)	$\langle n_e \rangle$ ($10^{19} m^{-3}$)	P_{INPUT} (MW)	P_{SOL} (MW)	P_{RAD}^{DIV} (MW)
24165	52.3 - 52.7	Ohmic	3.2	1.2	1.6	1.2	0.2
24145	55.0 - 55.5	Ohmic	2.9	2.0	1.8	1.9	0.6
24175	53.2 - 53.8	L - Mode	2.1	1.1	5.5	4.9	0.4
24174	52.0 - 52.2	L - Mode	2.1	1.2	14.0	8.8	0.3
24171	52.5 - 52.9	H - Mode	2.1	2.3	8.0	4.2	0.3
24174	52.7 - 53.0	H- Mode	2.1	2.1	14.0	7.3	0.3

Table 1 : Plasma Parameters for the JET Single Null Divertor Discharges Modelled

Discharge	Inner Side		Outer Side	
	$\hat{D}_\perp$ $[m^2 s^{-1}]$	$\hat{\chi}_\perp$ $[m^2 s^{-1}]$	$\hat{D}_\perp$ $[m^2 s^{-1}]$	$\hat{\chi}_\perp$ $[m^2 s^{-1}]$
#24165 Ohmic	0.42	0.76	0.11 (0.1)	0.70 (0.5)
#24145 Ohmic	0.22	0.50	0.10	0.51
#24175 L-Mode	0.30	1.71	0.12 (0.2)	0.65 (0.5)
#24174 L-Mode	0.71	3.10	0.15	0.92
#24171 H-Mode	0.11	1.24	0.06 (0.05)	0.36 (0.25)
#24174 H-Mode	0.10	0.56	0.05	0.35

Table 2 : Averaged Radial Values of the Particle and Heat Diffusion coefficients (Corresponding values determined by Loarte et al. using EDGE2D/U [11] are shown in brackets).

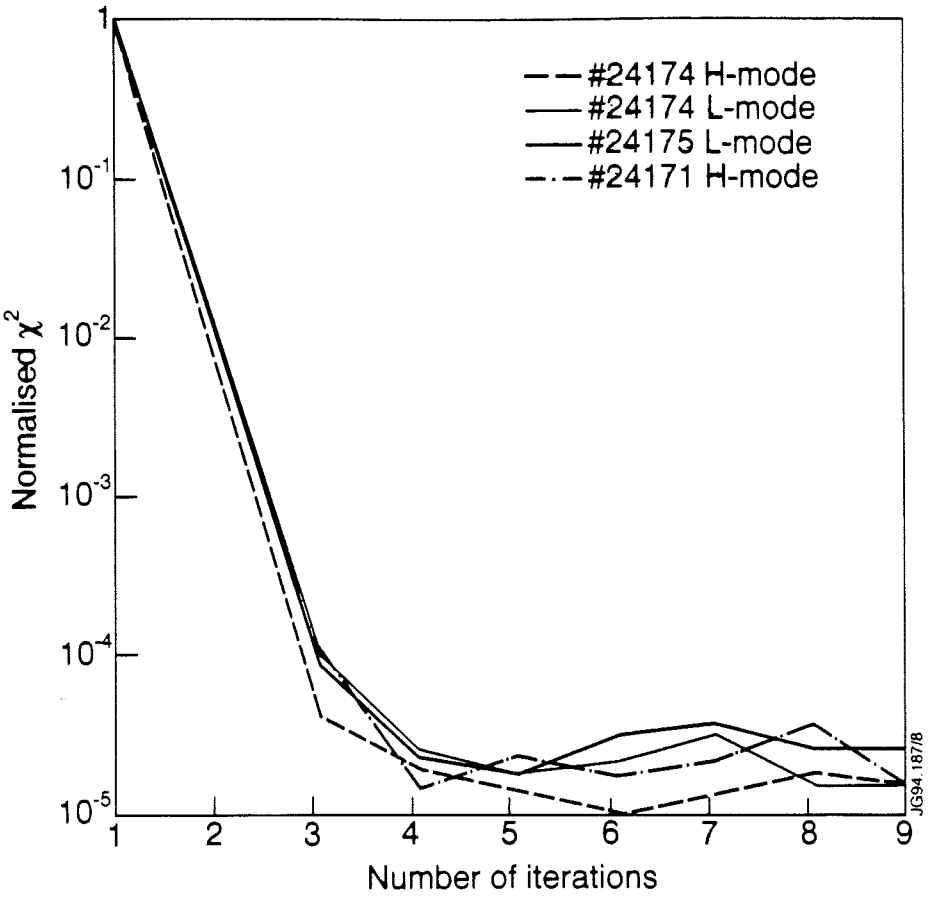

Figure 1 : Normalised Chi-squared variation of electron density over all the SOL mesh points during iteration of the plasma model with the NIMBUS neutral transport code.

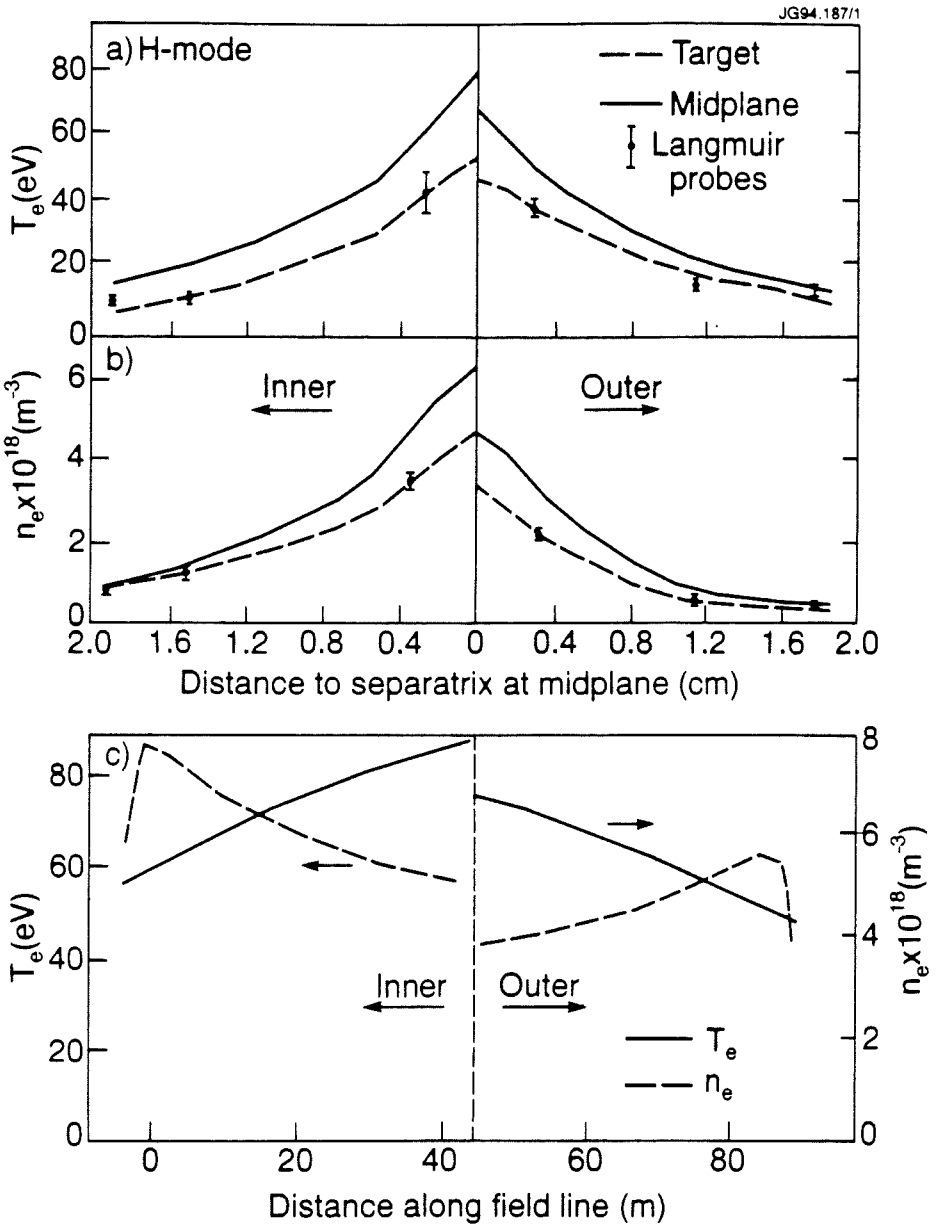

Figure 2 : H-Mode #24174 (a) Measured divertor target and modelled midplane profiles of electron temperature. (b) Measured divertor target and calculated midplane profiles of electron density. (c) Modelled profiles of electron temperature and density along the field line nearest to the separatrix.

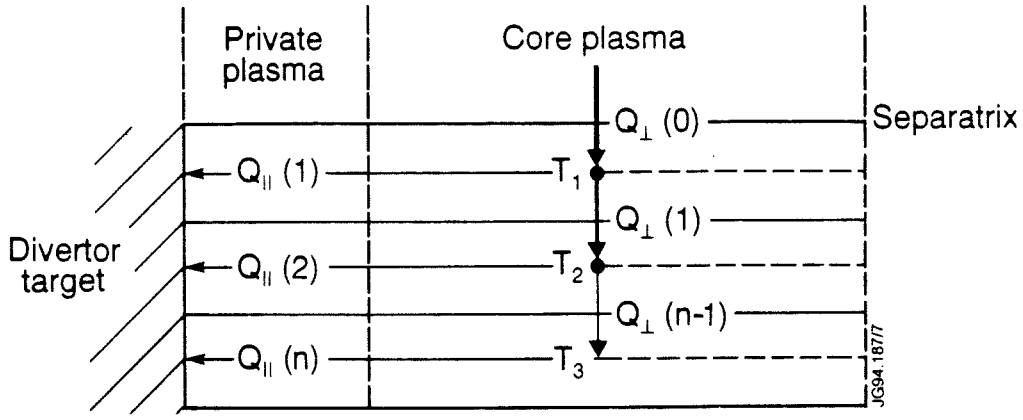

Figure 3 : Schematic of the SOL illustrating the energy balance in the magnetic flux tubes close to the separatrix.

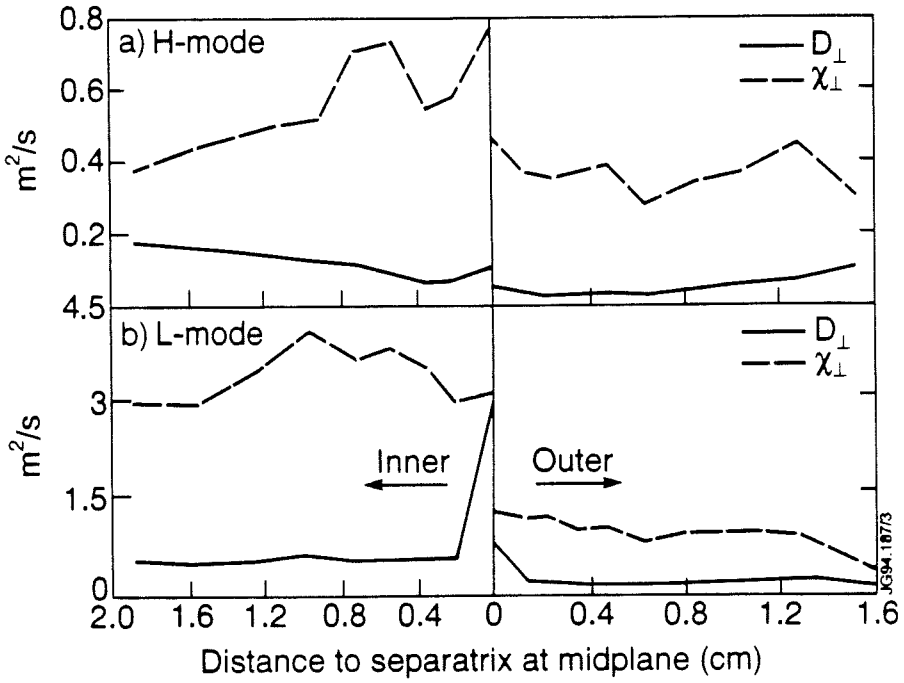

Figure 4 : Radial Variation of the Cross-Field transport coefficients (using midplane density and temperature gradients) for (a) #24174 H-Mode and (b) #24174 L-Mode

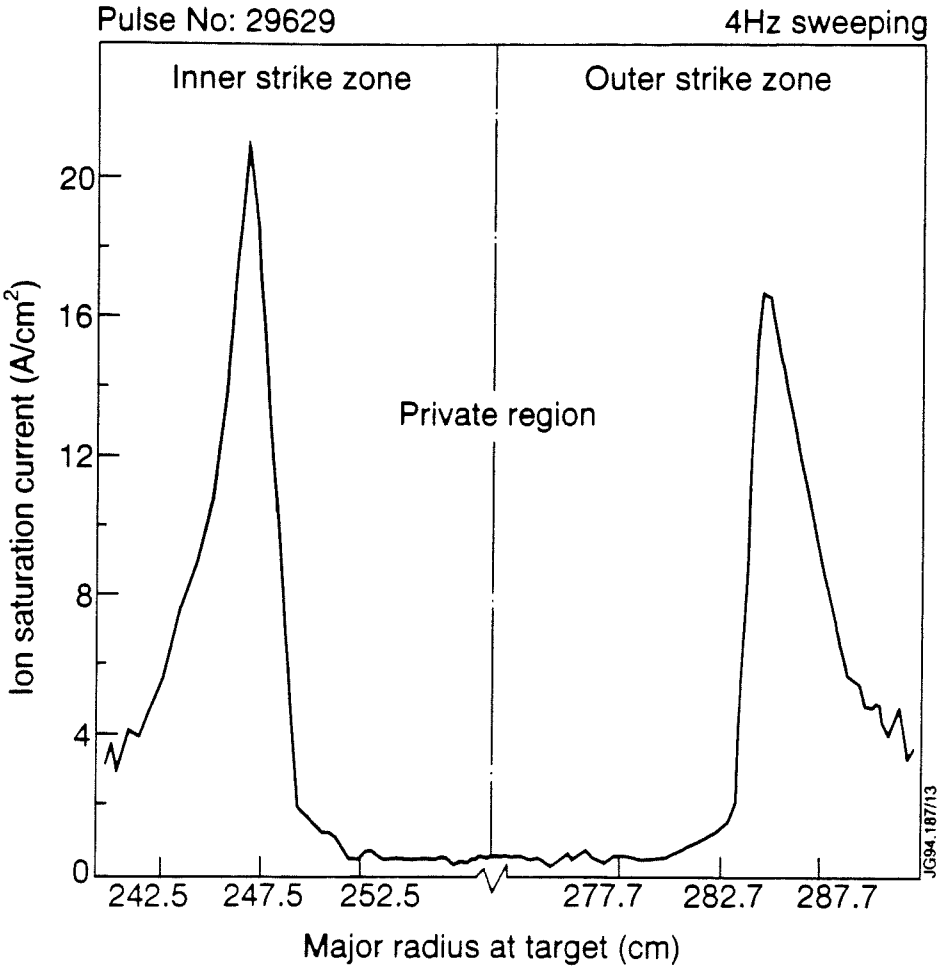

Figure 5 : Profile of Ion Flux measured at the new JET pumped divertor target during sweeping of the plasma.

The Effect of B_T Reversal on the Asymmetries between the Strike Zones in Single Null Divertor Discharges: Experiment and Theories

A V Chankin[1], S Clement, K Erents[2], P J Harbour, G Janeschitz, J Lingertat, A Loarte, G F Matthews, R Reichle, P C Stangeby[3], D D R Summers.

JET Joint Undertaking, Abingdon, Oxon, OX14 3EA.
[1] Scientific Centre "Kurchatov Institute", Institute for Nuclear Fusion, Moscow, Russia.
[2] UKAEA, Culham Laboratory, Government Division, Abingdon, Oxfordshire, UK.
[3] University of Toronto, Institute for Aerospace Studies, Ontario, Canada, M3H 5T6.

Abstract

Asymmetries in power and particle fluxes to the strike zones in single null divertor configuration are strongly affected by the toroidal field direction (see e.g. [1]). The behaviour of these asymmetries was shown to be consistent with a heuristic hypothesis of the changes in the power sharing between the two divertor branches caused by the B_T reversal: more power is delivered to the inner divertor branch when the toroidal field is reversed [2]. However, at present, there is not enough experimental evidence and theoretical justification to support this idea.

In the present paper we consider different approach to the explanation of the divertor asymmetries. We review experimental data and examine physical mechanisms which redistribute density between the two divertor branches. Amongst these is the radial $\mathbf{E}\times\mathbf{B}$ drift caused by the T_e drop along the field lines towards the target [3] and recently proposed mechanism of momentum transfer into the SOL due to edge toroidal rotation. These two mechanisms compress the plasma at the inner side in the normal B_T configuration (ion ∇B drift towards the target), and at the outer side - when the B_T is reversed. Since they do not supply additional power to the target apart from convective energy fluxes, the increased recycling and radiation at the side where the plasma is compressed should lead to a decrease in T_e. The combined effect of the above mechanisms allowes one to explain qualitatively experimental observation that plasma parameters at the target become more symmetric when the B_T is reversed.

1. Introduction

As a general trend, in single null divertor plasmas the outer divertor target receives higher power flux than the inner one (see e.g. [3]). Higher plasma temperature and power flux at the outer side is expected from the geometrical toroidal effect of the surplus of the outer circumference of the magnetic surface over the inner one. In addition, the Shafranov shift, which compresses magnetic surfaces at the outer side, and a possibility of poloidal asymmetry in plasma anomalous transport in favour of the outer side [3] can also contribute to higher power flux to the outer strike zone of the divertor target. The kynetic describtion of the edge plasma, carried out in [4], also yielded higher particle and energy fluxes to the outer side due to toroidal effects. The conservation of plasma pressure along the field lines should then cause the density rise at the inner side, leading to higher particle flux, recycling and radiation losses from this region and further reducing power conducted to the target.

In the experiment, in-out asymmetries show strong variance with the discharge/machine parameters, and in particular - with the direction of the toroidal magnetic field, B_T (or the ion ∇B drift). Analysing the pronounced effect of the B_T reversal can help in establishing the physical mechanisms responsible for in-out asymmetries, as well as for the SOL plasma transport as a whole.

A number of physical mechanisms discriminate in their effect on the asymmetries between ion and electron drift sides rather than between inner and outer sides. The ion drift side is located at the inner strike zone for the normal B_T, while the electron drift side - at the outer strike zone. The reversal of B_T exchanges the sides. The reversal of I_p does not exchange the sides, as it changes both the plasma current direction and the helicity of the field lines, and these two effects cancel each other. In the normal B_T direction, ion ∇B drift is directed towards the target, and in the reversed B_T - away from the target.

2. Basic trends in the in-out asymmetries caused by B_T reversal

So far, the most apparent evidence for the influence of the B_T reversal on the SOL was its effect on the in-out asymmetry in the power deposition to the target. The ratio P_{out} / P_{in} has on average dropped in NB heated discharges from 1.8 to 1.2 on JET (see fig.1 reproduced from [1]), from 3.0 to 1.3 on JT-60U [5], from 6.0 to 1.0 on DIII-D [6], from 1.4 to 1.15 on JFT-2M [7], and from 2.0 to 1.5 in Ohmic and ICR heated discharges on ASDEX-U [8], as the toroidal field was reversed.

Asymmetry in the electron density shows broad scattering. However, as a statistical average, the density was found to be higher at the inner side for moderate main plasma

densities in the case of normal B_T in ASDEX [9], JET and JT-60U, while T_e was higher at the outer side [1,2,10,11]. At very high densities the drop in T_e at the inner side is so significant, that plasma detaches at this side in JET [2], and the asymmetry in density reverses in favour of the outer side. In JT-60U, asymmetry in n_e seems to have been significantly suppressed when, following the rise in density, the MARFE condition has been reached [11]. In DIII-D, contrary to the observations in JET and JT-60U, it is the outer side which normally has both higher electron temperature and density in the discharges with additional heating [12]. Predominance of the power flux, n_e and T_e at the outer side in this machine compared to JET (both have the same aspect ratio, which is larger than on other machines), is believed to be due to an asymmetry in the gaps between the separatrix and the walls, and the slanted divertor tiles on the inboard side of DIII-D [13].

The B_T reversal, as it has been demonstrated on JET and JT-60U, as a general tendency, makes the density and temperature distributions near the target more symmetric [1,2,5,10,11]. On ASDEX n_e asymmetry even reversed [9], and on JT-60U [14] and JFT-2M [7] both n_e and T_e were reported to have reversed. For the analysis of the theoretical conceptions, carried out in the next section, it is important to note that the reversal of B_T causes n_e and T_e distributions to shift in the opposite directions: n_e - from the inner to the outer side, and T_e - from the outer to the inner side. Fig. 2, reproduced from [2], illustrates such trend in profile asymmetries observed in JET.

Changes in the plasma parameter asymmetries, caused by the B_T reversal, have been confirmed by measurements of the currents passing along the field lines between the two different strike zones. Systematic analysis of these currents, performed on JET [15] and JT-60U [14], revealed that in the case of normal B_T they flowed from the outer to the inner side due to mainly thermoelectric effect of T_e difference in favour of the outer strike zone [16]. In reversed B_T discharges, the direction of the SOL currents reversed. The T_e asymmetry reversed in JT-60U [14], while in JET it became more symmetric, with a slight shift on average towards the inner side. In both machines the electron pressure asymmetry between the strike zones has been found. In JET it was mainly in favour of the ion side, whereas in JT-60U the pressure was larger at the electron side. It has to be noted, that the pressure asymmetry can be strongly affected by the recycling and associated momentum loss of parallel plasma flow near the strike zones.

In the experiment, the most sustainable trend in the asymmetries' changes caused by the B_T reversal is the shift in the T_e distribution from the outer to the inner side, which in most cases leads to more equal T_e distribution in the reversed B_T (but T_e asymmetry even

reversed in JT-60U [14] and JFT-2M [7]). To illustrate this, we plotted in fig.3 maximum temperatures at the two strike zones for the JET discharges, which were earlier selected for the analysis in [15]. They included Ohmic and NBI heated discharges with the input power up to 14 MW. The magnetic configuration was varied from both B_T and I_p normal, to the reversed B_T, and then to the reversed I_p cases. Note that only the reversal of B_T has caused major changes in the T_e distribution, while the effect of the I_p reversal was less significant.

3. Main theoretical ideas

Changes in divertor asymmetries, caused by the B_T reversal, appear to be consistent with the hypothesis that the reversal of the toroidal field affects power sharing between the two divertor branches [2]. From the larger outer surface of the plasma and other mechanisms mentioned in Section 1, one would expect higher power flux to the outer divertor branch. This general tendency seems to be supplemented by the force which depends on the direction of the B_T , so that the toroidal field reversal shifts the fraction of the power from the outer to the inner side. However, at present, there is no theoretical justification to support this idea. Neither there is enough experimental evidence for it. Proper experimental measurements of the total power flux to each divertor branch should include radiation losses due to ionisation and charge exchange of the neutrals, as well as impurity radiation near the target. With the normal B_T all these processes seem to dominate at the inner side (higher recycling and radiation at the target and near the X-point on the inner side) [2]. Therefore, their inclusion may substantially equalise calculated total power flow to each divertor branch. Recent measurements on DIII-D with counting all existing power losses have revealed that power flow to the inner branch was $\sim 80\%$ of that to the outer branch, despite 4-6 times larger heating of the outer target surface [17].

Next we shall make a brief analysis of the main mechanisms which can affect the divertor asymmetries. One of the most frequently referenced mechanisms is the power and particle deposition to the target carried by fast ion losses. They potentially can deposit a substantial power to the target in additionally heated discharges [18]. Analysis of the loss ion orbits, however, shows, that, for two orbits with the same launching point inside the separatrix, the energy barrier for the ion to be lost to the target is substantially higher for the ion with the orbit terminating at the electron drift side than for the one - terminating at the ion drift side [19]. Therefore, fast ion losses can contribute more to the power flux at the ion drift side. Such power deposition could only aggravate our task of explaining the experiment. Monte-Carlo calculations of power deposition to the target [20] confirmed this expectation. Power deposition was found predominantly to the outer side for the reversed B_T. For the

normal B_T, ions at higher edge temperatures heated the inner side, and only for low ion temperatures, which were attributed to the Ohmic regime, power deposition was mainly at the outer side [20]. On the whole, however, we do not have sufficient experimental and theoretical information to judge which side receives the majority of the fast ion power.

Radial and poloidal electrical **E×B** drifts, which are illustrated in fig.4, replicated from [3] with some additions, for the normal B_T, are capable of changing the density redistribution between the strike zones. Radial flux, caused by poloidal electric field owing to the T_e drop towards the target and resulting thermoelectric force, has been suggested as a mechanism to increase the density at the ion side [3]. This means that the effect of such a drift agrees with basic experimental trends outlined in Section 2. In contrast, the poloidal flux, caused by radial electric field in the SOL, contributes to the density accumulation at the electron drift side. This classical drift has a clear nature and therefore can not be excluded from the SOL modelling. We can make a crude estimate of the particle flux to each divertor branch due to these drifts. Radial drift, suggested in [3], creates an additional source of plasma density at the ion drift side, whereas the poloidal drift - at the electron drift side. Plasma flow to the corresponding divertor branch is proportional to the poloidal potential drop from the midplane separatrix position to the divertor target for the radial flow, and to the potential drop from the same position across the SOL - for the poloidal flow. Therefore, the radial flow should be proportional to $\Gamma_\theta \sim T_e|_{sol} - T_e|_{div}$, whilst the poloidal flow - to $\Gamma_r \sim 3T_e|_{div}$, where the temperatures are taken at midplane separatrix and near the divertor target. The condition for the domination of the poloidal flow over the radial one is therefore: $T_e|_{sol} >> 4T_e|_{div}$. An opposite case of radial flow domination takes place when the electron temperature does not show significant poloidal variations and $T_e|_{div} >> (T_e|_{sol} - T_e|_{div})/3$.

There also exists in the plasma the diamagnetic, or $\mathbf{B} \times \nabla P$, mainly poloidal drift, the effect of which on the density asymmetry could be similar to the one of the poloidal electric drift, since its poloidal direction due to ion pressure gradient is parallel to the electric drift. However, as has recently been shown in [21], the diamagnetic drift, as well as similar temperature driven $\mathbf{B} \times \nabla T$ heat fluxes, do not deliver particles and energy to the target because of their nature of being predominantly divergence-free, as being caused mainly by the rotation of particles about their Larmor centres. However, while the diamagnetic drift fluxes can be ignored near the target, their non-divergence-free components are responsible for the up-down asymmetries in the main SOL [22], but they should not affect the in-out asymmetries discussed in the present paper. It has to be mentioned that the effect of the diamagnetic drifts in creating the source/sink of particles

and energy is equivalent to the effect of the corresponding $\mathbf{B} \times \nabla B$ toroidal drift terms in the Larmor guiding centre approximation.

Recently, another mechanism for the creation of the asymmetries at the target has been proposed, which, like the previously discussed electrical $\mathbf{E}\times\mathbf{B}$ drifts, is aimed at offering a force which redistributes the density between the strike zones. The origin of this force stems from experimentally observed (see e.g. [23] and refs. in [24]) and theoretically supported [24] toroidal rotation of the edge plasma. The rotation can be driven by ion orbit losses, which have anisotropic velocity distribution, so that mostly ions rotating opposite to the plasma current are lost to the target. As a result, plasma toroidal momentum just inside the separatrix in the direction parallel to I_p is formed. After this toroidal momentum is transferred to the SOL by the convection and/or perpendicular viscosity, it exerts a force on the SOL plasma. This force compresses the plasma at the ion strike zone, causing the density rise there. Such a mechanism for the density redistribution is effective only if the edge plasma is sufficiently hot and a large number of collisionless ion orbit losses occurs. There is an indication that such a toroidal rotation has been measured with reciprocating Langmuir probes at JET [16,25]. Experimental arrangement is presented in fig.5, replicated from [25] with small alterations. With the probe penetrating inside the separatrix, the reversal of plasma flow has been detected. The arrows around the probe in fig.5 indicate the projection of parallel plasma flow onto the poloidal cross-section. With the reversal of the flow inside the separatrix the plasma in this region flowed along the field lines parallel to the main plasma current. Although such distribution of plasma flows has been attributed in [25] to the effect of the ionisation source of neutrals from the target, there is also reason to believe that it reveals the effect of intrinsic plasma toroidal rotation inside the separatrix. This argument is strengthened by the fact that in the experiment flow reversal has been observed in low density L-mode and in H-modes (but not in higher density L-mode!), where we may expect large number of fast ion losses. The influence of the edge toroidal momentum on the SOL structure at present can not be assessed in a quantitative form. Its potential impact on the SOL can, however, be strong enough, since both experimental measurements and theoretical expectations point to the possibility that the toroidal velocity just inside the separatrix may approach the ion sound speed [24]. This may happen when the effective ion collisionality at the separatrix decreases to ≈ 1, i.e. ions approaching the banana regime. The compression of the SOL plasma towards the ion drift side, due to the presence of such a rotation, has a similar effect on the n_e asymmetry as the radial electric drift, i.e. consistent with experimental observations.

In addition to the fast ion related mechanism for the creation of the edge toroidal momentum, the effect of the unbalanced co-current NBI can not be excluded. The separation between these two mechanisms requires further investigation.

4. Discussion

Establishing the links between experimental data and theoretical conceptions, we should firstly note that in the experiment the effect of the B_T reversal seems to be weaker in low confinement, high recycling regimes. The connection between the recycling and power loading has been discussed in [1], where for both field directions unusually high P_{out} / P_{in} ratios were accompanied by high recycling rates. L-modes were found to have higher P_{out} / P_{in} ratios than the H-modes, as can be seen from fig.1. In [2] it was concluded that the pronounced effect of the B_T reversal seems to vanish at high densities. Concurrently with the last observation, recent radiative divertor experiment in DIII-D have produced only a modest effect of the B_T reversal on the power flux asymmetry [26]. An explanation for such a regime-dependent effect of the B_T reversal can be that in the regimes described above the edge temperature is expected to be low (compared to other regimes like hot ion mode or low density H-mode), reducing the strength of all the physical effects we considered. At the same time, anomalous perpendicular transport, in poor confinement, high density plasmas, is likely to have a strongly "ballooning" nature with poloidal variation of transport coefficients biased towards the outer side of the magnetic surface (see e.g. [3]).

In terms of the SOL and divertor parameters which may enable us to distinguish separate effects of the analysed physical mechanisms, we should discriminate between: a) high or medium density, high recycling plasmas with additional heating (probably $T_e|_{sol} >> 4T_e|_{div}$ case), and b) low density regimes with additional heating and small fraction of charge exchange and radiation power $(T_e|_{div} >> (T_e|_{sol} - T_e|_{div})/3$ case with high T_i, T_e and collisionless edge plasma). The majority of regimes of practical interest, which have created a database for the main experimental trends outlined in Section 2, seem to have fallen into the category a). Both the radial **E×B** drift and the effect of the toroidal momentum could have contributed to the increase of n_e at the ion drift side, and consequently to the increase of recycling and radiation there. This must have eventually lead to the decrease of T_e at the ion side (with further increase of radiation) and explain why T_e asymmetry has been reduced when the toroidal field was reversed.

In the b) case the effect of the poloidal **E×B** drift is to increase both density and power flux at the electron drift side. A number of experimental observations from JET indicate,

however, that in low density H-modes with normal B_T the inner side receives higher power flux (in the quiescent phase of the H-mode) [2]. An example of the power flux distribution to the target in JET is presented in fig.6 (reproduced from [27]). After an L-H transition, the asymmetry in power deposition in favour of the inner strike zone has developed. This discharge was not dominated by the radiation, and good power accountability was achieaved. A remarkable effect of the main plasma density influence on power asymmetries was demonstrated in NB (20.5 MW) plus LHRF (2 MW) heated discharge on JT-60 [28] with normal B_T. As the density was raised from $2.7 \times 10^{19} m^{-3}$ to $3.6 \times 10^{19} m^{-3}$ due to the NBI, the ratio P_{out} / P_{in} increased from 0.8 to 1.6, while the same ratio for the maxima of power density showed even greater increase: from 0.56 to 1.65. Another evidence for the existance of some mechanism that can increase the density at the ion drift side when the edge plasma becomes collisionless, is presented in table 1 (reproduced from [29]). Comparison between high and low density Ohmic discharges, and high and low power H-modes shows that, as the SOL T_e was increased, the plasma became more collisionless and the temperature difference between strike zones was eliminated. More power, electron pressure, density and particle flux were measured at the inner side with the Langmuir probes. While the data from the IR camera on JET could be partly attributed to the fast ion power deposition at the inner side, the data from the Langmuir probes provide a strong support for the idea that there should be some external force which compresses the SOL plasma at the ion drift side. A candidate for this force can be the effect of the edge toroidal momentum.

Concerning relative role of various physical mechanisms in creating the divertor asymmetries, we may also consider the case $T_e|_{div} >> (T_e|_{sol} - T_e|_{div})/3$ in low density Ohmic plasmas in open divertor configurations, with a weak interaction between the plasma and neutrals and low radiation. In this case all the mechanisms listed above are void except for the poloidal **E**×**B** drift, which should compress the plasma at the electron drift side. It is arguable whether such situation may occur in practice in divertor discharges. However, it could have been more easily realised in Ohmic limiter discharges on TEXTOR [30]. The toroidal limiter, located on the low field side 45° below the midplane was used in the series of discharges with medium density and large limiter radius (implying low current density and low heating power per unit volume). The B_T reversal has lead to an increase in plasma density at the electron drift side of the limiter, which (as is has been noted in [30]) could be explained by the poloidal **E**×**B** drift.

5. Conclusions

Apart from the heuristic hypothesis of the changes in power sharing between the two divertor branches caused by the B_T reversal, there exist a number of physical mechanisms which redistribute density between the two divertor branches. Qualitative analysis of these mechanisms shows that two of them - the radial **E×B** drift and the momentum transfer into the SOL due to the edge toroidal momentum parallel to the main plasma current - increase the density at the ion drift side. Such a density redistribution between the sides should make plasma parameters and power flux to the target more symmetric in the case of the reversed B_T, in accordance with the general trend seen in the experiment. The effect of the radial **E×B** drift must be stronger than the opposite effect of the poloidal **E×B** drift (which compresses the plasma at the electron drift side) in high power high recycling regimes. In the extreme case of very high densities the drop in T_e at the inner side in normal B_T can lead to detachment of the plasma at this side, making both temperature and density higher at the outer side.

In another extreme case of low density and high power discharges where edge T_e and T_i are high and the SOL plasma becomes collisionless, the poloidal **E×B** drift must dominate over the radial one. In this situation the effect of the edge toroidal momentum seems to be the only mechanism which can overweigh the influence of the poloidal **E×B** drift and explain why the plasma in these discharges appears to be denser at the inner side (in the normal B_T), with higher pressure and power deposition there.

References

[1] R.Reichle et al., Proc.18th Eur.Conf., Berlin,1991,V.15C, part 3, 105.

[2] G.Janeschitz et al., Proc.20th Eur.Conf., Lisboa,1993,V.17C, part 2, 559.

[3] F.L.Hinton, G.M.Staebler, Nucl.Fus.29(1989)405.

[4] U.Daybelge, Nucl.Fus. 21(1981)1589.

[5] K.Itami, M.Shimada, N.Hosogane, J.Nucl.Mater.196-198(1992)755.

[6] D.N.Hill et al., J.Nucl.Mater. 176&177(1990)158.

[7] I.Nakazawa et al., Proc. 16th Eur. Conf., Venice,1989,Vol.13B, part 3, 887.

[8] A.Herrmann et al., Proc. 20th Eur.Conf., Lisboa,1993,Vol.17C, part 2, 567.

[9] F.Wagner et al., J.Nucl.Mater.121(1984)103.

[10] N.Asakura et al., J.Nucl.Mater.196-198 (1992)1069.

[11] N.Asakura et al., Recycling enhancement with $\bar{n}_e$ and q_{eff} in high density discharges on JT-60U,(1993), submitted to Nucl.Fus.

[12] D.Buchenauer et al., J.Nucl.Mater.196-198(1992)133.

[13] G.M.Staebler, private communication.

[14] K.Itami et al., Proc.14th Int.Conf. on Plasma Phys. and Controlled Nucl. Fus. Res. (Wurzburg, 1992) IAEA, V.1, p.391.

[15] A.V.Chankin et al., J.Nucl.Mater.196-198 (1992) 739.

[16] P.J.Harbour et al., J.Nucl.Mater.162-164 (1988) 236.

[17] A.W.Leonard et al., Power Flow in the SOL and Divertor Plasmas of DIII-D, APS Conference, V.38, No.10(1993)2059.

[18] H.Weisen et al., Nucl.Fus.31(1991)2247.

[19] A.V.Chankin, G.M.McCracken, Nucl.Fus.33(1993)1459.

[20] M.A.Kovanen et al., Nucl.Fus.32(1992)863

[21] A.V.Chankin, P.C.Stangeby, The Effect of the Diamagnetic Drift on the Boundary Conditions in Tokamak Scrape-Off Layers and the Distribution of Plasma Fluxes Near the Target, JET-P(94)18, submitted to Plasma Phys. and Contr. Fus.

[22] J.Hugill, J.Nucl.Mater.196-198(1992)918.

[23] V.A.Vershkov and the T-10 Group, J.Nucl.Mater.162-164(1989)195.

[24] A.V.Chankin, W.Kerner, O.P.Pogutse, The Generation of Edge Toroidal Momentum due to Ion Orbit Losses and its Effect on the Scrape-Off Layer, JET-P(94)03, submitted to Nucl.Fus.

[25] A.Loarte et al., Proc. 20th Eur.Conf., Lisboa, 1993,V.17C, part 2,555.

[26] D.Hill, private communication.

[27] A.V.Chankin et al., Plasma Phys. and Contr. Fus.36(1994)403.

[28] K.Itami et al., J.Nucl.Mater.176&177(1990)504.

[29] A.Loarte, PhD Thesis, Universidad Complutense de Madrid (1992).

[30] U.Samm et al., Nucl.Fus.31(1991)1386.

	High density Ohmic		Low density Ohmic	
Parameter	Inner side	Outer side	Inner side	Outer side
I_{sat}(A/cm^2) at sep. position	16.2± 0.4	15.9± 0.5	6.3± 0.1	6.6± 0.1
T_e (ev) at sep. position	13.3± 1.1	30.9± 3.1	33.8± 10.8	43.9± 2.9
n_e (10^{18} m^{-3}) at sep. position	19.9± 1.2	12.6± 1.3	9.9± 0.9	4.5± 0.2
Pressure (10^{20} ev/m^3) at sep. pos.	2.7± 0.1	3.9± 0.3	1.6± 0.3	2.0± 0.1
Pow. Flux dens.(MW/m^2) at sep.	15.8± 1.3	37.8± 3.8	16.5± 5.4	23.6± 1.4
Total Part.Flux (10^{22} s^{-1})	2.2± 0.1	2.8± 0.2	2.4± 0.2	1.2± 0.1
Total Power Flux (MW)	0.24± 0.03	0.78± 0.1	0.29± 0.14	0.43± 0.05
	Low power H-mode		High power H-mode	
Parameter	Inner side	Outer side	Inner side	Outer side
I_{sat}(A/cm^2) at sep. position	9.4± 1.1	6.0± 0.9	7.3± 0.7	5.1± 0.7
T_e (ev) at sep. position	24.6± 9.1	39.7± 9.9	59.3± 18.7	50.4± 10.1
n_e (10^{18} m^{-3}) at sep. position	8.2± 2.4	4.2± 1.1	4.2± 1.1	3.1± 0.5
Pressure (10^{20} ev/m^3) at sep. pos.	2.1± 0.5	1.8± 0.4	2.6± 0.6	1.7± 0.3
Pow. Flux dens. (MW/m^2) at sep.	18.7± 7.1	20.1± 5.3	37.4± 12.4	21.9± 5.6
Total Part.Flux (10^{22} s^{-1})	1.5± 0.3	0.9± 0.3	1.2± 0.2	0.7± 0.2
Total Power Flux (MW)	0.37± 0.17	0.32± 0.15	0.50± 0.20	0.30± 0.10

1. Ion saturation current, electron temperature, density, electron pressure and power flux density at the target near the separatrix position, and total particle and power fluxes at each strike zone, calculated from Langmuir probe data assuming $T_e = T_i$.

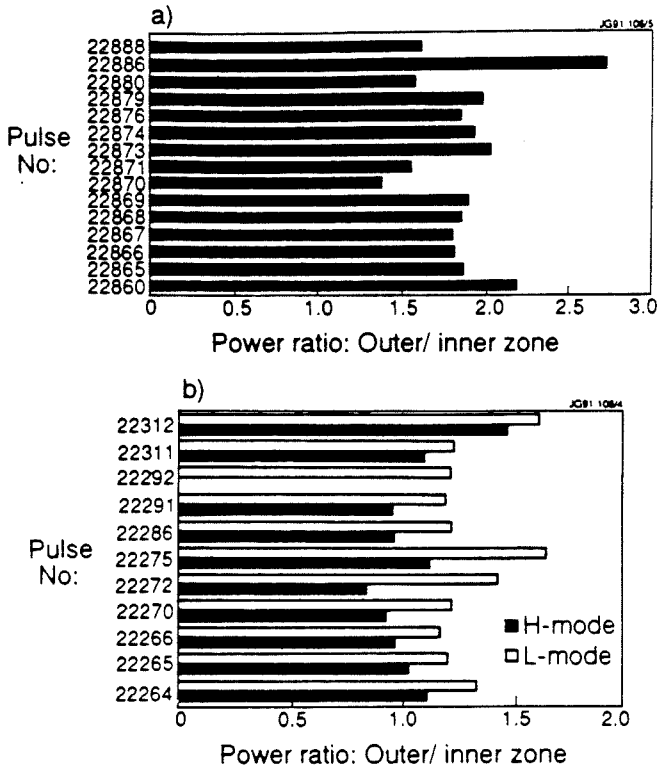

1. P_{out} / P_{in} ratios for normal (a) and reversed (b) field in JET.

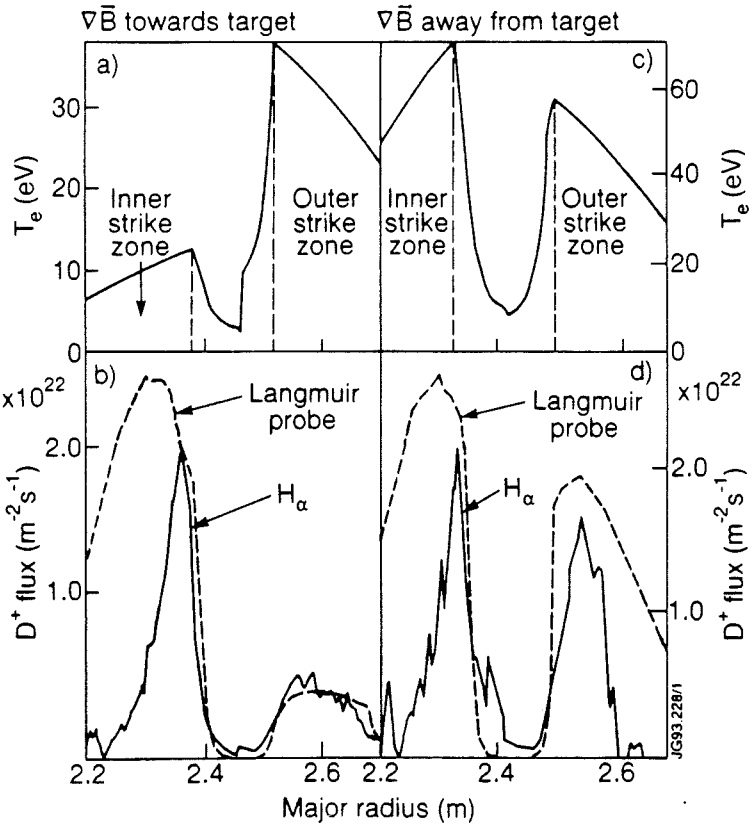

2. T_e and D^+-flux profiles for a 12 MW heated ELM free H-mode discharge with normal B_T direction (a,b) and a 15 MW NBI heated hot ion H-mode discharge with reversed B_T (c,d) in JET. The pronounced asymmetry between the strike zones in case of normal B_T in contrast to reversed B_T can be seen.

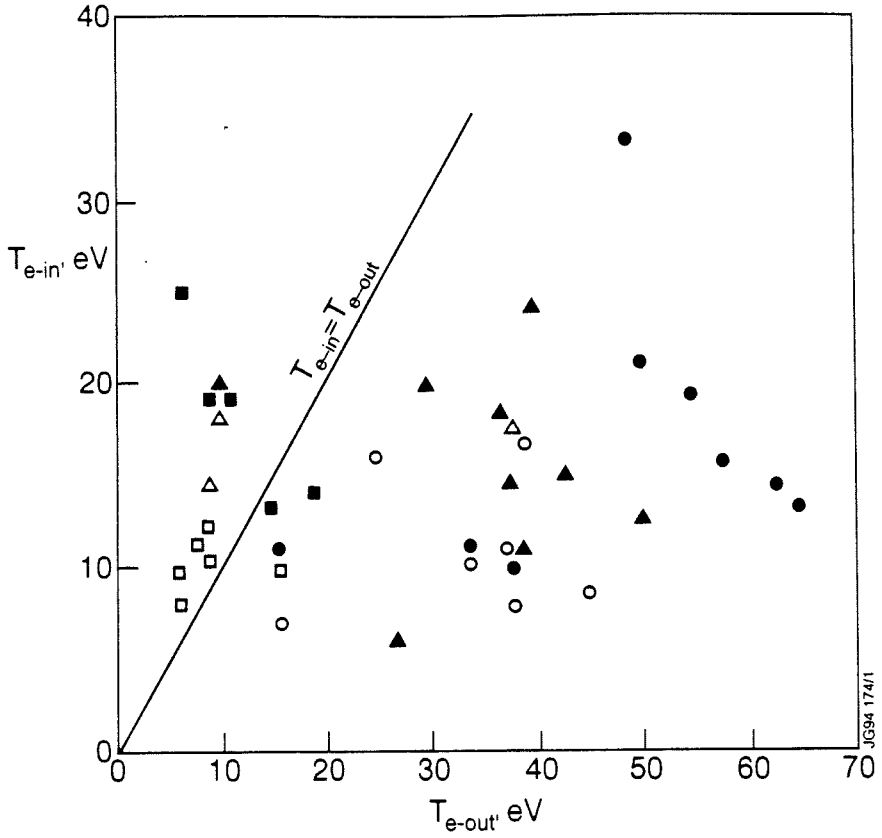

3. Maximum temperatures at the two strike zones observed in JET discharges. Circles - normal B_T and I_p, squares - reversed B_T, triangles - reversed I_p plasmas. Open symbols correspond to Ohmic discharges, dark symbols - no NBI heated discharges.

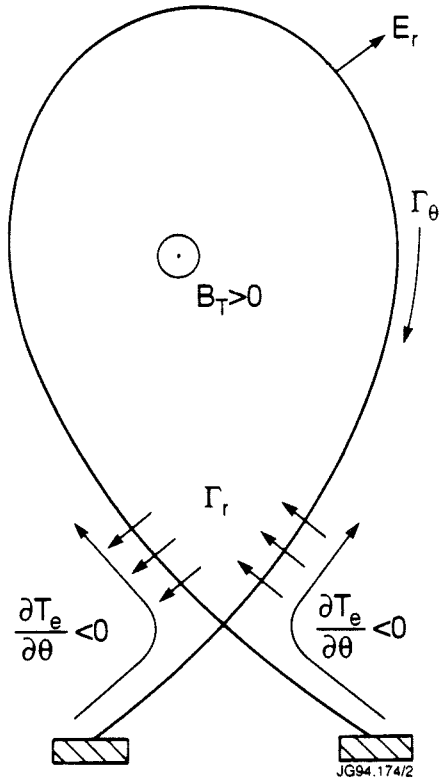

4. The direction of radial and poloidal **E**×**B** drifts for the case of normal B_T.

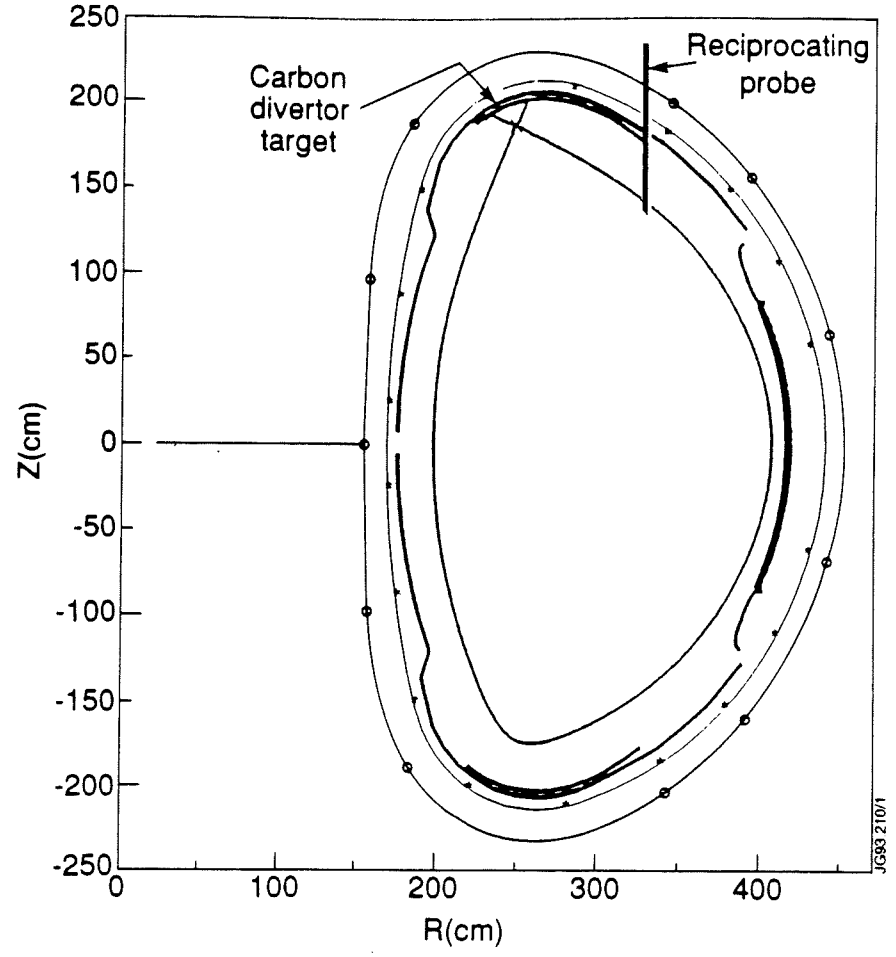

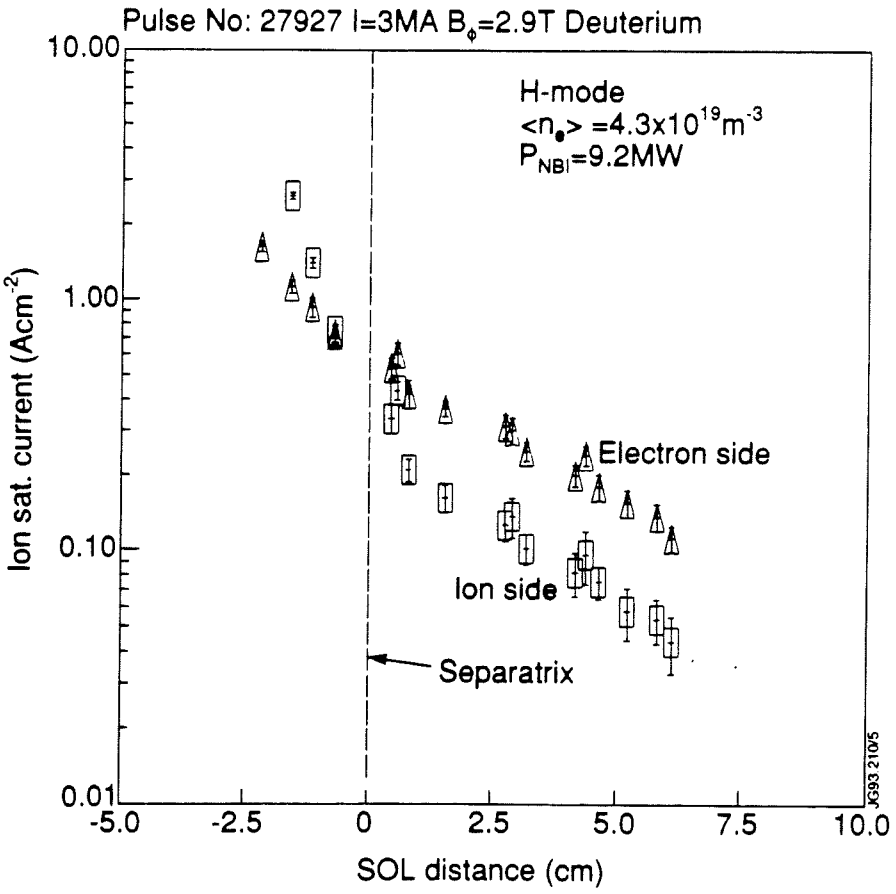

5. Position of the reciprocating probe and the projection of parallel flows onto the poloidal cross-section (top), and measured ion saturation currents versus distance normal to the flux surfaces at the probe position (bottom) in JET.

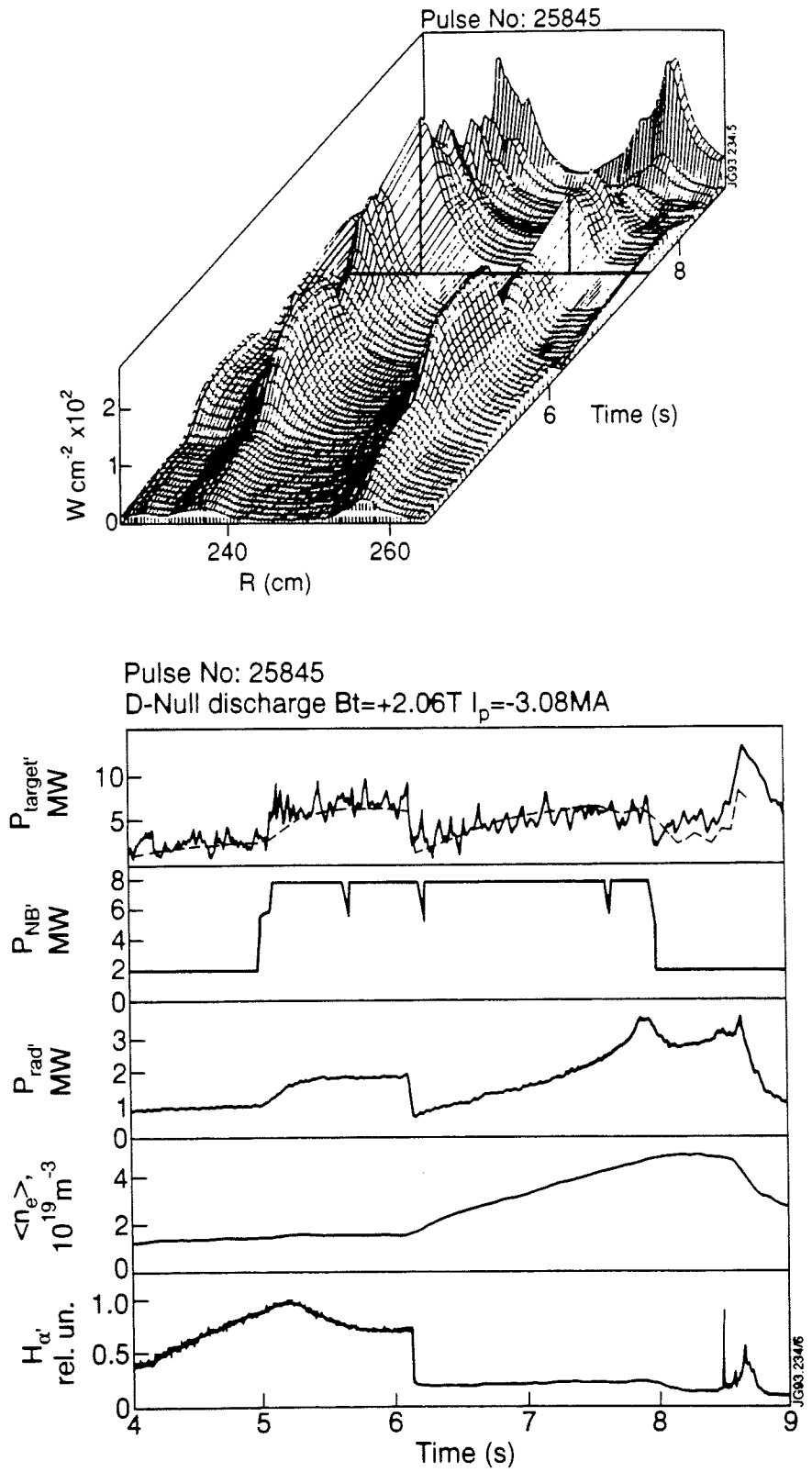

6. Time evolution of the poloidal profiles of deposited power (top), power conducted to the target (calculated from both IR data and global power balance), NBI heating power, radiated power, volume average density and H_α emission at the target (bottom) for a low density H-mode discharge in JET.

Comparison between Measured Scrape-off Layer Plasma Parameters and 2-D Model Calculations for JET X-point Discharges

A Loarte, A Chankin, S Clement, G Corrigan, P Harbour, L Horton, G Janeschitz[1], J Lingertat, G Matthews, R Simonini, J A Tagle[2], A Taroni, G Vlases.

JET Joint Undertaking, Abingdon, Oxon, OX14 3EA.
[1] ITER–EDA, Garching, Germany.
[2] IBERDROLA, Madrid, Spain.

1. INTRODUCTION.

Two dimensional fluid codes for the plasma linked with a Monte-Carlo (or diffusive) code for the neutrals [1, 2, 3] are routinely used to predict the performance of divertor tokamak experiments and reactors. Hence, it is necessary to compare the predictions of these codes with experimental measurements in order to assess the reliability of the models and assumptions contained in them. Such a study is presented in this paper for the JET 2-D fluid code EDGE2D/U [1] using experimental measurements from JET diverted discharges.

2. EXPERIMENTAL MEASUREMENTS.

The basic measurements used in this assessment are from Langmuir probes embedded in the divertor target plate and from a reciprocating Langmuir probe which enters the scrape-off layer plasma away from the divertor region. Bolometric measurements for the main plasma and divertor region are also used to determine (together with the input power and diamagnetic energy) the energy flow out of the main plasma to the SOL. Generally, the main uncertainties involved in the Langmuir probe measurements are those associated with their effective area, which determines the value of the electron density measured, and with the position of the probe with respect to the magnetic separatrix. The location of the target probes with respect to the magnetic separatrix is determined very accurately [4]. However, the effective area of these probes may be affected by shadowing from parts of the divertor plate and may change due to erosion during the course of the experiments. On the other hand, the reciprocating effective area is well defined, whereas its position with respect to the magnetic separatrix is determined with a typical accuracy of 1 cm at the outer midplane [5]. Since the

typical fall off length of plasma parameters in the SOL is of the order of 1 cm or less, it is clear that the relative position of the probe to the separatrix must be known with a much higher accuracy in order to assess quantitatively the gradients of the SOL plasma parameters along the field lines. For this reason, in our study we use the conservation of electron pressure along the field lines (no large momentum losses), which connect the reciprocating probe and the target probes, to determine the distance between the reciprocating probe and the separatrix [6]. In this paper we consider discharges in all confinement regimes (Ohmic, L-mode, H-mode) and in deuterium and hydrogen.

3. MODELLING ASSUMPTIONS AND INPUTS.

3.1. MODELLING ASSUMPTIONS.

The code EDGE2D/U contains physical models with various degrees of sophistication; in this study we have used the code in the simplest way to model basic features of the discharges and leave the investigation of more complicated experimental features with more advanced models to the future. Hence, only modelling of pure plasmas has been carried out and no drift terms have been included nor has the influence of currents in the SOL on the sheath boundary conditions been considered. The only asymmetries between the divertor strike zones contained in the model are those associated with the toroidal geometry of the SOL and no other intrinsic term that may lead to such asymmetries, such as momentum transfer from the main plasma to the SOL [7], has been included. Correspondingly, only measurements at the outer divertor target are presented in this study.

The real non orthogonal geometry of the divertor target has been used in the modelling and perfect recycling (recycling coefficient R = 1) assumed (a sensitivity study performed is discussed in section 4.3).

Transport is assumed to be classical along the field line and anomalous across the field. Only a flux limit for the momentum flux along the field is used [8], which is important to avoid unphysically large viscous effects at high SOL temperatures. Two basic assumptions can be used in the code to characterize the radial anomalous transport which determine the value of the radial diffusion coefficients

deduced from modelling the experiment : either the radial fluxes are driven by gradients of temperature and density in the radial coordinate or they are driven by gradients in magnetic flux coordinate. In the first case the diffusion coefficients are poloidally constant (in our notation $D_\perp$, $\chi_\perp$), in the second case they increase with poloidal flux expansion ($\hat{D}_\perp$, $\hat{\chi}_\perp$ will represent their value at the outer midplane).

One of the problems found in modelling most of the discharges in JET is that the region over which the field lines connect both divertor strike zones without intersecting any other material surface (i.e. ''pure single-null'' configuration) is relatively narrow, typically $\lesssim 2$ cm at the outer midplane, which is comparible to the typical SOL thickness. Hence the radial boundary conditions at the outer edge of the SOL must be defined consistently with the diffusion coefficients used in the modelling. This is done by imposing a decay length in the outer edge of the SOL, deduced from the calculated profiles with the assumption that the density profiles decay exponentially from the separatrix and the temperature profiles follow approximately the dependence obtained if conduction along the field dominates i.e. $T \propto (Const. + \Delta R)^{-4/5}$ [9]. Other typical assumptions, valid when the ''magnetic SOL'' is very broad, such as assuming given small values of plasma parameters in the outer part of the computational domain or zero gradients there, are obviously not applicable in our case.

3.2. MODEL INPUTS VARIED TO FIT EXPERIMENTAL DIVERTOR PARAMETERS.

The basic inputs which determine the SOL plasma parameters in EDGE2D/U are the total hydrogenic ion content in the computational domain and the power flow out of the main plasma carried by the electrons and the ions into this domain. These two inputs together with the effective transport coefficients for anomalous transport determine the main SOL plasma density and temperature profiles. In JET, measurements of the ion temperature at the plasma edge are very sparse, hence we usually assume that the same power flows out of the main plasma the SOL via the electrons and the ions.

The experimental situation with respect to the power balance is unclear in JET discharges. From Langmuir probe measurements, the power balance is

satisfactory for Ohmic and low power L-mode discharges. For high power L-modes and H-modes the situation is unsatisfactory because although the probes clearly show a worsening of the power balance [10], there are indications from infrared measurements which point towards a similar power balance in L-mode and H-mode [11]. This was attributed in [11] to the proximity between the X-point and the divertor plate for those discharges, which favours a better estimate (with infrared measurements) of the recycling losses deposited onto the target. Another possible explanation for this disagreement is based on the large electron currents observed in JET close to the separatrix strike point [12] and which have not been considered to calculate the power measured with the Langmuir probes. In principle, the power flow associated with these currents could be of the same order of magnitude of the missing power, but its estimate depends critically on the influence of secondary electron emission on the sheath transmission coefficient, which is poorly known. Hence, these measurements close to the separatrix strike point are not considered in the study performed in this paper, where we assume that their influence in the plasma parameters away from the strike point is negligible.

Despite the experimental uncertainties, the power which enters the SOL to be used in the code cannot be much larger than that determined experimentally from bulk plasma measurements (because of different asymmetries in code and experiment, and modelling only performed for the outer divertor). Hence, in the modelling, the power which enters the SOL via the electrons and ions channels $P_{e,i}$ must satisfy

$$P_e + P_i \lesssim P_{SOL} = P_{INP} - P_{RAD}^{BULK} - \dot{W} \qquad (1) \quad ,$$

where P_{INP} is the input power, P_{RAD}^{BULK} is the power radiated in the bulk plasma and $\dot{W}$ is the time derivative of the plasma diamagnetic energy. However, due to the different asymmetries in the code and the experiment only trends in the power balance for various regimes can be assessed from the comparison of modelling and experiment. The values of $D_\perp$, $\chi_\perp$ used in modelling are determined from the measured plasma parameter profiles in the main SOL and at the divertor target.

4. DISCHARGES MODELLED AND MODELLING RESULTS.

4.1. DISCHARGES WITH ONLY DIVERTOR TARGET MEASUREMENTS.

The parameters for a series of hydrogen discharges using the upper JET divertor target (Carbon target) in various confinement regimes which has been modelled are given in Table 1 (Δ_X is the distance between X-point and divertor target).

Pulse	Conf.	I (MA)	B_ϕ (T)	Δ_X (cm)	$< n_e >$ (10^{19} m^{-3})	P_{INP} (MW)	P_{SOL} (MW)	P_{RAD}^{DIV} (MW)
24165	Ω	3	3.2	9.6	1.2	1.6	1.2	0.2
24175	L	3	2.1	8.9	1.1	5.5	4.9	0.4
24171	H	3	2.1	7.9	2.3	8.0	4.2	0.3

Table 1. Plasma parameters for the hydrogen discharges modelled.

The summary of the modelling results for these discharges is given in table 2.

Pulse	n_{sep} (10^{18} m^{-3})	$\frac{n_{sep}}{< n_e >}$ (%)	$P_e = P_i$ (MW)	$\frac{(P_e + P_i)}{P_{SOL}}$ (%)	$\hat{D}_\perp$ (m^2/s)	$\hat{\chi}_{\perp e,i}$ (m^2/s)
24165	5.3	44	0.7	87	0.1	0.5
24175	5.2	46	1.6	65	0.2	0.5
24171	6.5	28	0.8	38	0.05	0.25

Table 2. Modelling results for discharges in Table 1.

An example of the temperature profiles obtained with EDGE2D/U and from probe measurements at the divertor target for the ohmic discharge is shown in Fig. 1. By mapping these profiles along the field lines it is possible to represent midplane SOL profiles and target profiles versus flux surface spacing at a given spatial position. In the following figures this has been done taking as reference spatial point the outer midplane of JET. In Fig.2 the mapped profiles for the ohmic discharge are shown.

The effective values of the diffusion coefficients to be used in order to model the measurements are very small (particularly $\hat{D}_\perp$) as reported in [13], which is in agreement with similar results for DIII-D [14] and ASDEX-Upgrade [15]. They

are much smaller than the Bohm value which, for instance, for the discharge 24165 would be $D_{\perp}^{Bohm} \simeq 1\ m^2/s$). The values of the deduced transport coefficients follow the trend expected from the changes in main plasma confinement, being larger for L-mode than for H-mode.

The trends in the power balance with Langmuir probes for various confinement regimes are also reflected in the modelling of these discharges. However the percentage of power into the SOL (compared to P_{SOL}) used in the simulations is higher than that deduced from the experimental interpretation of the Langmuir probe measurements, where electron and ion temperatures are assumed to be equal. This is due mainly to the behaviour of the calculated ion temperature which tends to be higher than the electron temperature and has a much flatter profile (both factors increase the amount of power that arrives at the divertor target for the same electron parameters). Although for these discharges no measurements were available for the main SOL plasma parameters, the values of separatrix density used in the model are consistent with those from similar discharges from the JET/DIII-D database [16], in particular the drop in the ratio of separatrix to main plasma densities when the discharges are in the H-mode.

As these pulses do not show very high recycling at the divertor (low n_{sep}), the energy coupling between electrons and ions in the SOL is very weak and hence it is possible to obtain similar results for the electron parameters (n_e , T_e) with much higher ion temperatures (taking $P_i >> P_e$) and much better power balance correspondingly. This study has been done for the pulse 24171 whose electron SOL and divertor parameters can be obtained with the same transport coefficients and taking $P_e = 0.7MW$ and $P_i = 3.0MW$.

4.2. DISCHARGES WITH MEASUREMENTS AT DIVERTOR TARGET AND MAIN SOL.

The parameters for two deuterium discharges using the lower JET divertor target (Beryllium target) in L-mode which have been modelled are given in table 3. For these discharges measurements are available both in the main SOL and the divertor target.

Pulse	Conf.	I (MA)	B_ϕ (T)	Δ_X (cm)	$< n_e >$ (10^{19} m^{-3})	P_{INP} (MW)	P_{SOL} (MW)	P_{RAD}^{DIV} (MW)
25720	L	3	2.9	8.0	1.6	3.2	2.4 (*)	0.7 (*)
25710	L	3	2.9	8.0	2.6	3.4	2.7 (*)	1.9 (*)

(*) The divertor radiation is somewhat uncertain for JET Beryllium target X-point discharges because of restrictions in the field of view of the bolometer cameras.

Table 3. Plasma parameters for the deuterium discharges modelled.

The summary of the modelling results for these discharges is given in table 4.

Pulse	n_{sep} (10^{18} m^{-3})	$\frac{n_{sep}}{< n_e >}$ (%)	$P_e = P_i$ (MW)	$\frac{(P_e + P_i)}{P_{SOL}}$ (%)	$\hat{D}_\perp$ (m^2/s)	$\hat{\chi}_{\perp e,i}$ (m^2/s)
25720	5.5	34	0.7	58	0.05	0.7
25710	9.2	35	1.1	81	0.05	0.5

Table 4. Modelling results for discharges in Table 3.

The comparison between the results of these calculations and the measurements is shown in Fig.3 for discharge 25720 and Fig. 4 for discharge 25710. Due to the uncertainty in the distance between the reciprocating probe and the separatrix, the profiles measured with this probe have been shifted so as to obtain experimental electron pressure balance. The agreement between experiment and model is good for the low density pulse (25720) and slightly worse for the high density one (25710). This trend holds at higher densities and it is due to the absence of impurity radiation in our model which becomes dominant at higher densities for these levels of input power. Another trend which is observed when comparing hydrogen and deuterium discharges is that the particle diffusion coefficients tend to be smaller for deuterium as seen in the ratio of separatrix density to line average density used in the modelling. This is associated with a higher ionization in the divertor for the case of deuterium.

4.3. SENSITIVITY STUDIES.

Some sensitivity studies have been performed in order to assess the dependence of the results on the assumptions made in modelling :

• Radial Transport : Similar results in the main SOL and the divertor target can be obtained for either assumption (radial fluxes proportional to spatial gradients or gradients in magnetic flux) provided that the values of the transport coefficients are taken as

$$D_{\perp} \text{ (Radial spacing)} \simeq 2 \times \hat{D}_{\perp} \text{ (Magnetic Flux spacing).} \qquad (2)$$

The same relation holds for $\chi_{\perp}$. Very different plasma parameters and decay lengths in the private flux region are found for either case (steeper for radial spacing). The existing measurements in the private flux region of the JET divertor fall in between the two assumptions being more consistent with magnetic flux spacing driven fluxes, but the spatial resolution of the measurements is too coarse to draw definite conclusions. The asymmetry for the power arriving at the divertor strike zones calculated with the code is associated with the toroidal geometry of the SOL and the Shafranov shift which compresses the flux surfaces in the outer side of the torus. This asymmetry depends on the transport model and increases with plasma collisionality, being larger (5 - 15 %, for the discharges modelled) for radial spacing driven fluxes. However, the typical power asymmetry value calculated (30% more power to the outer side) may be very different from that found in experiment which depends on discharge conditions [17].

• Recycling coefficient : At low divertor densities the relation between the midplane and divertor scrape-off layer densities depends weakly on the value of the recycling coefficient used (provided $R \simeq 1$). However, at higher densities the value of the calculated divertor density (for the same midplane density) is more sensitive to the value of R assumed. For instance, in modelling the discharge 25710, it was found that reducing the recycling coefficient to 0.95 decreased the divertor density by approximately 40% for the same midplane density. Hence, an experimental assessment of the value of the recycling coefficient is needed in order to model accurately high density discharges.

5. CONCLUSIONS AND FURTHER WORK.

Measured plasma parameters at the divertor target of JET can be modelled for all regimes with reasonable or "measured" (once corrected for electron pressure balance) main SOL plasma parameters. While the modelled power balance is

satisfactory in ohmic and L-mode discharges a sizeable amount of power cannot be accounted for (assuming $P_e \simeq P_i$) in H-mode discharges. Very small values of the effective diffusion coefficients (one to two orders of of magnitude smaller than Bohm, for particle diffusion) must be used to match the measured steep radial profiles of electron density and temperature. The modelled and measured main SOL plasma density profiles decay exponentially from separatrix while temperature profiles do not decay exponentially because of the contribution of conduction to the energy transport along the field. Modelling of the discharges with full impurity treatment has been performed and the preliminary results are encouraging but further work in this line is needed to assess the transport of impurities in divertor discharges.

Acknowledgments : J. Spence is acknowledged for his technical assistance in the use of EDGE2D/U.

6. REFERENCES.

[1] Simonini, R., Corrigan, G., Radford, G., et al., Contrib. Plasma Phys. **34** (1994) 368.

[2] Schneider, R., Reiter, D., Zehrfeld, H.P., et al., J. Nucl. Mater. **196 - 198** (1992) 810.

[3] Rognlien, T.D., Milovich, J.L., Rensink, M.E., et al., J. Nucl. Mater. **196 - 198** (1992) 347.

[4] O'Brien, D.P.J., Ellis, J.J., Lingertat, J., Nucl. Fusion **33** (1993) 467.

[5] Zwingmann, W., Ellis, J.J., Lingertat,J., et al., Proc. 20th EPS Conf. Contr. Fus. & Plasma Phys., Vol. 17C Part I (1993) 195.

[6] Vlases, A., JET Team, Proc. 14th IAEA Conf. Plasma Phys. & Contr. Nucl. Fusion Res., Vol. 1 (1992) 287.

[7] Chankin, A., et al., 11th PSI Conference, Mito, Japan (1994).

[8] Radford, G., Contrib. Plasma Phys. **32**(1992) 297.

[9] Keilhacker, M., Lackner, K., Behringer, K., et al., Physica Scripta. **T2/2** (1982) 443.

[10] Loarte, A., PhD Thesis, Universidad Complutense de Madrid (1992).

[11] Chankin, A., Summers, D.D.R., Jaeckel, H.J., et al., Plasma Phys. and Contr. Fusion **36** (1994) 403.

[12] Lingertat, J., et al., 11th PSI Conference, Mito, Japan (1994).

[13] Simonini, R., Taroni, A., Keilhacker, M., et al., J. Nucl. Mater. **196 - 198** (1992) 369.

[14] Porter, G.D, ITER Tech. Meet. & Workshop on Divertor Physics Garching (FRG) 1994.

[15] Bosch, H.S., Schneider, R., Pitcher, C.S.,et al., Proc. 20th EPS Conf. Contr. Fus. & Plasma Phys. Vol. 17C Part II (1993) 795.

[16] Matthews, G.F., Jong, R.A., Porter, G.D., et al., 35th APS Div. Plasma Phys. Meet., St Louis (USA) 1993.

[17] Reichle, R., Clement, S., Gottardi, N., et al., Proc. 18th EPS Conf. Contr. & Plasma Phys., Vol. 15C Part III (1991) 105.

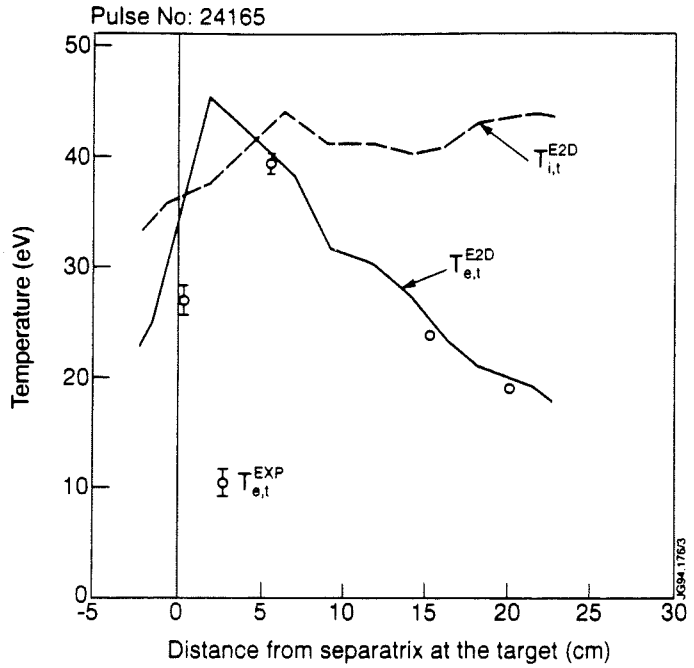

Fig.1. Measured Electron Temperature at the divertor target (EXP) and modelled (E2D) Electron and Ion Temperatures.

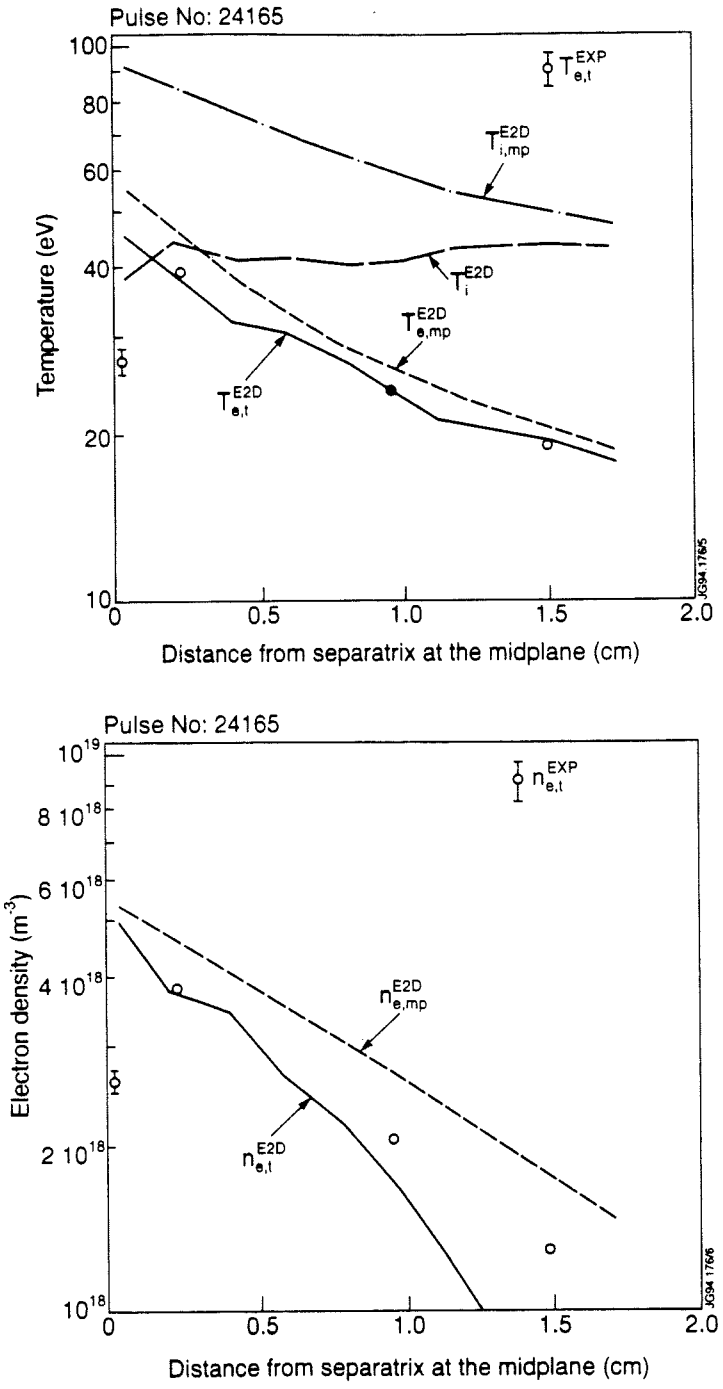

Fig.2. (a) Measured Electron Temperature at the divertor target (EXP) and modelled (E2D) Electron and Ion Temperatures at the midplane (mp) and divertor target (t). (b) Measured Electron Density ($T_i \simeq T_e$ assumed) at the divertor target (EXP) and modelled (E2D) Electron Density at the midplane (mp) and divertor target (t). The divertor target profiles are mapped to the outer midplane along the flux surfaces.

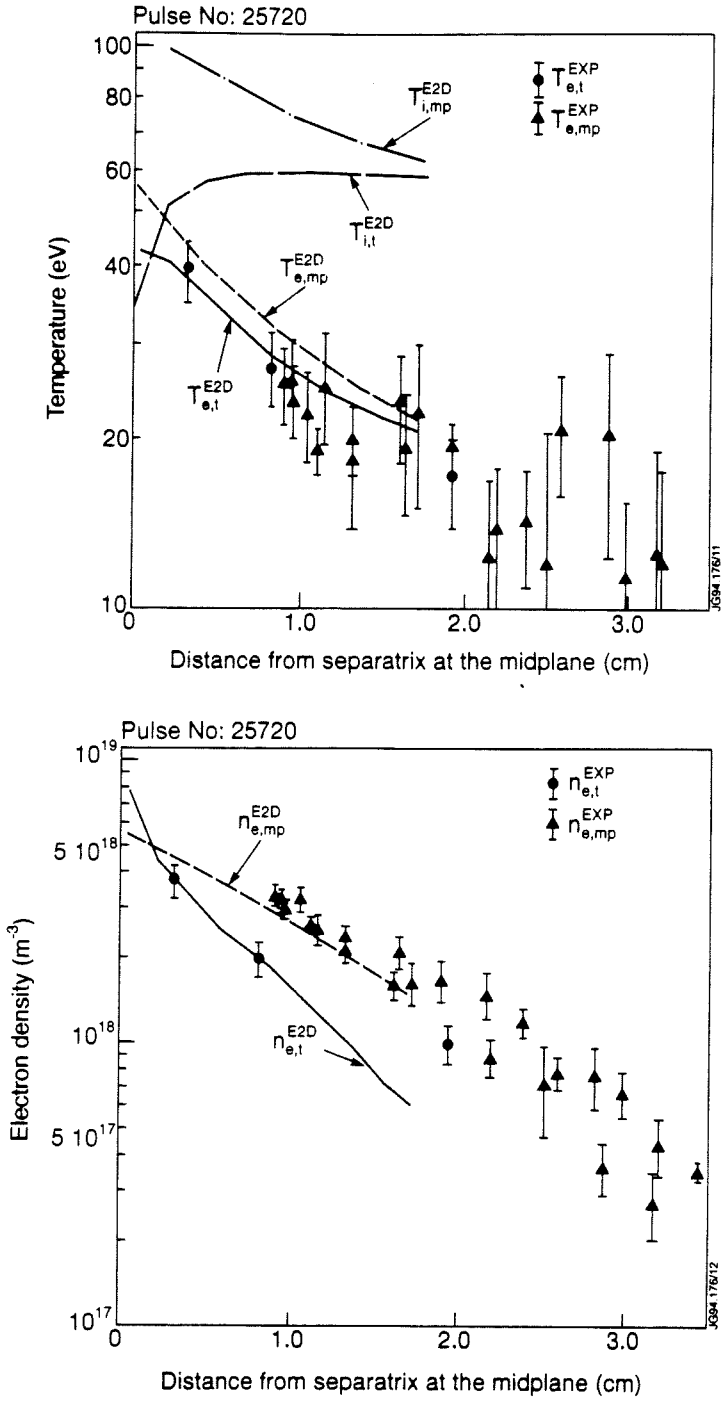

Fig.3. (a) Measured Electron Temperature (EXP) at the divertor target (t) and the midplane (mp) and modelled (E2D) Electron and Ion Temperatures at the midplane (mp) and divertor target (t). (b) Measured Electron Density ($T_i \simeq T_e$ assumed) (EXP) at the divertor target (t) and the midplane (mp) and modelled (E2D) Electron Density at the midplane (mp) and divertor target (t). The divertor target profiles are mapped to the outer midplane along the flux surfaces. The midplane profiles are shifted with respect to the calculated magnetic separatrix so as to achieve experimental electron pressure balance.

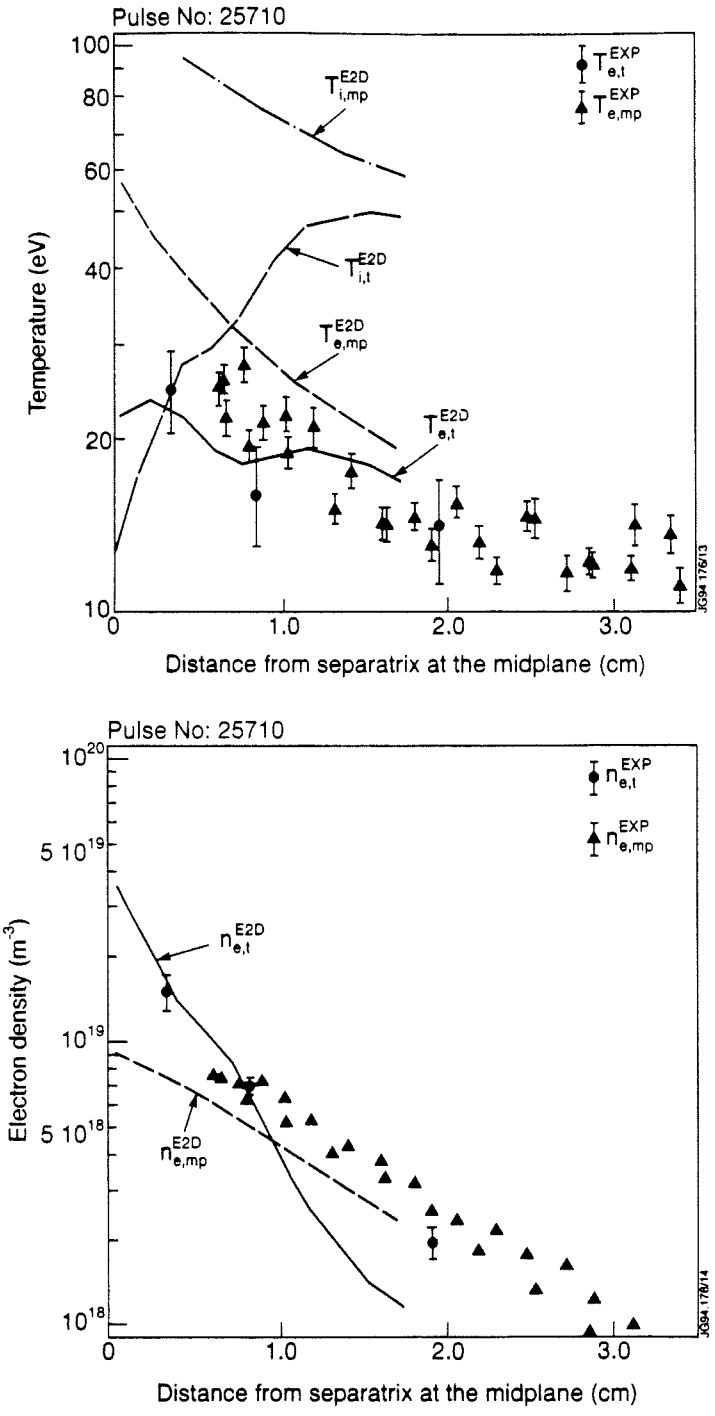

Fig.4. (a) Measured Electron Temperature (EXP) at the divertor target (t) and the midplane (mp) and modelled (E2D) Electron and Ion Temperatures at the midplane (mp) and divertor target (t). (b) Measured Electron Density ($T_i \simeq T_e$ assumed) (EXP) at the divertor target (t) and the midplane (mp) and modelled (E2D) Electron Density at the midplane (mp) and divertor target (t). The divertor target profiles are mapped to the outer midplane along the flux surfaces. The midplane profiles are shifted with respect to the calculated magnetic separatrix so as to achieve experimental electron pressure balance.

Power Flux and Electric Current Flow to the Divertor Target Plates of JET

J Lingertat, K Günther, A Loarte.

JET Joint Undertaking, Abingdon, Oxon, OX14 3EA.

Abstract

Divertor plate heat loads are recognised as a critical design issue for large power tokamaks. Target heat load data obtained during high power divertor discharges at JET show a large, narrow peak of power flux near the strike point of the separatrix and in the same region an electric current flowing from the target to the plasma. We present an analytical model which connects both phenomena and gives some insight into the underlying physics.

1. Introduction

One of the unresolved key issues in the design of a future fusion reactor is the power handling capability of the divertor target plates. There are numerous technical problems concerning the choice of materials and the design of the power receiving parts. Additionally, the physics behind the transport of particles and energy from the plasma to the target plates is only partly understood. This situation is improving by performing dedicated experiments on high power machines combined with theoretical and modelling efforts to understand the experimental results.

In JET, high power divertor discharges have been performed with a specific emphasis on divertor physics issues. A thorough analysis of the spatial distribution of the target heat load and the currents flowing between the plasma and target shows substantial deviations from the commonly accepted picture of the plasma-target interaction. This paper shows examples of experimental results published in more detail elsewhere [1,2,3] and develops a simple analytical model which gives some insight into the underlying physics.

2. Experimental results

2.1 Power fluxes

Narrow power deposition profiles and electric current flow between the target and the plasma have been observed in various series of well-diagnosed divertor discharges at JET. The results apply mainly to NB-heated single-null discharges with typical parameters I_p = 3.1 MA, B_t = 2.8/3.2 T, $\langle n_e \rangle$ = 1.7 - 3.8×10^{19} m^{-3}, P_{NB} = 10/15 MW, X-point target distance = 8/13 cm and for both directions of the $\vec{\nabla}B \times \vec{B}$ drift. As a typical example, fig. 1 shows power deposition profiles on the divertor tar-

get plates derived from Langmuir probe data, using the standard formula $q = \gamma \cdot I_{sat} \cdot T_e/e$ with $\gamma = 7$, together with surface temperature profiles obtained by a CCD camera measuring the thermal radiation. The low dynamic range of the CCD camera does not allow a satisfactory conversion of the temperature data into a power flux profile. However, a rough estimate shows that the maximum power flux derived from the temperature data is at least by a factor of 3 higher than that obtained by extrapolating the probe data towards the separatrix. The temperature profile width at the target is extremely small during H-mode (δ_H = 1.5 - 4 cm), during L-mode it is larger (δ_L = 3 - 6 cm). The corresponding power flux profile width should generally be smaller or equal to $\delta_{L,H}$. The flux expansion factor between the outer midplane and the target plate is $\approx$ 15, so the profile width at midplane becomes during H-mode 1 - 3 mm. The profiles derived from Langmuir probe data are much broader with a decay length of $\approx$ 7 cm (H-mode) at the target.

Integrating the power flux in the narrow profile over the toroidal length shows that it contributes substantially to the total power dumped on the target [1,3].

The existence of peaked power flux profiles on divertor target plates has recently been confirmed on Asdex-Upgrade with high resolution thermography [4].

2.2 Electric currents

Target probes operated near the strike point of the separatrix show as a rule a high positive current at zero voltage I_0 flowing out of the tile. The same behaviour has been previously reported from DIII-D [5,6]. At JET currents $I_0 \geq 10$ A/cm^2 have been regularly observed for both L and H confinement regimes, both directions of the toroidal field as well as for the inner and outer strike zones.

Fig. 2 shows as an example the profiles of I_0 at the target for a NB heated discharge during the L - and H - mode. Here, the X-point position is constant during both phases and one of the probes is near the outer separatrix. Strong currents ($j_{max} \geq 2 \cdot I_{sat}$) flowing from the plate to the plasma are observed near the strike point superimposed on the well known (and smaller) thermoelectric currents [7, 8, 9] that flow from the outer (hotter) to the inner (colder) strike zone.

Fig. 3 shows the current profile for a different discharge with higher spatial resolution (swept X-point). Clearly, the current flows near both strike points in the same direction which implies the existence of a return current in the outer and inner region of the target plate and the existence of a current flowing perpendicular to the magnetic

field lines somewhere in the SOL. That means the plasma flow towards the target is locally non-ambipolar which is in contradiction to the usual treatment of boundary conditions in most plasma codes.

3. Qualitative physical model

In previous papers [2,3] we speculated that both features, the current flow pattern and the narrow power flux profile, have a common origin. A qualitative discussion of the processes involved starts with the commonly used assumption that the sheath potential Ψ_A follows the electron temperature T_e^* near the target plate ($\Psi_A \approx 3 \cdot T_e^*$). If we assume that the electron temperature decreases with the distance from the strike point this implies that an electric field exists which points away from the separatrix. This field causes an electric current $j_\perp$ to flow perpendicular to the field lines and the plasma to drift in the $\vec{E} \times \vec{B}$ direction. Since this current flows across the magnetic field it experiences a $\vec{j} \times \vec{B}$ force. In steady-state this force has to be compensated by a force $\vec{R}$ of equal magnitude and opposite direction. We assume that $\vec{R}$ is generated by friction of the drifting plasma, and that charge exchange between ions and neutrals is the main source of friction. Continuity of the electric current requires the current to flow in a closed loop. Together with the experimental observations that means: the current has to leave the target near the strike point and to return further outside. Such a current flow out and into the target can only be sustained if the sheath potential relaxes from its ambipolar value. In the region, where the current leaves the target the "non-ambipolar potential" Ψ_N should be smaller than its ambipolar Ψ_A value and where the current flows into the target it should exceed its ambipolar value.

The deviation of the sheath potential from its ambipolar value has an additional effect: The power transmission factor becomes larger than its ambipolar value near the strikepoint and slightly smaller further out, i.e. the power flux profile becomes narrower and steeper.

Although our qualitative discussion describes the experimentally observed phenomena quite well, only a quantitative self-consistent theoretical model can answer the important question about the magnitude of the postulated effects and their relevance for future fusion reactors. Obviously, such a model requires a full 2-D treatment of the SOL using the fluid equations with all relevant drift terms, allowing for current flow in arbitrary directions and using the correct boundary conditions [10]. Here we

try to simplify the problem significantly, aiming at an analytical description of the relevant features.

4. Fluid equations

We adapt a theoretical approach used by one of the authors to derive the characteristics of target mounted Langmuir probes. For details the reader is referred to [11]. The model uses fluid equations in slab geometry, where y is the coordinate along the target plate and x is parallel to the magnetic field lines. Z is an ignorable coordinate ($\partial/\partial z = 0$), the strike point is at y=0 and the magnetic field B is assumed to be constant.

We use the standard fluid equations for continuity (1a,b,c), total momentum balance (2) and electron momentum balance (3).

$$\vec{\nabla} \bullet \vec{j} = 0 \qquad \vec{\nabla} \bullet \vec{\Gamma} = S \qquad S = k \cdot N \cdot n \quad , \qquad \text{(1a,b,c)}$$

$$m_i \cdot \vec{\nabla} \bullet \vec{\Gamma} \vec{\upsilon} + \vec{\nabla} p = \vec{j} \times \vec{B} + \vec{S}_m \qquad \vec{S}_m = -\mu \cdot S \cdot m_i \cdot \vec{\upsilon} \quad , \qquad (2)$$

$$e \cdot n \cdot \vec{\upsilon} \times \vec{B} = e \cdot n \cdot \vec{\nabla} U - \vec{\nabla} p_e + \vec{j} \times \vec{B} - e \cdot D \cdot \vec{\nabla} n \times \vec{B}, \qquad (3)$$

where k is the ionisation rate coefficient and μ the ratio of rate coefficients for charge exchange and ionisation assuming cold neutrals. Viscosity and conductivity are neglected ($\eta_{\parallel} = \eta_{\perp} = 0$, $\sigma_{\parallel} = \sigma_{\perp} = 0$) and only the external magnetic field is taken into account. As boundary conditions at the sheath edge we use the Bohm criterion

$$\upsilon(x = \pm L) = \pm c_s^* = \pm \sqrt{(T_e^* + T_i^*)/m_i} \qquad (4)$$

and from non-ambipolar sheath theory

$$j_x(x = \pm L) = \pm e \cdot n^* \cdot c_s^* \cdot \left\{1 - \exp(\Delta - e \cdot U^* / T_e^*)\right\}, \qquad (5)$$

where Δ is the well-known normalised ambipolar sheath drop

$$\Delta = \ln\left\{\sqrt{T_e^* / 2 \cdot \pi \cdot m_e} / c_s^*\right\}, \qquad (6)$$

and the asterisk indicates the sheath edge position (x = ±L).

Considerable simplifications and assumptions are necessary to derive from this set of fluid equations a reasonable and treatable equation for the non-ambipolar potential. Firstly, we assume nearly 100 % replacement of the outstreaming plasma by ionisation, that means

$$\vec{\nabla} \bullet \vec{\Gamma} \approx \frac{\partial \Gamma_x}{\partial x} = S, \tag{7}$$

which is usually fulfilled under high recycling conditions.

Secondly, T_e and T_i are assumed to be constant along the field lines and the density has been factorized

$$n = n^*(y) \cdot \nu(x). \tag{8}$$

Furthermore, we prescribe the profiles of the plasma density, electron temperature and ion temperature to be exponential with different decay lengths λ_n, λ_e, λ_i.

$$n^* = n^*_{e,0} \cdot \exp(-y/\lambda_n) \tag{9}$$

$$T_e^* = T_{e,0}^* \cdot \exp(-y/\lambda_e) \qquad \zeta(y) = \exp(-y/\lambda_e) \tag{10}$$

$$T_i^* = T_{i,0}^* \cdot \exp(-y/\lambda_i) = T_{i,0}^* \cdot \zeta^{\Lambda_e/\Lambda_i} \qquad \Lambda_{e,i} = \lambda_{e,i}/\lambda_n \tag{11}$$

Here it is important to note that given all these simplifications and assumptions, the results from such a theory will scarcely deliver more than qualitative similarities with the experiment, general trends and some insight into the physical processes.

To derive an equation for the potential we first integrate the longitudinal component of the electron momentum equation along the field lines. The result is an equation for the potential U.

$$U = U^* + \frac{T_e}{e} \cdot \ln(\nu(x)) \tag{12}$$

In a second step the continuity equation for the electric current is integrated along the field lines. We evaluate the expression $\vec{e}_x \bullet \left[\vec{\nabla} \times \left(\vec{j} \times \vec{B}\right)\right]$ which gives

$$\vec{e}_x \bullet \left[\vec{\nabla} \times \left(\vec{j} \times \vec{B}\right)\right] = B \cdot \frac{\partial j_x}{\partial x}. \tag{13}$$

After integrating (13) over x we obtain

$$-\vec{e}_x \bullet \left[\vec{\nabla} \times \vec{J}\right] = j_x(+L) - j_x(-L) \quad \text{with} \tag{14}$$

$$\vec{J} = -\frac{1}{B} \int_{-L}^{+L} dx \left\{ m_i \cdot \vec{\Gamma} \bullet \vec{\nabla}\vec{\upsilon} + (1+\mu) \cdot m_i \cdot S \cdot \vec{\upsilon} \right\} \tag{15}$$

On the other hand

$$-\vec{e}_x \bullet \left[\vec{\nabla} \times \vec{J}\right] = -\frac{\partial J_z}{\partial y} \tag{16}$$

The vector $\vec{J}$ in expression (15) has the components $J_y = 0$ and

$$J_z \approx -\frac{2 \cdot m_i \cdot (1+\mu)}{B} \cdot \upsilon_z \cdot n^* \cdot c_s^*. \tag{17}$$

υ_z in (17) is obtained from (3), (2) and (12)

$$\upsilon_z \approx \frac{1}{B}\left(\frac{dU^*}{dy} + \frac{1}{e}\frac{dT_i}{dy} + \frac{1}{e}\frac{T_i^* \cdot d\ln(n^*)}{dy} \right). \tag{18}$$

Equating (14) and (16) and inserting (12), (17), (18), (9), (10), (11) gives an ordinary differential equation for the normalised potential $\Psi = e \cdot U^* / T_{e,0}^*$ at the sheath edge

$$\zeta^2 \cdot \frac{d^2\Psi}{d\zeta^2} + \left(\Lambda_e + Q(\zeta) + 1\right) \cdot \zeta \cdot \frac{d\Psi}{d\zeta} + \left(\Lambda_e + Q(\zeta) + q\right)\left(\Lambda_e + q\right) \cdot \kappa \cdot \zeta^q =$$

$$C\left[1 - \exp\left(\frac{\Delta \cdot \zeta - \Psi}{\zeta}\right)\right] \tag{19}$$

with

$$q = \frac{\lambda_e}{\lambda_i}, \quad Q(\zeta) = \frac{1}{2} \cdot \frac{\zeta + q \cdot \kappa \cdot \zeta^q}{\zeta + \kappa \cdot \zeta^q}, \quad \kappa = \frac{T_i^*}{T_e^*}, \quad C = \frac{\lambda_e^2 \cdot e^2 \cdot B^2}{m_i \cdot T_e^*} \cdot \frac{1}{1+\mu} \tag{20}$$

The equation is written as a function of the transformed variable ζ (see Eq.10) with the two boundary conditions

$$\Psi'(1) = \left.\frac{d\Psi}{d\zeta}\right|_{\zeta=1} = -(\Lambda_e + q)\kappa_0 \qquad \text{and} \quad \Psi(0) = 0, \tag{22}$$

where the first condition means continuity of J_z under the assumption of symmetric profiles in the SOL and in the private flux region and the second vanishing potential at infinity.

Eq. 19 has been solved numerically for a range of the relevant parameters T_e, T_i,

λ_e, λ_i and λ_n. The numerical results are used to calculate the current density flowing to the plate j_x and the energy transmission coefficient γ:

$$j_x = j_{||} = e \cdot n^* \cdot c_s^* \cdot \left\{1 - \exp(\Delta - e \cdot U^* / T_e^*)\right\}, \tag{23}$$

$$\gamma = 2 \cdot \frac{T_i^*}{T_e^*} + \frac{e \cdot U^*}{T_e^*} + \sqrt{\frac{2 \cdot m_i}{\pi \cdot m_e \cdot (1 + T_i^* / T_e^*)}} \cdot \exp(-\frac{e \cdot U^*}{T_e^*}). \tag{24}$$

5. Results

Fig. 4 shows as an example one of the profiles obtained. It is obvious that the calculated profiles correspond to the expected ones. For the parameter set chosen in fig. 4 there is a significant difference between the ambipolar and the non-ambipolar potential at the strike point (~ 1.5 $T_{e,0}^*$) which causes a maximum current of ~ 3 I_{sat} to flow from the target plate to the plasma. The width of the current flow channel near the separatrix is rather narrow (~ 0.1 λ_e), whereas the return current is distributed over a much larger area. The energy transmission coefficient has a high maximum near the strikepoint. However, this maximum is caused mainly by the assumed profile of the ion temperature. An additional steepening of the power flux profile results from the current flowing near the separatrix.

Figs. 5 and 6 show the current density at the strike point and the width of the current flow channel near the separatrix as a function of T_i and $\Lambda_i = \lambda_i/\lambda_n$, whilst T_e, λ_e and $\Lambda_e = \lambda_e/\lambda_n$ are held constant at experimentally determined values. From the experiment we know j_{max}/I_{sat} to be ~ 2. Using our model (fig.5), this value can be obtained e.g. for T_i ~ 200 eV and Λ_i ~ 0.1 or T_i ~ 700 eV and Λ_i ~ 1. However, the relevance of these rather high ion temperatures and small decay lengths can only be assessed experimentally or by a 2D-code which avoids the simplifications made in this paper.

The current density increases with increasing T_i and decreasing Λ_i, whereas the width of the current flow channel shows just the opposite behaviour. An analysis of the dependencies on other relevant model parameters reveals that the calculated quantities are most sensitive to the ratios T_i/T_e and λ_i/λ_e. Clearly, this is the result of Eq. (18). In our model the friction force, and hence the maximum current which

can be sustained, depends on the drift velocity. This in turn depends according to (18) on the gradients of the potential and ion pressure.

The calculated profiles describe the experimentally observed well. However, as previously stated, due to the used simplifications and approximations further conclusions should only be drawn after comparison with 2D-code results. It is of particular importance to verify that the high ion temperatures and short decay lengths obtained within the model are consistent with the code predictions.

6. Summary and conclusions

Power flux profiles at the divertor target plates of JET during NB heated X-point discharges show a large, narrow peak near the separatrix overlaid on a smaller and broader exponential tail.

In the region of the narrow power flux peak a large electron current is flowing from the plasma to the target which has the same direction on both target plates. This implies a current flow perpendicular to the magnetic field lines elsewhere in the SOL.

An analytical model using non-ambipolar fluid theory has been developed which shows that both phenomena are caused by a common mechanism.

The model qualitatively reproduces the experimental findings. Within the framework of the model the main cause of the observed current flow are the radial gradients of electron temperature and ion pressure.

The current and the energy transmission coefficient at the separatrix increase mainly with increasing T_i/T_e and decreasing λ_i/λ_e, whilst at the same time the widths of the current and power flux profile decrease. Large values for the ratio T_i/T_e or small values for the ratio λ_i/λ_e are required to fit the experimental data.

Further experimental and theoretical research is needed to determine the relevance of the phenomenon to ITER. Especially, results from 2-D fluid codes which include all relevant terms and boundary conditions should give further insight into the physics and allow more reliable extrapolations to high power divertor tokamaks.

7. References

[1] Lingertat, J. et al.,The behaviour of the divertor target plates during high performance hot-ion mode discharges at JET, JET Report JET-IR(92)09, (1992).

[2] Loarte, A. et al., Plasma parameters in the vicinity of the separatrix strike points on the divertor target plates in JET, JET Report JET-IR(92)09, (1992).

[3] Lingertat, J. et al., Poster at the 4th Intern. Workshop on Plasma Edge Theory, Varenna 1993

[4] Herrmann, A., et al., this conference.

[5] Buchenauer, D., et al., Jour. Nucl. Mat. 176&177 (1990) 528.

[6] Schaffer, M.J., et al., Nucl. Fusion 31 (1991) 1750.

[7] Harbour, P.J., et al., Jour. Nucl. Mat. 162 & 164 (1989) 236.

[8] Staebler, G.M., et al., Nucl. Fusion 29 (1989) 1820.

[9] Chankin, A.V., et al., Jour. Nucl. Mat. 196-198 (1992) 739.

[10] Baelmans, M., et al., this conference

[11] Günther, K. et al., Contr. Plasma Physics 34 (1994) 484.

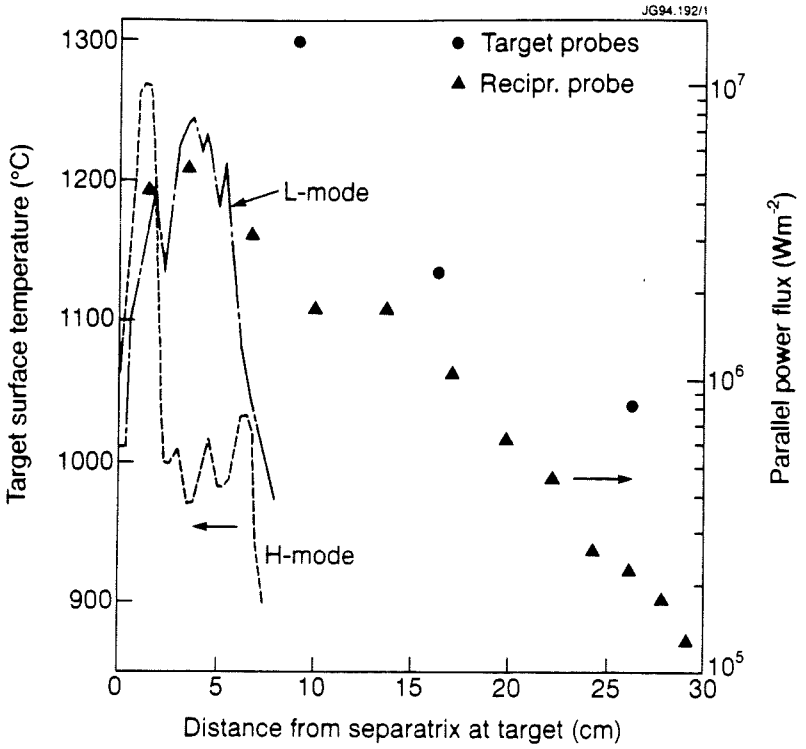

Fig.1 Profiles of the parallel power flux at the divertor target plate derived from Langmuir probes during H-mode and temperature profiles during L- and H-mode from the CCD camera, pulse 25724, outer strike zone.

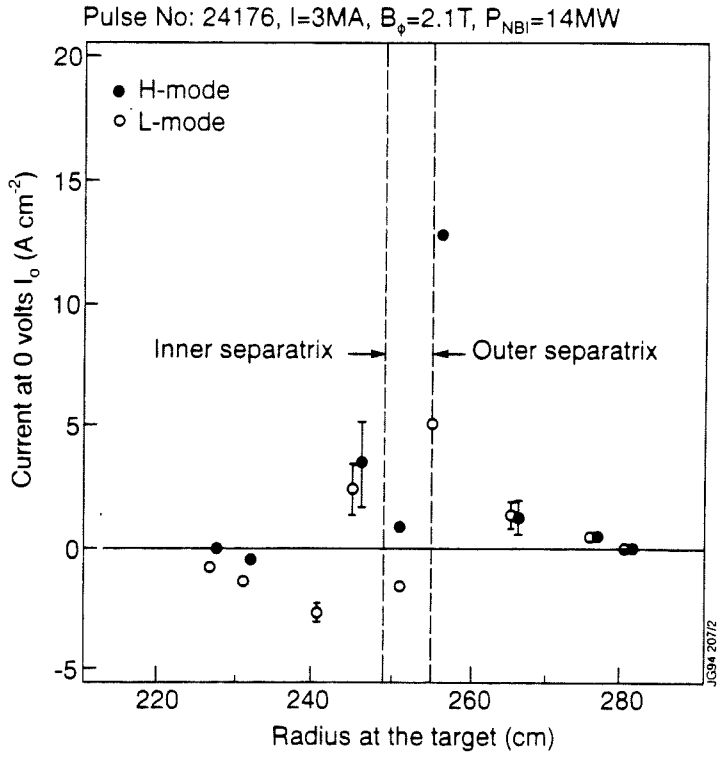

Fig.2 Current profiles from target mounted Langmuir probes (target on vessel potential) in a pulse with stationary separatrix position (I_0 >0 positive current towards the target).

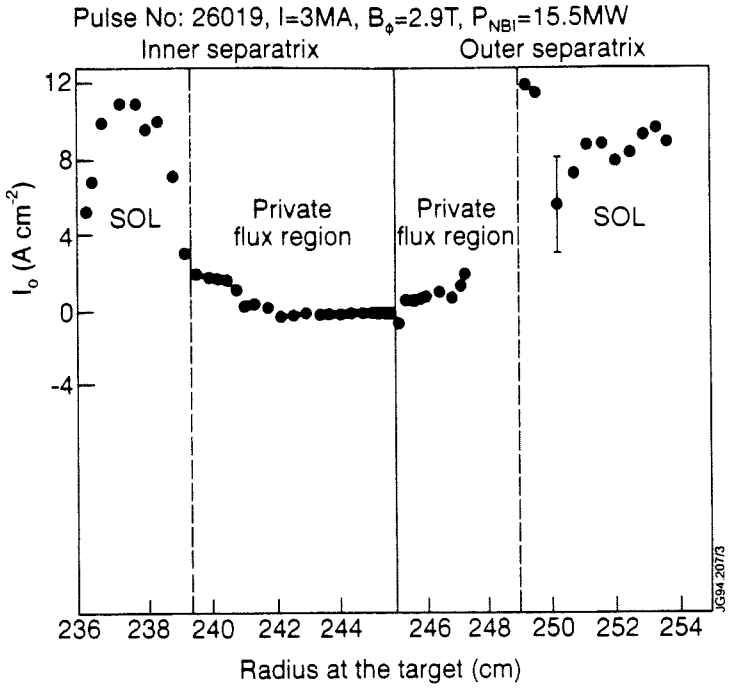

Fig.3 Current profiles from target mounted Langmuir probes (target on vessel potential) in a pulse with swept separatrix position (I_0 >0 positive current towards the target).

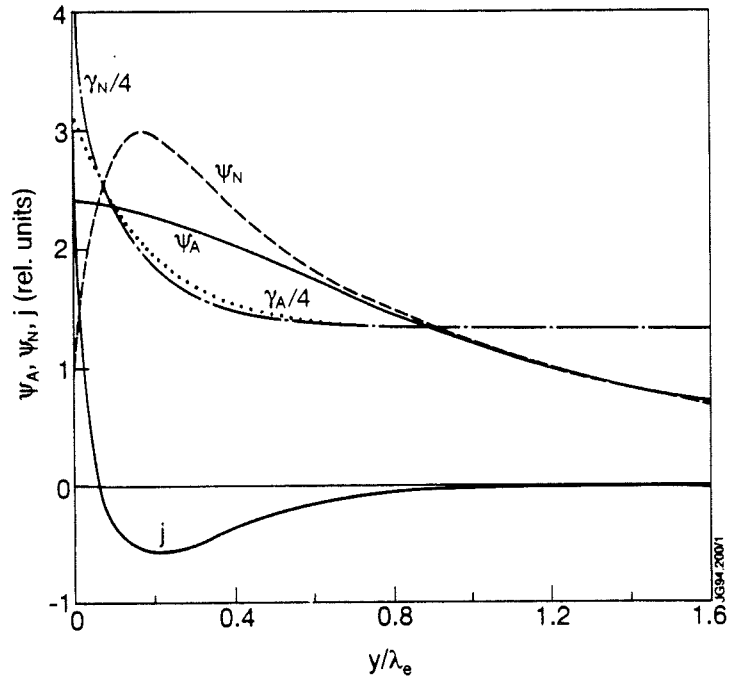

Fig.4 Calculated profiles of the non-ambipolar potential Ψ_N in units of $T_{e,0}^*$, the current density j in units of I_{sat} and the energy transmission coefficient $\gamma_N/4$ together with the ambipolar profiles Ψ_A and $\gamma_A/4$ (T_i= 400 eV, Λ_i = 0.5, T_e = 100 eV, λ_e =1 cm, Λ_e =3, B = 3 T, A = 2, μ = 2)

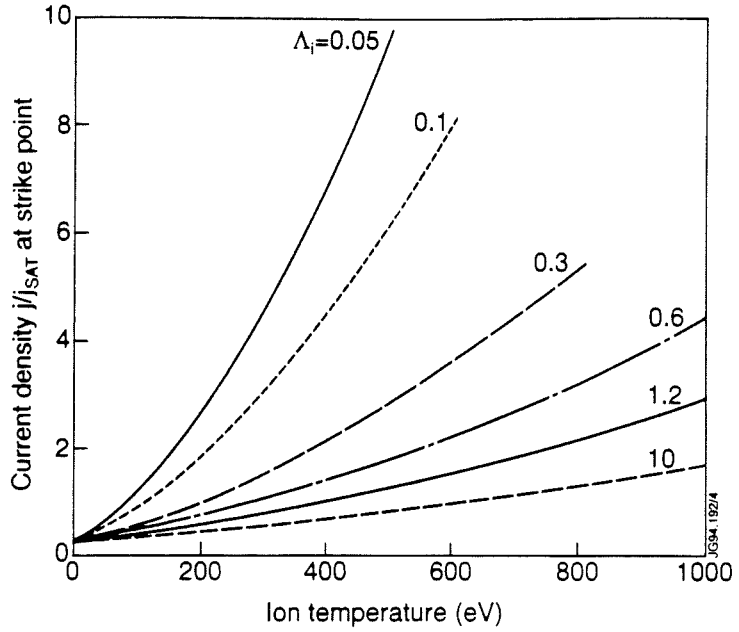

Fig.5 Calculated current density at the strike point as a function of ion temperature for different parameters Λ_i (T_e = 100 eV, λ_e =1 cm, Λ_e =3, B = 3 T, A = 2, μ = 2).

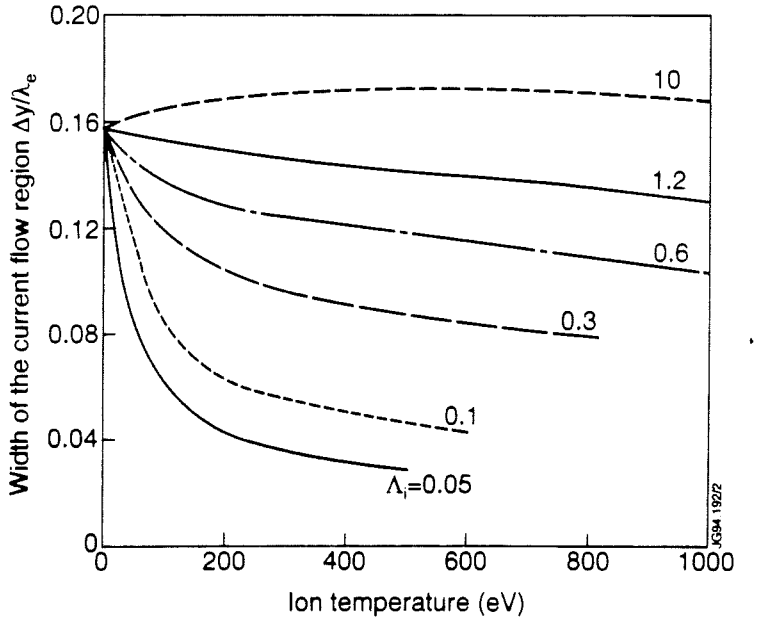

Fig.6 Calculated width of the current flow region near the separatrix as a function of ion temperature for different parameters Λ_i (T_e = 100 eV, λ_e =1 cm, Λ_e =3, B = 3 T, A = 2, μ = 2).

A Study with the EDGE2D Code of the Power Exhaust Problem in ITER Relevant Divertor Plasmas

A Taroni, G Corrigan, R Simonini, J Spence, S Weber.

JET Joint Undertaking, Abingdon, Oxon, OX14 3EA.

INTRODUCTION

Power exhaust in the ITER divertor is an important problem to be solved for the design of this device. A solution based on plasma extinction was suggested by P. H. Rebut and M. L. Watkins [1].

Plasmas that practically extinguish (detached plasmas) in the divertor region have been observed in several Tokamaks, including JET. These plasmas are obviously of great interest for possible extrapolations to ITER. However such extrapolations require a better degree of understanding of the mechanisms leading to plasma detachment than it is presently available.

As a step in this direction an extensive campaign of numerical simulations based on the EDGE2D/U- NIMBUS chain of codes [2] has been carried out at JET in order to study some basic problems related to plasma detachment. In particular we studied the dependence of detachment on mid-plane separatrix density, power entering the SOL, volume power losses in the SOL and geometrical configuration.

Most of the results reported refer to predictions for the JET Mk I divertor. JET operations only started very recently and a comparison between experimental results and these predictions has not yet been possible. However the code reproduce important trends observed in detached plasmas in the old JET divertor configuration.

The modelling assumptions used can be found in refs [3] and [4]. Atomic data are from the ADAS data base[5]. It is shown in [4] that the transport model we are using allows reasonable simulations of attached L-mode plasmas.

EFFECTS RELATED TO MID-PLANE SEPARATRIX DENSITY, POWER ENTERING THE SOL AND GEOMETRY IN A PURE PLASMA

Experimental results in detached plasma regimes suggest that particle, total momentum and total energy flows are strongly reduced at the divertor targets with respect to the case of attached plasmas with comparable values of input power in the SOL and density upstream. Conservation laws imply that such a reduction must be the result of volume loss mechanisms for momentum and energy and possibly of perpendicular transport toward the side walls.

We have studied the efficiency in determining detachment of volume losses alone, by assuming in our computations a set of boundary conditions giving no flux of particles or energy towards the side walls.

In our model the volume power losses are due to both hydrogenic plasma and impurity atomic processes, while volume losses in the momentum balance are related to hydrogenic plasma atomic processes. In particular, as pointed out in [6]-[7], momentum can be efficiently dissipated via charge exchange if the plasma close to the targets enters a regime ($T \leq 5eV$ and not too high density) where the charge exchange mean free path is much shorter than the ionization mean free path, but long with respect to the width of the divertor plasma channel.

For extrapolations to ITER it is important to understand the relative role of the various loss terms in determining detachment.

We consider first the case of a pure plasma and present the results obtained for two equilibrium configurations ($I_p = 3MA$) in the Mk I divertor. (fig 1, SD case and fig 2, V case). By changing the particle inventory N in the boundary region we performed scans in the value n_s of the density at the separatrix mid-plane for two values of the SOL input power, $P = 2.5MW$ and $P = 10MW$, for each configuration (see [3] for the technique).

The main results are illustrated in figs 3 and 4 for the V configuration. Fig 3 shows how the percentage of the power P contributing to the target power load depends on

the density n_s. The values include contributions to both targets. Due to purely geometrical reasons a uniform distribution of the power entering the SOL results in somewhat more power reaching the external target, but the asymmetry is usually not too large (≤50%). The figure also shows the contribution due to recombination at the targets, P_{rec}, which is proportional to the particle flow Φ to the targets.

The ratio f_p of the pressure at mid-plane to the pressure at the targets (related to the efficiency in dissipating parallel momentum), is shown for the same cases in fig 4. Values at the separatrix and at a field line approximately 1 cm outside are given. An average of the pressure at the targets is considered in the definition of f_p (the in-out asymmetry is small, ≤20%).

One sees that as n_s increases, the fraction of power reaching the targets decreases, while the pressure drop increases. However the power due to recombination at targets slightly increases with n_s, implying that Φ increases and that real detachment is not achieved in any of these cases. The maximum value $\Phi \approx 6.7\ 10^{23} s^{-1}$ is for P=10MW, $n_s \approx 4.4\ 10^{19} m^{-3}$.

The figures show that the volume loss terms in a pure plasma become more efficient at low input power, but do not seem to be enough to cause detachment if P≥2.5 MW. The problem is mainly related to power dissipation. A similar result was obtained in [8] for both JET and ITER parameters in a slab divertor channel approximation.

Similar trends have been found for the SD configuration. However in this case the efficiency in removing momentum is somewhat less than in the V configuration. For example it results $f_p=8$ at the separatrix and $f_p=28$ at the magnetic field line 1 cm outside in a SD case with $n_s = 4.2\ 10^{19} m^{-3}$ and P=2.5MW. In a V case with the same value of P and somewhat lower density, $n_s = 3.7\ 10^{19} m^{-3}$, one has $f_p=40$ at the separatrix and $f_p=16$ at the magnetic field line 1 cm outside.

The reason for this is mainly related to effects of the target inclination on neutral reflection and as a consequence on the plasma profiles [3]. In the V case the divertor plasma enters more easily the low temperature regime favourable to momentum

dissipation by charge exchange. The choice of the boundary conditions towards the walls might also have an effect that remains to be assessed.

EFFECT OF IMPURITY RADIATION

A first step in studying the role of impurity radiation in plasma detachment can be performed without simulating in a consistent way impurity generation, transport and radiation. The basic feature of impurity radiation is to reduce the power flowing to the targets and it is interesting to assess how this feature in itself can modify the other flows to the targets (momentum and particles) by reducing the temperature and therefore guiding the plasma into a regime where momentum dissipation due to the hydrogenic species becomes important.

To this purpose we carried out a series of simulations using a simple formula for the radiation efficiency proposed in [9] to simulate carbon radiation in an otherwise pure ASDEX plasma.

The radiation loss term in this approximation is given by:

$$Q_{rad}(T_e)=\alpha_{imp} n^2 L_z(T_e) \tag{1}$$

$$L_z(T_e)=2\ 10^{-18}/(T_n^{1.5}+T_n^{-3}) \quad \text{erg cm}^3/\text{s} \tag{2}$$

$$T_n=\max(10^{-6},T_e/15\text{eV}) \tag{3}$$

α_{imp} is spatially constant and in EDGE2D/U its value is determined at each time step in order to obtain a prescribed value of the total radiated power P_{RI}.

The main results obtained with this approach have been reproduced, as we will show, also by a number of simulations dealing consistently with impurities.

We found that if the conditions of a pure plasma are such that efficient radiation is expected from eqs (1)-(3), i.e. T≤15eV at the targets, detachment can be obtained at large enough values of P_{RI} and it improves as $P-P_{RI}$ decreases. This is valid, obviously with differences related to the geometrical configuration similar to those

pointed out in the previous section, for all of the JET divertor configurations studied so far, including the pre-'92 one and a gas box configuration that are not considered here. In particular, for all the configurations tested, the value of f_p increases as $P-P_{RI}$ decreases and for this reason practically no limit related to insufficient momentum dissipation is found in the fraction of power that can be radiated.

Fgs 5 and 6 illustrate the dependence of detachment on $P-P_{RI}$ in the case of the V configuration. These figures refer to an input power P=10MW and a particle inventory N corresponding to a density $n_s=3.4\ 10^{19}\ m^{-3}$ in the case without impurity radiation.

The variation in the target power load due to recombination shown in fig.5 corresponds to a reduction of the particle flow Φ to the targets from $5.9\ 10^{23}\ s^{-1}$ without impurity radiation to $10^{23}\ s^{-1}$ with P_{RI} =8MW.

Fig.7 shows that the density as well as the pressure drops at the targets, a clear sign of detachment. All these drops are of course related and imply a concomitant drop in neutral density.

The same figure shows that n_s slightly decreases as P_{RI} and detachment increase. This variation of n_s may depend on the transport model, the spatial distribution of impuriy radiation and the boundary conditions towards the side walls. However this is not expected to modify substantially the finding that no strong increase in n_s is required for a transition from an attached to a detached situation induced by an increase in P_{RI}. This may be related to the fact that electron heat conduction and volume energy losses still play a role at the entrance of the detachment region, and the temperature is free to drop below 5eV, contrary to the assumptions in [6].

In our simulations the role of high density n_s in detached plasmas is to reduce the temperature close to the targets and to favour the radiation losses.

Contour plots of T_e for the case $P-P_{RI}$ =4MW are given in fig.8. The divertor region with T≤5eV and reduced ionization appears to be large. This region becomes larger in an even more detached plasma and the divertor closure to neutrals worsens as the ionization region shifts outside the divertor.

A proper evaluation of the spatial distribution of impurity radiation in the SOL and divertor regions require a proper, consistent modelling of impurities. A few exploratory runs with the multispecies version of EDGE2D/U have been carried out in order to study this important problem. The same transport model for impurities and main plasma ions has been assumed.

Results obtained so far show that physical sputtering of Beryllium and Carbon is too low to produce enough impurities to radiate the required level of power for detachment. Injection of Carbon from the walls (that might be interpreted as a very crude simulation of chemical sputtering) can produce the level of Carbon (1-2%), required to radiate a few MWatts in the SOL.

For example in the V configuration, with 10MW input power and N ($\Rightarrow n_s = 3.4\ 10^{19}$ m^{-3}) one obtains $P_{RI} = 4.5$ MW by assuming a carbon influx $\Phi_C \approx 10^{22}$ s^{-1} uniformly distributed along the vacuum chamber . However in this case 70% of P_{RI} as well as 67% of Carbon is above the X-point, where Z_{eff} reaches 1.7. Results of course may differ with impurity species, and impurity injection scheme.

With eqs 1-3 only 25% of the radiation comes from above the x-point for the same P_{RI} (this fraction increases with P_{RI}), however even if the radiation patterns are different the effects of radiation on parameters relevant for detachment (f_p etc.) are similar, as expected.

Even if the most important parameters determining the accessibility to detached divertor plasma regimes appear to be P-P_{RI} and n_s, the geometrical configuration might play an important role also.

For example as indicated in the previous section the SD configuration appears to be less favourable to detachment than the V configuration. Namely for the same power radiated by impurities the V configuration allows plasmas somewhat more detached, at a lower density n_s, than the SD one. In addition it is much more closed to neutrals. This is illustrated in the following table, where n_s is in $10^{19} m^{-3}$, power is in MW, and $S_{H,out}$ is the percentage of ionization source distributed above the X-point.

	n_S	P	P_{RI}	P_t	P_{rec}	$F_{p,sep}$	$F_{p,1}$	$S_{H,out}$
SD	3.8	10	4	3.25	1.23	2.9	12	7
V	3	10	4	3.5	0.7	35	3	0.9
SD	2.8	10	8	0.6	0.3	28	160	39
V	2.2	10	8	0.7	0.2	380	32	10

We remark that while the models used in EDGE2D/U are far from being properly validated against experimental observations, the trends observed in our results are very similar to those observed in detached plasmas obtained in the past in JET. This is confirmed by computations carried out with the old JET configuration and direct comparisons with the experimental information available [10], [11].

CONCLUSION

Our numerical simulations indicate that plasma extinction is unlikely in JET for relevant values of P and n_s without a means to dissipate power in the divertor (or before entering it) other than volume losses related to the atomic processes possible in a pure D or D-T plasma. A similar conclusion is likely to be true for ITER.

It appears that a solution to the power handling problem by plasma extinction in a ITER relevant divertor might imply the dissipation of power by means of impurity radiation. Clearly this requires injection of a recyclable impurity, such as neon or argon, in order to avoid impurity accumulation at targets and walls. The production of intrinsic impurities via sputtering would be minimized inside the divertor with an extinguished plasma, and it would also be small outside if the divertor remained sufficiently closed to neutrals.

Obviously a much greater understanding of impurity control and transport in the SOL than is presently available is required to assess the feasibility of such a solution. Only a careful analysis of experimental results and the validation and improvement of models on the basis of such results can help in this task.

Acknowledgments: K. Borrass, L. Horton, A. Loarte, and G. Vlases are acknowledged for useful discussions.

REFERENCES

[1]Watkins, M.L., Rebut, P.-H., 19th Europ. Conf. on Contr. Fusion and Plasma Phys., Innsbruck, 1992.

[2]Simonini, R., Corrigan, G., Radford, G., Spence, J., Taroni, A., Contributions to Plasma Physics, Vol.34, 368, 1994.

[3]Taroni, A., Corrigan, G., Simonini, R., Spence, J., Vlases, G., Contributions to Plasma Phys., Vol.34, 448, 1994

[4]Loarte, A.,Chankin, A., Clement, S., et al., 11th PSI Conference, Mito, Japan, (1994)..

[5]Summers, H.,P. and von Hellermann, JET report, JET-P(93)35, 1993.

[6]Borrass K. and Stangeby, P.,20th Europ. Conf. on Contr. Fusion and Plasma Phys., Lisbon 1993.

[7]Stangeby. P., Nuclear Fusion, Vol. 33, 1695, 1993.

[8]Weber, S., Simonini, R., Taroni, A., Contributions to Plasma Phys., Vol. 34, 374, 1994.

[9]Schneider, R., Braams, B., Reiter, D., et al., Contributions to Plasma Phys., Vol. 32, 450, 1992

[10]Taroni, A., Horton, L., Loarte, A.,et al. Workshop on ITER Divertor Physics Design, ITER JCT, Garching, Feb. 1994.

[11]Matthews, G., F., 11th PSI Conference, Mito, Japan, (1994)..

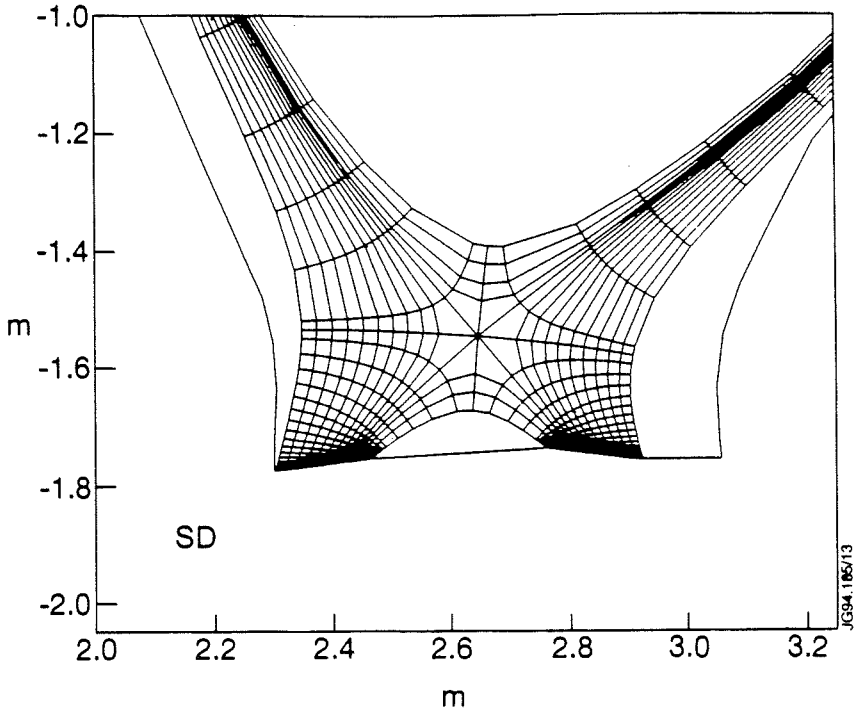

Fig1 SD configuration. Mesh from MHD equilibrium (divertor region).

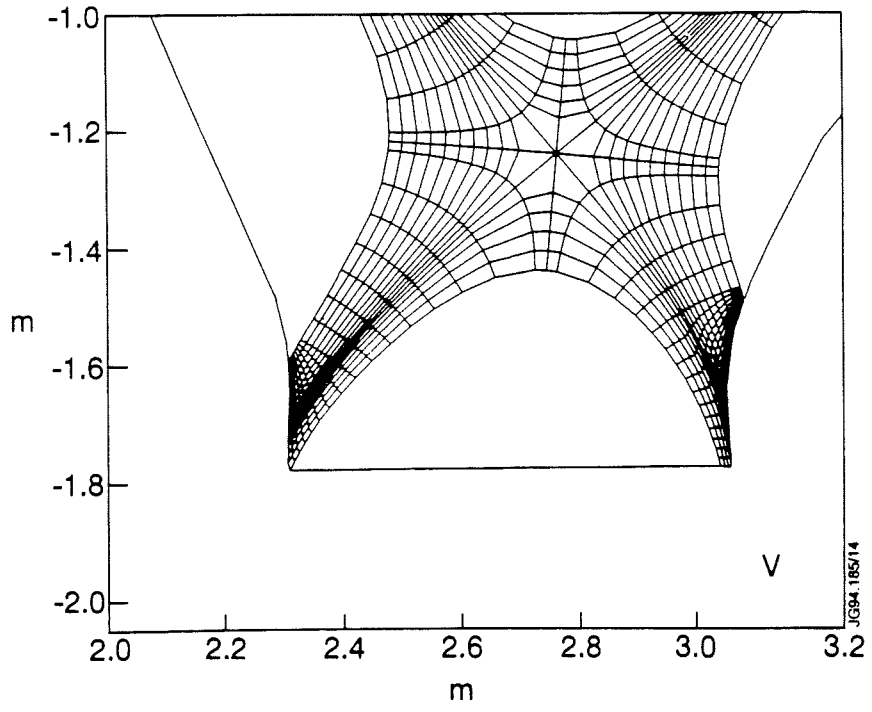

Fig2 V configuration. Mesh from MHD equilibrium (divertor region).

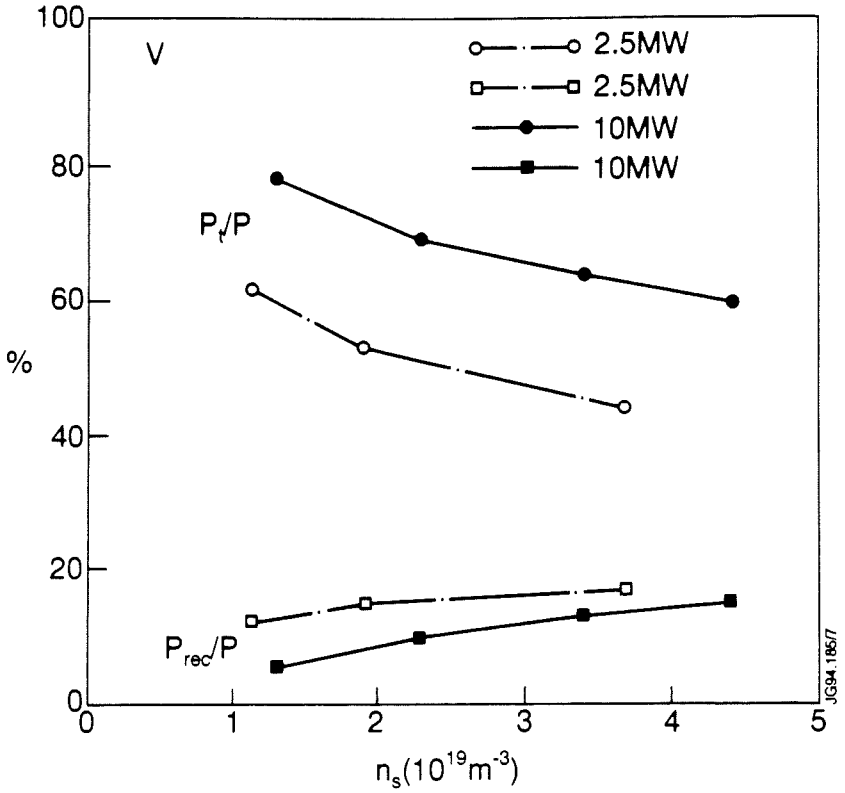

Fig3 V configuration. Percentage of input power contributing to target load and of power due to recombination at targets as a function of n_s.

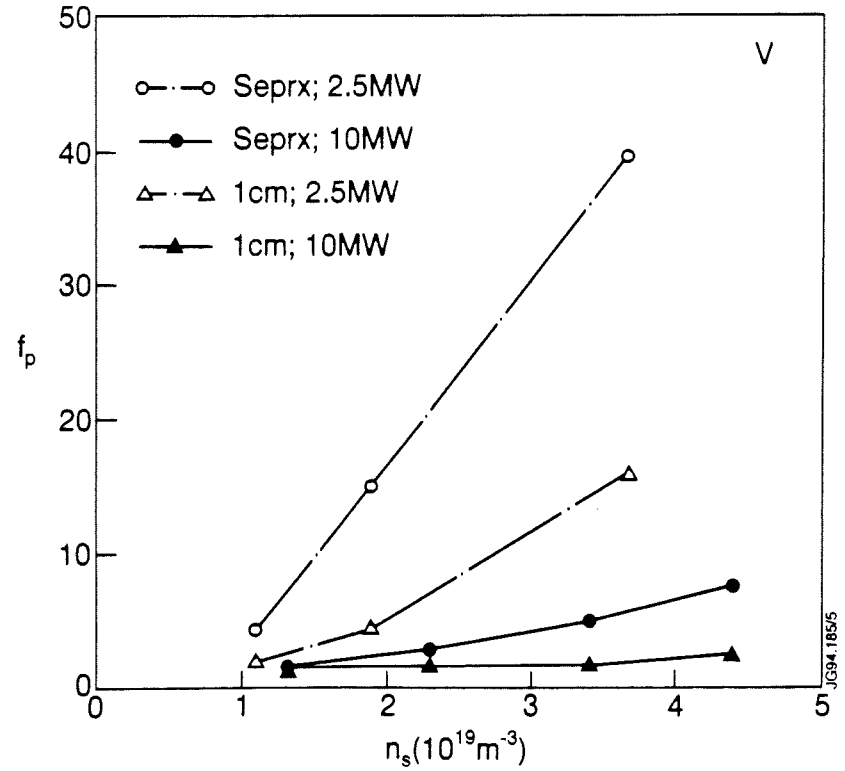

Fig4 V configuration. Pressure drop ratio f_p as a function of n_s.

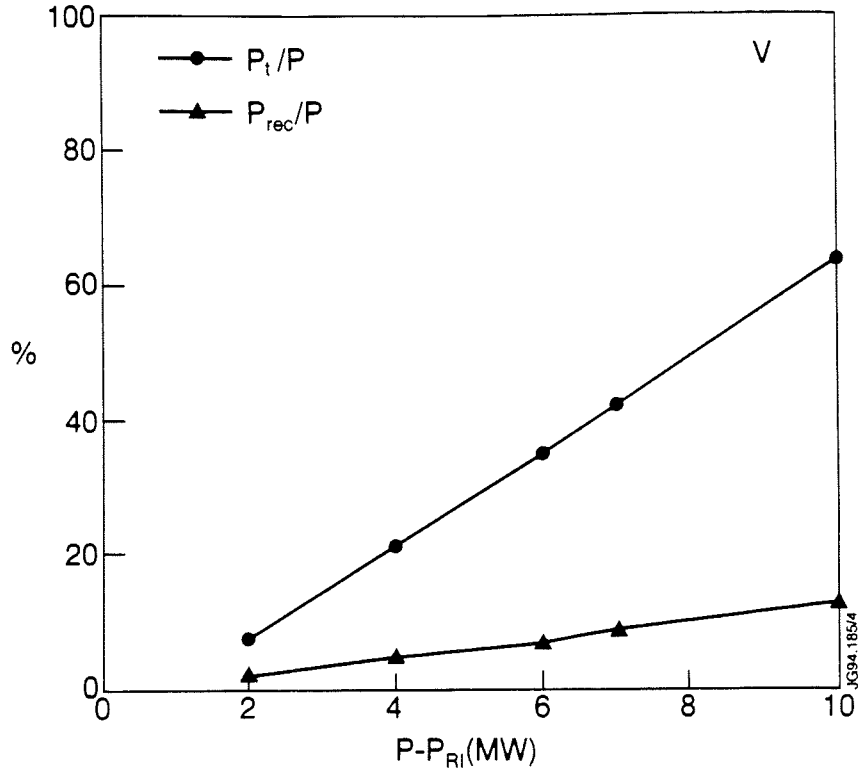

Fig 5 V configuration. Percentage of input power contributing to target load and of power due to recombination at targets as a function of $P-P_{RI}$.

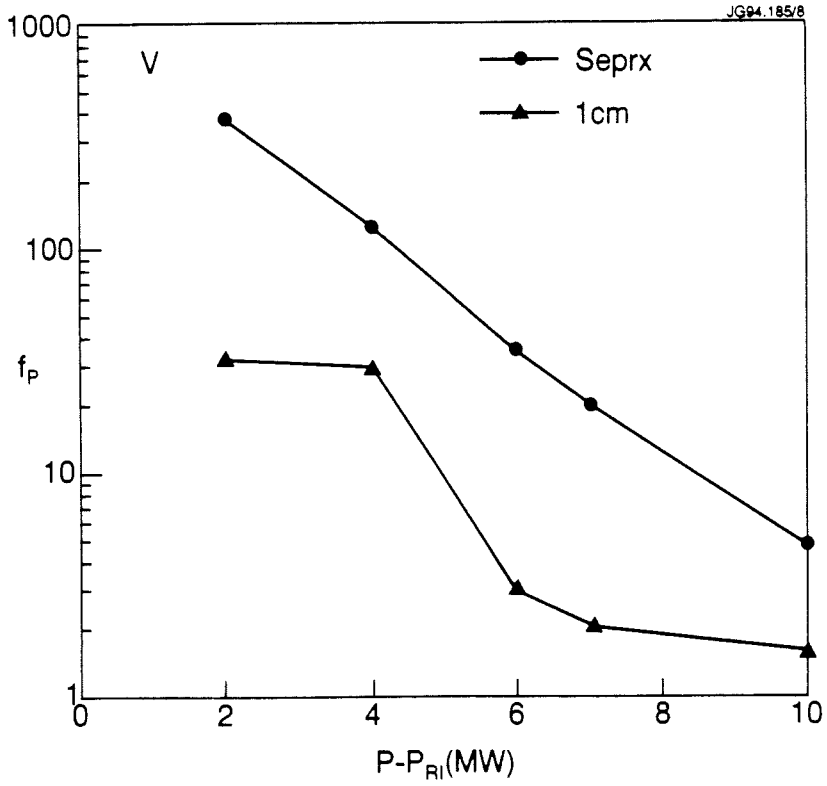

Fig6 V configuration. Pressure drop ratio f_p as a function of $P-P_{RI}$.

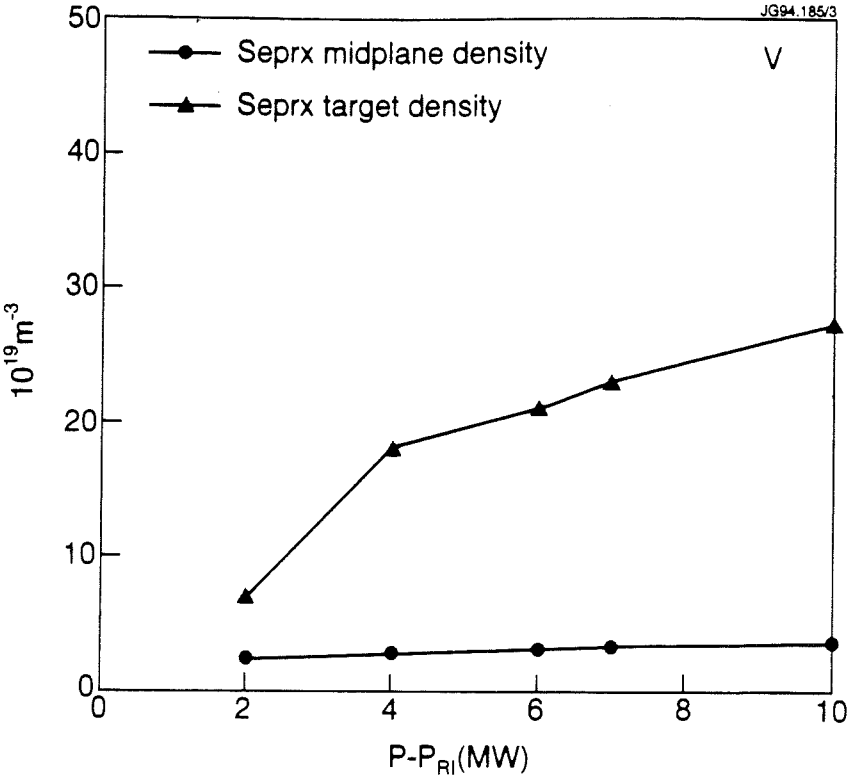

Fig 7 V configuration. Density at separatrix (mid-plane and target) as a function of P-P_{RI}.

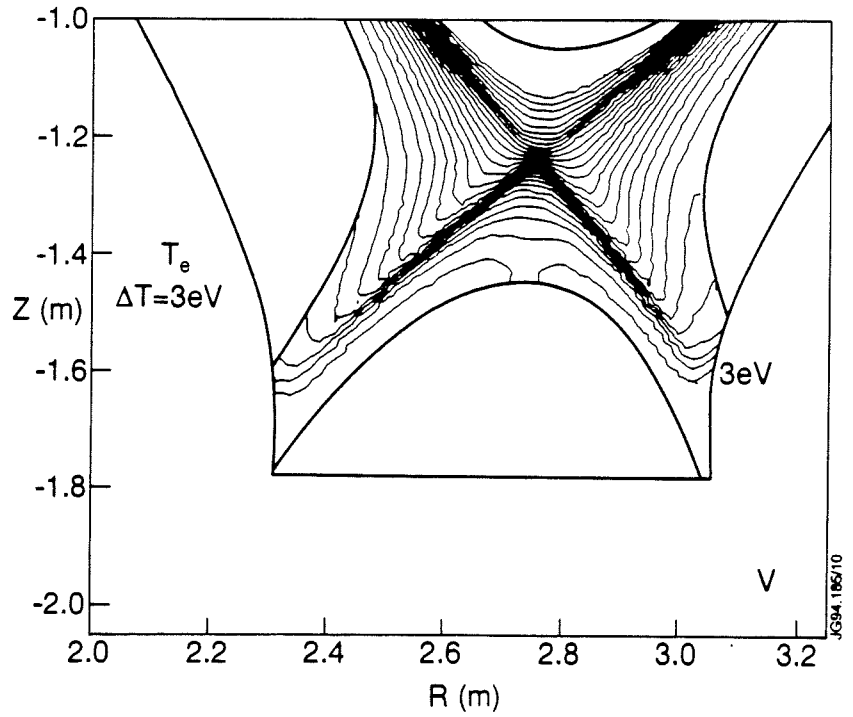

Fig 8 V configuration. Contour plot of T_e for the case P-P_{RI}=4MW.

Plasma Detachment from Divertor Targets and Limiters

G F Matthews

JET Joint Undertaking, Abingdon, Oxon, OX14 3EA.

Abstract

Plasma detachment from a divertor target is defined as the state in which large gradients in total plasma pressure (static plus dynamic) are observed parallel to the magnetic field with consequent reductions in the plasma power and ion fluxes to the limiting surfaces. The origins of this concept and the first experiments in a linear divertor simulator are described. Experimental evidence for this phenomenon from the JET, JT60-U, DIII-D, Alcator C-Mod, and ASDEX-U tokamaks is reviewed along with recent advances in the theory and modelling of detached plasmas applicable to current experiments. Plasma detachment from limiters was first reported by TFTR in 1985, shortly followed by DITE and TEXTOR. This phenomenon occurs in low power discharges near the density limit and is characterised by a shrinking of the layer where most of the ionisation occurs away from the limiter. The physics, phenomenology and relevance to fusion of detachment from limiters and divertors are contrasted.

1. INTRODUCTION

After agreeing a title for this review I have found that the meaning of *detachment*, in the context of plasmas, can provoke considerable debate. I therefore consulted a dictionary and found the following definitions [53]:

- *detachment*, state of being detached.
- *detached*, unconnected: separate: aloof: free from care, passion, ambition and worldly bonds.

If to a laboratory plasma *worldly bonds* are the material surfaces defining its boundaries then *detachment* implies that the primary boundary condition for the plasma is no longer at these surfaces. However, this definition seems rather too vague and so propose the following alternative:

plasma detachment, state in which large pressure gradients (static plus dynamic) are observed parallel to the magnetic field with consequently low plasma power and ion fluxes to the material surfaces bounding the system.

Although the concept of *plasma detachment* may sound rather esoteric, reducing the peak power load to the first wall of a fusion reactor such as ITER [54] is of great practical importance and current interest. For this reason *detached divertor plasmas* are now considered the primary solution to the problem of engineering the ITER divertor. However, as will be described in this paper, *plasma detachment from limiters* although appearing quite frequently in the literature, does not fit within the above definition of *detachment* and seems doomed to remain a fascinating but inconsequential phenomenon.

The basic concept that one might extinguish the exhaust plasma from a fusion reactor in a box of netural gas originated in the gaseous divertor scheme presented by Tenney and Lewin [6] in 1974. In this conceptual reactor design, the neutral pressure is allowed to build up in a remote divertor chamber to a large density (~1Torr). Charged particle-neutral interactions and radiation from seeded argon impurities were to cause the temperature to fall along the divertor channel until, on entering the divertor chamber, the temperature fell bellow 0.1eV. At this point it was evisaged that the recombination rate would become so high that the plasma would recombine before reaching the

chamber walls. Plans for ITER also involve extinguishing the divertor plasma in a neutral gas but in a regime of much lower pressure [54] which is more in keeping with experience from current tokamak experiments. Since the catalytic paper by Watkins and Rebut [5] there has been such a huge amount of anlytical and code work on detached plasmas in reactor relevant regimes that it deserves a review of its own [38]. In this paper therefore the scope is restricted to simulations and theories relevant to existing experimental results.

2. DETACHMENT IN LINEAR SIMULATORS

The gaseous divertor concept of Tenney was first put to the test in a device which, if it were built today, would probably be described as a low power density divertor simulator. The QED (Quiet Energetic Dense) device was built at Princeton Plasma Physics Laboratory in 1976 for the study of magnetic divertor physics [11]. It consisted of a cylindrical vacuum vessel in which an axial magnetic field was generated by a series of external circular coils as is shown in Fig. 1(a). The plasma was generated in an arc jet and flowed down the axis of the device through two limiting apertures for a total distance of about 1.2m before striking the end collector. The parallel power density in the 1-2cm diameter beam was ~5MW m^{-2} in the central section of the machine giving electron temperatures around 5eV and densities around $10^{20}m^{-3}$. Although very much smaller than the parameters expected in ITER, these conditions are comparable to those seen in the divertors of smaller tokamaks.

Gas target experiments on the Princeton QED by Hsu [12,13] showed that stable detached plasmas could be produced by puffing gas into the divertor chamber. Fig 1(b) shows the decrease in the axial heat flux seen on calorimeter C_A and the associated rise in the radial heat flux C_R as the neutral pressure in chamber D is raised. One can see from Fig. 1(b) that detachment occured well bellow the plasma pressure which was between one and two orders of magnitude larger. In these experiments it was shown that the neutral pressure in the end chamber could be varied over an enormous range limited only by the point at which the finger of plasma was pushed out of the chamber altogether. As one might expect this expulsion occured when the neutral pressure exceeded the plasma pressure and resulted in a large (>10) abrupt reduction in the differential pressure between the middle and end chambers. The QED results were modelled by Hsu assuming that the dominant process for energy and momentum removal was collisions between ions and neutrals. This interpretation relies on collisions between ions and molecules. Molecules dominate the neutral population when the electron temperature is too low to produce much ionisation (T_e<5eV). Hsu's model produced a good fit to the QED data and also showed that ion-neutral collisions increased the diffusion coefficient well above the classical ambipolar value based on ion-ion collisions alone. At sufficiently high neutral pressures the electron temperature fell to T_e~0.2eV and the plasma appeared to recombine. Many of these results have more recently been reproduced and elaborated in a small pulsed device [51,52] including an elegant experiment proving momentum transfer to the neutral gas by direct measurement rather than inference [21].

The main weakness of the QED results from the perspective of extrapolation to a tokamak was the fact that the plasma column was not much larger than the ion gyro-radius and the electron temperature was low throughout the device. In a tokamak with a poloidal divertor we would expect to see a hot scrape-off layer T_e=30-100eV in the region adjoining the core plasma with a relatively sharp decrease in temperature at the point at which the ionisation and charge exchange occur. The PISCES machine is very similar to the QED only significantly larger and has performed very similar gaseous divertor experiments [14,15]. In PISCES the plasma column entered a 4.5cm diameter tube which was 90cm long and closed at the far end forming a close fitting channel rather than a gas box. In general the results from the two machines look very similar. However, PISCES has sufficiently

high electron temperature and plasma size to go from the high recycling regime, where a large fraction of the ions reaching the end are recycled as neutrals and reionised in the divertor channel thus amplifying the ion flux reaching the end, to the detached state where the ion flux arriving at the end plate is very substantially reduced. The PISCES experiments confirm the large increase in cross-field transport with neutral pressure reported from the QED device but in a plasma column that is many ion gryo-radii in diameter. Values of $D_\perp$ up to 20 times the Bohm value are reported in PISCES but, unlike the QED data, these results are said to be inconsistent with the classical ambipolar value $D_{\perp a} = kT_e\nu_{in}/(m_i\omega_{ci}^2)$; where ν_{in} is the ion-neutral collision frequency and ω_{ci} is the ion cyclotron frequency. In PISCES the decrease in ion current reaching the end has been shown to be primarily a consequence of the enhanced flow of ions to the sides of the channel. In that sense it is not a purist's gas-target in which the plasma is totally quenched in the neutral gas.

3. DETACHMENT IN DIVERTORS

The most characteristic signature of detachment from a divertor target is an unexpected and large decrease in the ion flux recorded on the target by Langmuir probes without a corresponding decrease in the H_α emission from the vicinity of the divertor. A beautiful example of this can be seen in Fig.2 [16] which shows the ion saturation current from 10 probes in the outer target of the C-MOD divertor. At 0.715s this data shows a relatively sharp decrease on all the probes below the knee in the divertor target whilst those above it actually show a slight rise in current. Close examination of the time history of the detachment shows that it starts closest to the separatrix first and moves outwards. Similar findings have been reported from JET [22] and DIII-D [20]. In DIII-D [20], ASDEX-U [24].and JET[23] the reduction in the ion flux has been shown to be accompanied by a fall in the surface power loading observed on the divertor targets with infra-red diagnostics.

Three main questions arise out of the observations of detachment:

- Why does the ion-saturation current decrease and where does that current go?
- On open field lines we normally expect the plasma pressure at the divertor target to be about half the value near the stagnation point. So what has happens to the pressure parallel pressure balance?
- Last but not least, where and how is the power lost?

3.1 Parallel Pressure Balance and Ion Flux

A simple one-dimensional fluid or kinetic theory of the flow of plasma to a solid surface along the magnetic field, which ignores volume sources of momentum, gives the following expression for the plasma pressure at the sheath edge [25]:

$$P_s = \frac{P_0}{1 + M_s^2}$$

where P_0 is the plasma pressure at the stagnation point of the scrape-off layer (SOL) and M_s is the Mach number of the plasma at the sheath edge. The Bohm condition requires that $M_s \geq 1$ at the sheath edge it is conventionally assumed that $M_s = 1$, giving $P_s = 0.5P_0$. A fluid dynamicist's expression of this condition is that the total plasma pressure (static plus dynamic) is constant along a magnetic flux tube.

Probe measurements of electron density and temperature show that the simple parallel pressure balance is lost during detachment. This can be seen in experiments where target Langmuir probe data is complemented by reciprocating probe measurements in the scrape-off layer, or in discharges which

detach at only one strike point such that a pressure imbalance between the inner and outer strike region can be seen. An example of this in given in Fig. 3 which shows data from a discharge in JET which detaches at the inner strike point [26]. The SOL profile was measured with a fast reciprocating probe and is very similar to that obtained in an attached case. Similar data has been obtained in Alcator C-Mod but in this case the data is from discharges which detach at both strike zones [16] and show significant changes in the SOL profiles, a point which I will return to later.

The static plasma pressure at sheath edge is actually the sum of the electron and ion pressures $P_s = n_{es}eT_{es} + n_{is}eT_{is}$, where T_{es} and T_{is} are the electron and ion temperatures at the sheath edge in units of eV. Langmuir probes can only measure T_{es} and the derivation of n_{es}, the electron density at the sheath edge, also requires assumptions about M_s and T_{is}. Fortuantely, although the static plasma pressure is quite dependent upon the Mach number and ion temperature, the ion flux is more closely related to the total static plus dynamic pressures and is much less sensitive[54]. For this reason large drops in the ion-saturation current seen on target Langmuir probes provide one of the best pieces of evidence for detachment.

The experiments carried out in linear simulators show that if the electron temperature is around 5eV or less that ion neutral collisions can dominate over ionisation and significant momentum removal can be observed. Electron temperature measurements made with target Langmuir probes in ASDEX-U [24], C-MOD[16], JET[26] and DIII-D[20] all show that in the detached regions of the plasma the electron temperture falls to $T_e = 2 - 5eV$. However, the fact that this is a necessary but not sufficient condition for detachment has been shown with JET data [26] where there are cases of attached discharges with temperatures in this range.

As with the linear simulators, the neutral pressures measured in the private flux regions of DIII-D [29] and C-MOD [32] at which detachment occurs are 2-3 orders of magnitude lower than the plasma pressures and in the region of a few mTorr. Unlike the QED results [13] continued puffing into these tokamaks does not substantially raise this pressure but instead drives the main plasma to the density limit. A more closed divertor geometry clearly helps reduce the leakage of neutrals back into the main plasma and should raise achievable divertor neutral pressure, at the price of bringing material surfaces closer to the plasma. However, it should not be assumed that closing the divertor will decouple the SOL plasma density from the divertor plasma density. The record divertor neutral pressure is held by the DITE bundle divertor which reached a neutral pressure of 30mTorr[49] in a very closed geometry. Even at this pressure the hot core of the flux bundle was not detached, although detachment of the outer layers may have led to a partial unplugging of the ducts thus leading to a density limit disruption in the main plasma

3.2 Comparison with Analytical Models

Perhaps the simplest model of detachment is one where we regard the neutral density in the divertor chamber as something we can set to any value we choose. If we think of it in this way then there is nothing surprising about detachment, since if we raise the neutral density high enough there will always come a point at which the ion neutral interactions carry away the momentum. Such a model is not that unrealistic for a linear simulator but in a tokamak the detachment must be self-sustained. Stangeby [17] has developed an analytical theory for the self-sustained gas-target by which he means that the residual ion flux arriving at the target after detachment must balance the ionisation sources. Without this condition the main plasma density would evolve in an uncontrolled way. For this reason *N - the number of elastic collisions experienced by a neutral atom or molecule before being ionised* is crucial to this picture and is shown in Fig. 4(b) [17].

When N is large there is a natural segregation into a neutral collision zone close to the target where ion-neutral collisions dominate and an ionisation zone further away as shown in Fig. 4(a). In his analysis, Stangeby takes this one step further by assuming complete separation of the two zones and then solves the equations for conservation of mass and momentum between the ionisation front and the target plate. The result of this analysis is a reduction in the plasma density at the target which may be understood as follows - To satisfy the Bohm condition the presheath electric field is set up to accelerate the ions to the ion acoustic speed at the sheath. Ion-neutral collisions produce a viscous drag which makes this more difficult and so a larger electric field develops to compensate. This electric field repels electrons and depresses their density via the Boltzman relationship. Fig. 4(c) shows the reduction in ion-saturation current that is predicted by this theory allowing also for the fact the collisions remove energy from the ions. This model therefore appears to predict that in the temperature range observed experimentally, large reductions in ion-saturation current might be expected.

It is worth noting that Fig. 4(c) assumes that all the elastic ion-neutral collisions are effective,by which we mean that the momentum is transferred to the wall after each elastic collision as illustrated in Fig. 4(a). If instead, additional elastic collisions occur on the way out to the wall momentum will merely be transported around within the plasma column. The only experimental evidence for this is shown in Fig. 5 and comes from DIII-D [20] target probe data which seems to show a redistribution of plasma pressure with a reduction near the separatrix and a significant increase further out. However, the huge inverted pressure gradient far from the separatrix may be hard to explain.

Geometry might also reduce the number of effective momentum removing collisions. In the special circumstance that the mean free paths are ordered as:

$$\lambda_{\text{ionisation}} >> \lambda_{\text{elastic ion-neutral}} \approx \text{divertor plasma width}$$

it is easy to imagine that the number of effective momentum removing collisions $N_{eff} \approx N$. However, it is not obvious that in an open divertor geometry there will be enough effective momentum removing collisions before neutrals are elastically scattered into ionising regions of the plasma. Only a two-dimensional code can answer this question.

Borass has looked at the problem of the gas-target divertor from the perspective of how it modifies the SOL parameters [27]. The end of his system is the entrance to the elastic collision zone or "cushion". At this point he derives a boundary condition for the power flow which looks like the normal sheath power transmission factor (≈ 8) but much smaller (0.5-1.5). As in Stangeby's model there is a very low Mach number at this point since the flow velocity is being dragged down by friction with neutrals in the elastic collision zone. This common idea might lead one to expect that the ions become bottled up in the SOL due to friction with the neutrals thus leading to an increase in the particle confinement time for the detached state and therefore a rise in the upstream SOL density.

In practice it requires care to test the predictions of the Borass model because attached and detached states involve simultaneous changes in a number of key parameters. However, it still interesting to ask what happens to the SOL plasma profiles during detachment. Fig. 6 shows reciprocating probe data from C-MOD which shows no increase in mid-plane separatrix density on detachment. However, there is a substantial broadening of the profile which means that the density averaged across the profile does indeed rise. This result is not however confirmed by the results from the DIII-D Thomson scattering system which show no significant change in the edge profiles between the attached and detached cases [28]. JET has published data on this point [27] but the spatial resolution of the LIDAR diagnostic used for this measurement must be regarded as very marginal for the task.

One firm prediction of the Borass model is that the power flow into the elastic collision zone must be small but the location of the radiation does not influence the divertor or SOL conditions. Experiments on DIII-D [29] are in qualitative agreement with this. Fig. 7 shows the distribution of radiated power in similar discharges with deuterium and neon injection. Despite large differences in the distribution of the radiation the divertor and SOL parameters were reported to be very similar.

3.3 Power Balance

From the practical point of view the most important aspect of detached plasmas is that the target power loading is drastically reduced. Perhaps the best known example of this is the JET pulse with 22MW of additional heating which is illustrated in Fig. 8(a) [23]. Measurements of the surface temperature of the beryllium tiles indicated that the power loading had dropped to less than 10% of the input power. One can see from the ion-saturation current traces from the outer and inner target Langmuir probes that both strike zones become detached early on in the pulse. Similar high power gas-target experiments have been carried out on DIII-D using deuterium and neon injection. These both show large reductions in peak power loading (~10) and total power loading although the detachment a the outer strike zone is not total. Far from the separatrix the power profile broadens and the power flux density does not decrease.

Although one might imagine that the problems of pressure balance and power balance are decoupled McCracken and Pedgeley [18] has shown that this is not the case. Taking the conventional picture that the plasma pressure in the divertor is a half of the upstream value, simple two-point analytical models show that as more power is radiated the divertor temperature falls and the ion flux Γ_i to the target increases. The usual equation used for the power flow to the target surface is $P_t = \gamma \Gamma_i e T_e$ where the sheath power transmission factor $\gamma \approx 8$. This allows the temperature to fall to an arbitrarily low level with a corresponding rise in ion flux thus allowing any fraction of the input power to be radiated. However, when T_e becomes sufficiently small the recombination energy for hydrogen ($E_H = 13.6eV$) cannot be ignored. Hence the power flow to the surface becomes $P_t = \gamma \Gamma_i e(E_H + T_e)$. Since Γ_i rises as T_e falls there is a minimum in the target power load corresponding to the point at which ~60% of the power entering the SOL is radiated [18]. This result appears to be confirmed by JT60-U whose radiative divertor experiments are limited to fractional radiated powers of around 60% whilst no decrease in the ion-saturation current seen by the divertor target probes is observed [30].

Borass and Janeschitz [31] have shown that if parallel momentum can be removed from the SOL via ion-neutral interactions then Γ_i need not rise as T_e falls and so the radiated fraction can reach a high level. This connection between fractional radiated powers of 80-90% and large drops in parallel plasma pressure has been demonstrated in JET[23], DIII-D[20] and C-MOD[32]. An example from JET is illustrated by Fig. 8(b).

Tomographic reconstruction using multi-chord bolometer data is now being used to unfold the distribution of the radiation [33,32,29]. Fig. 7 shows the results of such an analysis applied to DIII-D [29]. Fig. 7(a) is before gas-injection, Fig. 7(b) shows the distribution of radiation near the X-point in a detached plasma with deuterium injection and Fig. 7(c) shows the more uniform distribution of radiation associated with neon injection. The injection of impurities to produce attached radiating boundary plasmas which has been pioneered on TEXTOR seems a viable scheme for reducing heat load in limiter and divertor machines [34] but is beyond the scope of the current paper.

In the simplest models of detachment [5,35] the majority of the power is lost by charge exchange and hydrogenic radiation. On JET diagnostic simulations of bolometric data have been carried out for detached discharges with the DIVIMP (for beryllium impurities) and NIMBUS (hydrogen neutral)

Monte-Carlo codes [56]. These discharges were run on the beryllium divertor target but the simulations indicate that neither the hydrogenic processes nor the beryllium impurity radiation are sufficient to account for the power loss. The current conclusion is that carbon impurities, which were not well diagnosed, are responsible for the deficit. JT60-U has the most complete array of spectroscopic divertor diagnostics to date and a preliminary analysis of their radiative divertor data shows that when the radiating region reaches the X-point the radiation is carbon dominated. This is in contrast to the normal case where the radiation is near the target where up to 40% of the power comes from the deuterium [48].

3.4 Location and Stability of the Radiating Zone

In the original ITER concept, most of the power is exhausted in the divertor channel due to charge exchange at a relatively high temperature [5]. This idea has evolved to encompass low temperature gas-target divertors and the need for radiation to cool the electrons However, it is still intended that the radiating zone be located in the divertor channel with a fairly uniform distribution between the target and the divertor entrance [19]. Results from C-MOD [32], ASDEX-U[24,33], and DIII-D[29] indicate that the stable location for the radiating region is near the X-point. The results from JET [23] are ambiguous in this respect because X-point was quite close to the target and the bolometer system had insufficient spatial resolution to precisely locate the source of the radiation as can be seen from Fig.8(b). Results from JT60-U show that a radiating region can be stably maintained between the X-point and the target for several seconds [48] but these discharges do not show the drop in ion-saturation current which signifies detachment [30].

Ghendrih has produced a theory of detachment which has similarities to Stangeby's but solves for the length of the detached region assuming that the neutrals enter uniformly from the private region along the separatrix [35]. He obtains a bifurcated solution consisting of attached and detached states where the detached solution has the ionisation zone up near the X-point. To prove experimentally that there is a bifurcated solution is extremely difficult since you need to prove that either state can exist for a given set of control parameters. However, formal proof of a bifurcation is rather academic since what we really would like to know is whether intermediate stable states exist. The evidence for this is rather mixed. JET data seems to show that detachment can be a gradual process compared to any plasma time scale occurring over many hundreds of milliseconds as can be seen in the inner divertor ion-saturation current trace of Fig 8(a). On ASDEX-U the jump of the radiating region to the X-point appears to be quite fast [33]. On C-MOD the plasma pressure near the separatrix decreases gradually but there comes a point in the process where there is a sudden jump of the radiation to the X-point over a period of a few milliseconds which can be seen in Fig. 2. This data suggest that detachment is complex and not universally consistent with a bifurcation or bistable state.

Hutchinson [37] has recently produced a theory which addresses the whole issue of stability in both detached divertor plasmas and MARFEs. This assumes that momentum conservation is satisfied and that heat flow is via electron heat conduction, and uses a simplified radiation function for the power loss. He then analyses the stability of a thermal front. The thermal front is a region of the parallel temperature profile which is dominated by radiation. Hutchinson's conclusions are that in the detached state the most stable location for the thermal front is near the X-point and that it is probably only stable at positions intermediate between the target and X-point for a narrow range of upstream densities.

3.5 Code Simulations of Detached Divertor Plasmas

Much work has been done on predictive simulations of gas-target divertors for ITER but this is beyond the scope of the current review. I therefore concentrate on fluid code simulations of real plasma pulses in realistic geometries. The realistic geometry is important because we would like to

know if the codes can simulate the detachment which has been observed in very open divertor geometries (see section 3.2). Simulations of detached plasmas in ohmic ASDEX-U discharges have been carried using the Braahms B2 code [39]. At JET the EDGE2D code has been used to simulate a pulse with 10MW of additional heating [40] which is rather similar to that shown in Fig. 8(b).

In both cases the neutrals were modelled with a full Monte-Carlo model and impurities treated using a full multi-fluid calculation or with a single species and a simple radiation formula. There are two common conclusions arising from this work which are important:

- Large pressure drops can indeed be achieved in open geometries.
- In order to reproduce the experimental data a substantial wall source of carbon is required. The yield required is in the 1-4% range which is consistent with chemical sputtering of graphite.

Fig. 9 shows the results of a series of EDGE2D simulations for the 10MW detached discharge [40]. Fig. 9(a) shows how the simulated pressure drop and ion flux density near the separatrix scale with mid-plane separatrix density in a purely hydrogenic plasma. The density range was chosen to be consistent with experimental uncertainties. Although the pressure does start to fall at the highest density the ion flux is still far higher than the experimental value. Fig. 9(b) shows what happens in the lowest density case when the radiated power is artificially raised by the introduction of a carbon impurity. Larger pressure drops can then be achieved and the ion flux falls to approximately the level seen in the experiment. The electron temperature is also in the correct range.

The B2 simulations of ASDEX-U also show that the radiating region (MARFE) is not stable in-between the X-point and divertor. Its preferred location is in the SOL near or just above the X-point as seen in experiments.

3.6 The High Pressure Divertor Solution

The basic principle that the power exhaust and particle flux from a diverted tokamak reactor could be substantially dissipated if not extinguished in a neutral gas appears to have been demonstrated on a modest scale in tokamaks and linear simulators. Current tokamak experiments generally appear to operate in a regime of scale lengths where neutrals enter and leave the plasma in relatively few steps. The high pressure solution where the plasma actually recombines before reaching the walls ,which formed part of Tenney and Lewin's original concept [6], has not yet been demonstrated in any fusion relevant devices. This is also a regime where neutral-neutral collisions, radiation transport and multiple elastic collisions must be considered [36]. Simulations have shown that the high pressure regime may be relevant to ITER [42] but many simplifications were made in achieving the result. The fact that high pressure solutions are achievable at power levels more than adequate for ITER can be routinely observed when around one terawatt of power is diverted from a magnetically confined fusion powered plasma into a high density neutral gas. These spectacular pulses lasting up to 3 hours are the *aurora borealis* [41]. However, in the case of the *aurora borealis* , the large neutral pressure ratio between the magnetoshere (SOL) and the earth's atmosphere (gas-target) is achieved by gravity rather than geometry.

4. DETACHMENT FROM LIMITERS

Detachment was first used to describe results from current ramp down experiments in TFTR [8]. Radiative condensations known as MARFEs had been observed in many machines and have been reviewed by Lipshultz [10]. MARFEs are observed in many tokamaks operating close to the density limit, appearing as an axisymmetric strongly radiating belt of short poloidal extent on the high field side of the tokamak. The interesting thing about the TFTR data was that a transition then occurred

to a state where the radiation was poloidally symmetric with the radiation in a ring extending 20cm from the limiter essentially dropping to zero. In this ring the temperature and density also dropped bellow the detection threshold for the Thomson scattering system.

At about the same time similar observations were made in DITE [9]. Current ramp down was again used to achieve the detached state in ohmic discharges but in this case there was a gradual transition from the attached to detached states without the formation of a MARFE. Most persuasive in the decision to use the term *detached plasma* for the DITE discharges were the high speed cine pictures[46]. In the the normal *attached* state a thin reddish ring shows the ionisation of the recycling hydrogen immediately in front of the poloidal limiter. Few neutrals reach the core and so this region appears darker. Detachment occurs when the ring of H_α light has moved inwards leaving little evidence for ionisation near the limiter. Extensive studies of MARFE formation and detachment have been carried out in the TEXTOR tokamak [43]. Two discharges, one with high and the other low input power but similar fractional radiated powers, γ, always behave differently, as shown in the TEXTOR data of Fig. 10. The low input power discharge will detach but the one with high input power remains attached and, when γ is high enough, forms a MARFE. Samm speculates that the Shafranov shift associated with the high power cases creates a poloidal power asymmetry which precipitates the MARFE [34].

The fast reciprocating probe system on DITE allowed measurements to be made before and after the detachment in the very edge of the plasma. These results are shown in Fig. 11. Interestingly, the density profile hardly changes at all whilst the temperature falls to ~6eV and the profile becomes very flat. The ion flux and plasma pressure at the limiter radius are not substantially reduced and so the term "detached plasma" really means something rather different than in the divertor case. Detachment in a limiter discharge refers to the fact that a poloidally symmetric ionisation front moves away from the limiter surface. This only appears to occur in low power discharges.

The most complete model for detachment from limiters has recently been described by Tokar [44] and this paper includes an extensive discussion of previous work. Tokar is the first to tackle the problem of numerically coupling together the transport of energy with that of plasma and impurity particle transport. This approach successfully reproduces the radiation level as a function of plasma current and density. It predicts similar changes in SOL parameters to those of Fig. 11. The model also explains how in ohmic discharges the thermal collapse induced by an advancing ring of impurity radiation is halted by the contraction of the current channel which in turn raises the ohmic power input thus balancing the radiation.

5. DISCUSSION

Detached limiter plasmas show no evidence for significant changes in parallel pressure balance or ion flux and so are, at least by my definition, incorrectly classified as *detached*. They represent a very interesting phenomenon which appears to be fairly well understood but, owing to the low powers at which it is observed, seems to have little relevance for fusion reactors. This type of limiter discharge must be distinguished from the attached radiating boundary layer which has been extensively studied in TEXTOR [34] and is likely to prove important for both limiter and divertor tokamaks.

Detached divertor plasmas appear very complex in their behaviour and we are only just beginning to obtain a crude understanding of the physics involved. The level of interest is however intense as detached plasmas appear to offer a solution to the very tough problem of designing a divertor capable of handling the power and particle exhaust in ITER. Here are just a few of the questions that await experimental verification:

- Both JET[24] and DIII-D[20] have studied detached H-mode plasmas and find that the confinement is degraded to between 0.8 and 0.5 of the normal H-mode value, depending on the degree of detachment. It is important to know what causes this and whether it would still be observed in a more closed divertor geometry.
- Impurity radiation seems to be required for gas-target operation. This can only be controlled if injected impurities are used. Results from DIII-D[20] and JET[24] indicate that injected neon is poorly retained by the divertor. Further experiments are required to seek a regime which overcomes this problem.
- Theory indicates that divertor geometry affect detachment and so experiments are required to show how open divertors compare with slots and gas-boxes.
- We need to see whether the enhanced cross-field diffusion seen in linear simulators (section 2) plays a role in tokamak divertors.
- Gas-target burn through by ELMs may be a problem when scaled to an ITER and so needs further study.

There is however still plenty to be learned about detached divertor plasmas from existing experimental results. Particularly challenging to our ideas are the exceptions which should not be ignored. For example, JT60-U has performed a more thorough scan of parameter space with a more complete array of boundary diagnostics than almost any other machine and yet do not appear to see detachment, as defined here, from the divertor targets with the $B \times \nabla B$ drift towards or away from the target [30]. Even the machines which do see clear evidence for detachment report significant differences which must be understood. For example, the high performance gas-target discharges in JET seemed to require the $B \times \nabla B$ drift away from the target [45] whereas with the $B \times \nabla B$ drift towards the target, detachment occurred only on the inner divertor leg and before any detachment of the outer leg was observed a MARFE was ejected from the divertor into the inner SOL. It was argued that this was caused by greater in/out divertor asymmetries which were observed when the $B \times \nabla B$ drift was towards the target. However, C-MOD [16] and DIII-D[20] produce good detached plasmas when the $B \times \nabla B$ drift is towards the target. JT60-U [30] and ASDEX-U[24] find that the MARFE has a tendency to move to the top of the machine when the $B \times \nabla B$ drift is away from the target. Further work is clearly required to clarify this issue.

Little has been said about materials and erosion in gas-target divertors because little or no experimental or theoretical work has been done in this area for detached plasmas. In a conventional divertor one is almost totally reliant on extremely efficient local redeposition to reduce the net erosion rates by factors of 10^2 to 10^3 or on the use of high Z materials. With a detached divertor plasma local redeposition can effectively be ignored. On the plus side the ion flux has been reduced but it has been replaced by a larger flux of somewhat less energetic neutrals. The energy spectrum of these neutrals and the sputtering threshold of the divertor materials are critical determining the erosion rate. In current machines erosion is so small it is hard to study but in ITER by virtue of integrated pulse duration alone it will be $\sim 10^4$ times larger - sufficient to convert microns into centimetres. This should, I believe, be regarding as one of the most critical outstanding issues by both ITER and the plasma-surface interactions community.

6. CONCLUSIONS

Although the concept of the detached divertor plasma was thought of and demonstrated in principle over a decade ago in a linear divertor simulator, it generated little interest until the start of the ITER EDA. Now there is an explosion in theoretical, computational and experimental work in the area which may render this review obsolete before it comes out in print.

The use of the term *detachment* in the context of limiters is mainly the result of a visual impression rather than physical definition of what happens. A *detached* limiter plasma usually describes one in which the ionisation front moves inboard of the limiter. The ion flux and plasma pressure at the limiter radius are however little altered. Detachment from limiters still remains the minority interest it always was since there is no experimental evidence that this detached state can exist in anything other than low power discharges. The related use of controlled impurity injection to create radiating but attached boundary layers [34] seems much more relevant to fusion reactors with limiters or divertors.

Detachment from divertors seems to be a very complicated phenomenon involving large gradients in plasma pressure parallel to the magnetic field. Many inconsistencies or at least differences between observations in what is reported from different machines. Geometry appears to play an important role in detachment but the gas-box or slot type divertors proposed for ITER [19] have so far only been adequately tested in small linear simulators. Current experiments all show that in detached discharges the radiating region is located near the X-point and it remains to be seen whether changes in geometry will bring about the uniform distribution of radiation envisaged for the ITER divertor channels. Experiment and theory now show that impurities seem to be required to make detached divertor plasmas work - not just charge exchange as in the original ITER divertor concept. Experiments have begun in the seeding of detached plasmas with recycling impurity gases but our current understanding of impurity transport in these complicated conditions must be regarded as inadequate. There is now a real for new tokamak experiments with a range of closed divertor geometries, as planned by JET and DIII-D, combined with better diagnosis of the detached divertor state.

Acknowledgement
This review has been made possible with the help of many of those working in the boundary physics field.

REFERENCES

[1] G.M.McCracken, J.M.Pedgley, Plas. Phys. & Cont. Fus., Vol 35 (1993) 253

[2] P.C.Stangeby, JET-P(93)13

[3] J.D.Strachen et al., 12th EPS. Conf., Budapest 1985, Vol. 1, 539

[4] U.Samm et al., 20th Europ. Conf. on Plasma Phys. & Cont. Fus., Lisbon (1993)

[5] M.L.Watkins and P.H.Rebut, 19th EPS Conf., Innsbruck 1992, Vol.2, 731

[6] F.H.Tenney and G.Lewin in PPPL report No. MATT-1050 (1974) 75

[8] J.D.Strachen et al. in: Proc. 12th European Conf. on Controlled Fusion and Plasma Physics, Budapest, Hungary, 1985, Part 1, p.263

[9] G.M.McCracken et al., J. Nucl. Mater, **145-147** (1987) 181

[10] B.Lipshultz, J. Nucl. Mater, **145-147** (1987) 15

[11] D.K Owens and M.Yamada, Princeton Plasma Physics Laboratory Report PPPL-1520 (1980)

[12] W.L.Hsu, PhD. Thesis "The gaseous divertor experiment", Pinceton University Dept. of Astrophysical Sciences (1981)

[13] W.L.Hsu, M.Yamada, P.J.Barrett, Phys. Rev. Letts., Vol.49 No.14 (1982)1001

[14] L.Schmitz, et Al., J. Nucl. Mater., **176-177** (1990) 522

[15] L.Schmitz, et Al., J. Nucl. Mater., **196-198** (1992) 841

[16] B.LaBombard et al., American Physical Society Conf., St.Louis (1993) 3S6

[17] P.C.Stangeby, Nuclear Fusion, Vol.33, No.11 (1993) 1695

[18] G.M.McCracken and J.M.Pedgeley, Plasma Phys. and Cont. Fus., 35(1993)253

[19] ITER TAC-4-06 "The ITER Divertor" (1994)

[20] T.W.Petrie, D.Buchenauer, D.N.Hill, et al., J. Ncul. Mater., **196-198**(1992)848

[21] G.Fiksel and N.Hershkowitz, "Extinguishing of Plasma and Momentume in the Experimental Simulation of Dense Gaseous Divertor", submitted for publication.

[22] S.Clement, S.K.Erents, N.Gottardi, et al., APS-DPP, Tampa (1991), JET IR(91) 11

[23] G.Janeschitz, S.Clement, N.Gottardi, et al., in Controlled Fusion and Plasma Heating (Proc. 19th Eur. Conf. Insbruck, 1993), Vol. 16C PartII, Eu. Phys. Soc. (1992) 727

[24] M.Laux, in Controlled Fusion and Plasma Heating (Proc. 20th Eur. Conf. Lisboa, 1993), Vol. 17C PartII, Eu. Phys. Soc. (1993)

[25] P.C.Stangeby in Physics of Plasma-Wall Interactions in Controlled Fusion, JATO ASI Ser.B, Plenum Press, New York (1986) 41

[26] G.F.Matthews et al., Contribution to US DOE/Garching Divertor Workshop (1993)

[27] K.Borass, P.C.Stangeby, in Controlled Fusion and Plasma Heating (Proc. 20th Eur. Conf. Lisboa, 1993), Vol. 17C PartII, Eu. Phys. Soc. (1993) 763

[28] D.N.Hill, Contribution to - Technical Meeting and Workshop on ITER Divertor Physics Design, Garching, (Feb, 1994)

[29] T.Petrie, et al., APS-DPP meeting, 1993, St. Louis Mo. (to appear in Physics of Fluids, 1994)

[30] N.Hosogane, JT60-U, Private communication.

[31] K.Borass, G.Janeschitz, JET-P(93)107 (submitted to Nuc. Fus.)

[32] G.M.McCracken, Contribution to - Technical Meeting and Workshop on ITER Divertor Physics Design, Garching, (Feb, 1994)

[33] V.Mertens, W.Junker, M.Laux, et al., submitted for publication in Plas. Phys. and Cont. Fus.

[34] U.Samm, G.Bertschinger, P.Bogen et al., to be published in Plas. Phys. and Cont. Fus.

[35] P.Ghendrih, GA-A21488

[36] Krashnennikov, Nuc. Fus. 27(1987)1805

[37] I.Hutchinson, "Thermal Front Analysis of Detached Divertors and MARFEs", submitted for publication in Nuclear Fusion.

[38] G.Vlases, Plasma Phy. and Cont. Fus. 35(1993) B67

[39] R.Schneider et al., Contribution to - Technical Meeting and Workshop on ITER Divertor Physics Design, Garching, (Feb, 1994)

[40] A.Taroni, JET, private communication.

[41] A.Brekke, "Physics of the Upper Polar Atmosphere", in press (Ellis Horwood)

[42] Petravic et al., Proc. 4th Int. Workshop on Plasma Edge Theory in Fusion Devices, 1993, Varenna Italy (to be pubished in Contr. Plasma Phys., Berlin)

[43] U.Samm et al., KFA Jul-Report 2123 (1987)

[44] M.Z.Tokar, "Modelling of detachment in a limiter tokamak as a non-linear phenomenon caused by impurity radiation", submitted to Plas. Phys. and Cont. Fus.

[45] G.Janeschitz, in Controlled Fusion and Plasma Heating (Proc. 20th Eur. Conf. Lisboa, 1993), Vol. 17C PartII, Eu. Phys. Soc. (1993)

[46] D.H.J.Goodall, AEA Fusion, Culham, Private communication

[47] G.Jablonski, B.Labombard, B.Lipshultz, et al., APS-DPP meeting, 1993, St. Louis Mo.

[48] N.Asakura, S.Tsuji, K.Itami, et al., APS-DPP, St. Louis, 2R08 (1992)

[49] S.J.Fielding, P.C.Johnson, D.Guilhem, J. Nucl. Mater. 128&129(1984)390-394

[50] P.J.Harbour, private communication

[51] G.Fiksel et al., Phys. Fluids B 2(1990)837

[52] Fiksel et al., Phys. Fl. B 3(1991)834

[53] Chambers Twentieth Century Dictionary

[54] G.Janeschitz, this conference.

[55] A.Loarte, private communication

[56] A.Taroni et al., Contribution to - Technical Meeting and Workshop on ITER Divertor Physics Design, Garching, (Feb, 1994)

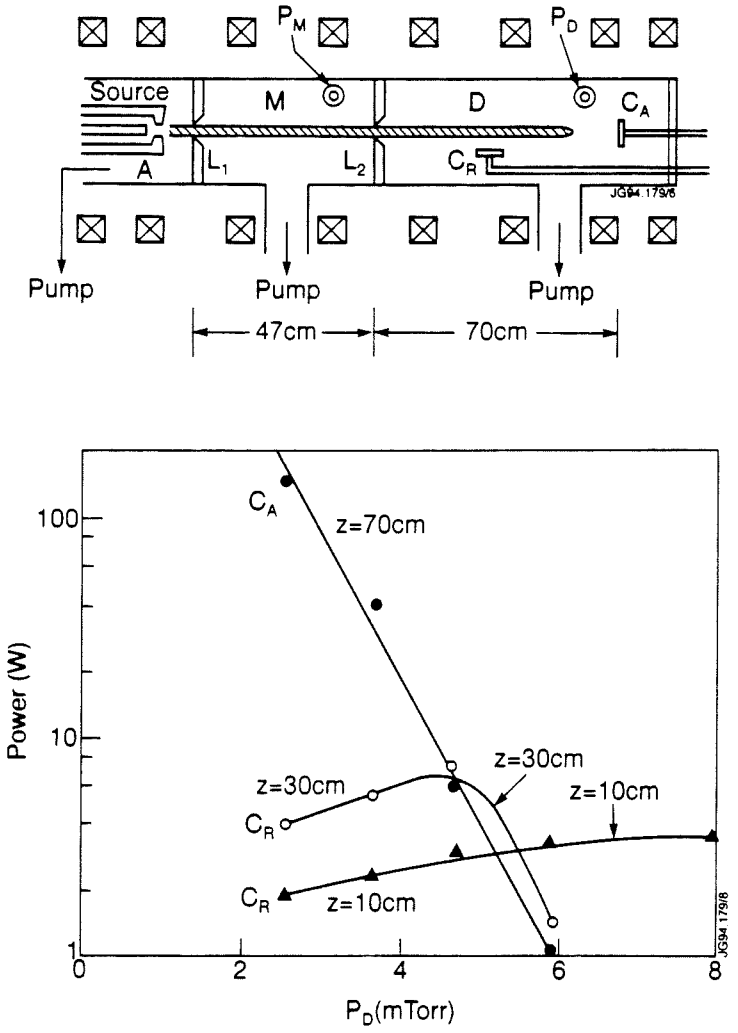

Fig. 1 (a) Schematic of the Princeton QED used for exploring the gaseous divertor concept [13]. C_A and C_R are calorimeters for measuring the axial and radial heat fluxes respectively. (b) Scaling of calorimeter signals with gas pressure in chamber D at various distance, z, from L2.

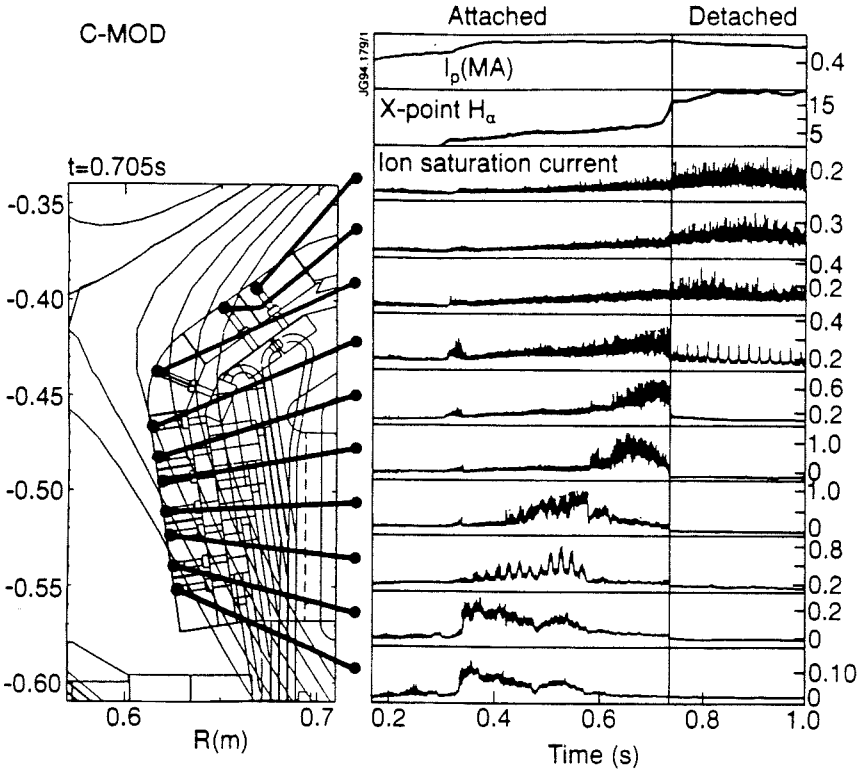

Fig. 2 Time history of the ion saturation currents recorded in the C-MOD divertor during the transition from the attached to detached states [16].

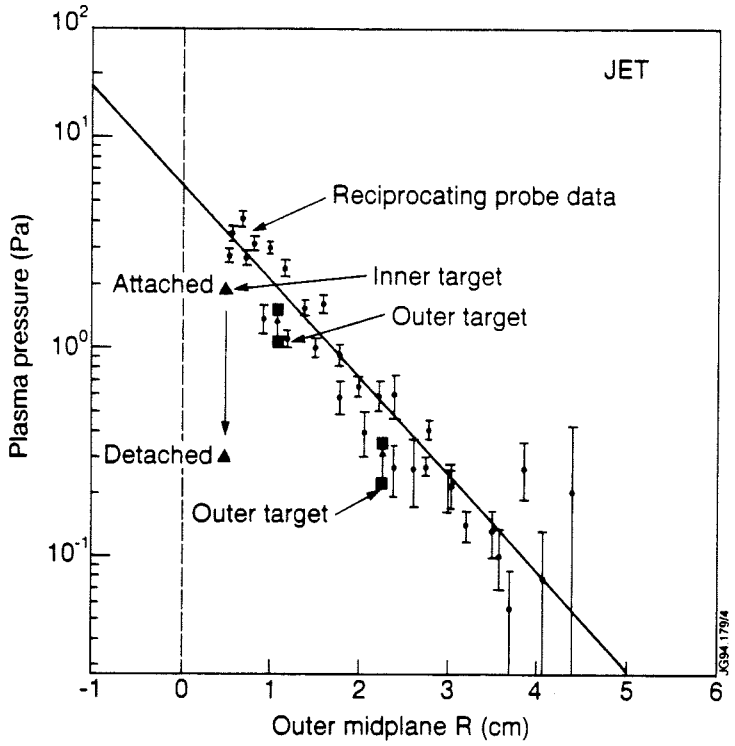

Fig. 3 Profiles of electron pressure derived from the JET reciprocating probe located near the stagnation point and target Langmuir probes during the detachment of the inner strike-zone. No significant changes in the reciprocating probe profiles are observed during detachment of a single strike zone.

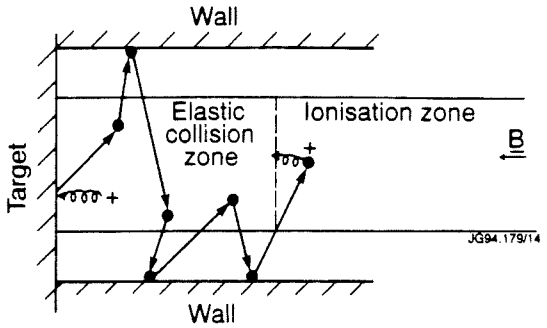

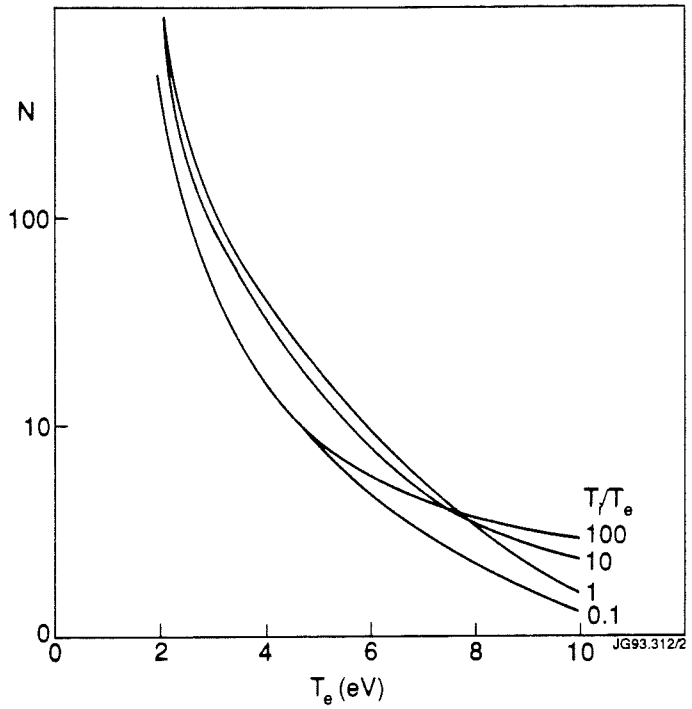

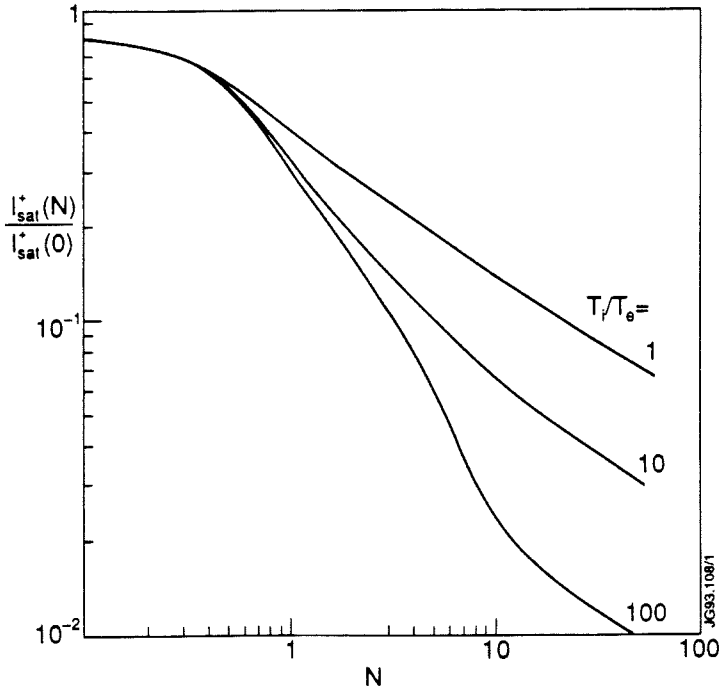

Fig. 4(a) Schematic showing transfer of ion momentum to the wall when N, the ratio of elastic ion-neutral collisions to ionisations is large. (b) N vs T_e for deuterium molecules [17].

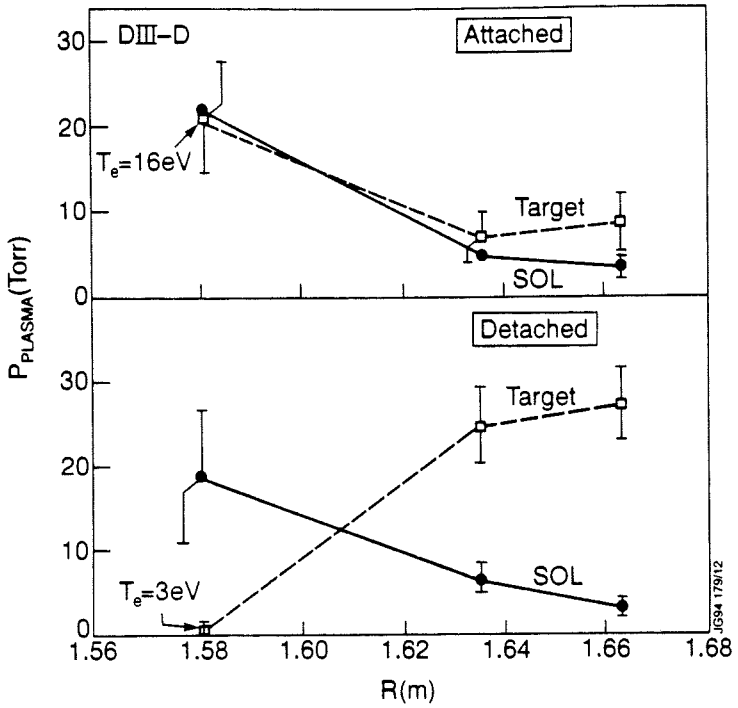

Fig. 5 Plasma pressure in DIII-D measured in the main SOL, using Thomson scattering and charge exchange recombination, is compared with the plasma pressure measured in the divertor with target Langmuir probes assuming that $T_i=T_e$ [20]. Attached and detached cases are compared.

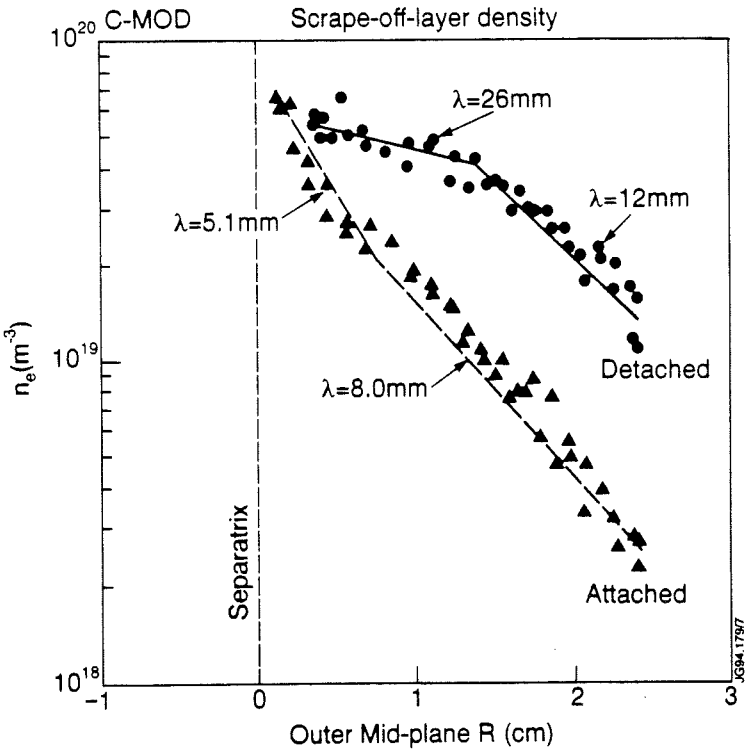

Fig. 6 Density profiles recorded in C-MOD with the reciprocating probe for attached and detached plasma conditions [47]. Profiles are plotted as a function of equivalent distance from the separatrix at the outer mid-plane.

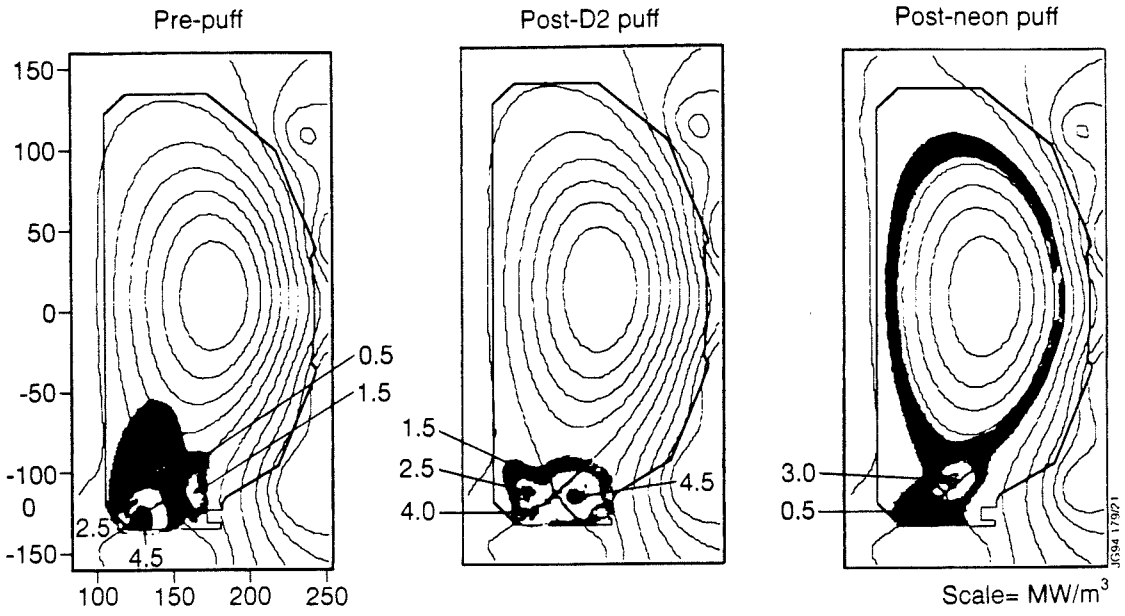

Fig. 7 Tomographically inverted bolometer data from DIII-D [29]: (a) normal attached case showing radiation near strike points, (b) detached phase with radiation near X-point and (c) radiating boundary produced by neon injection.

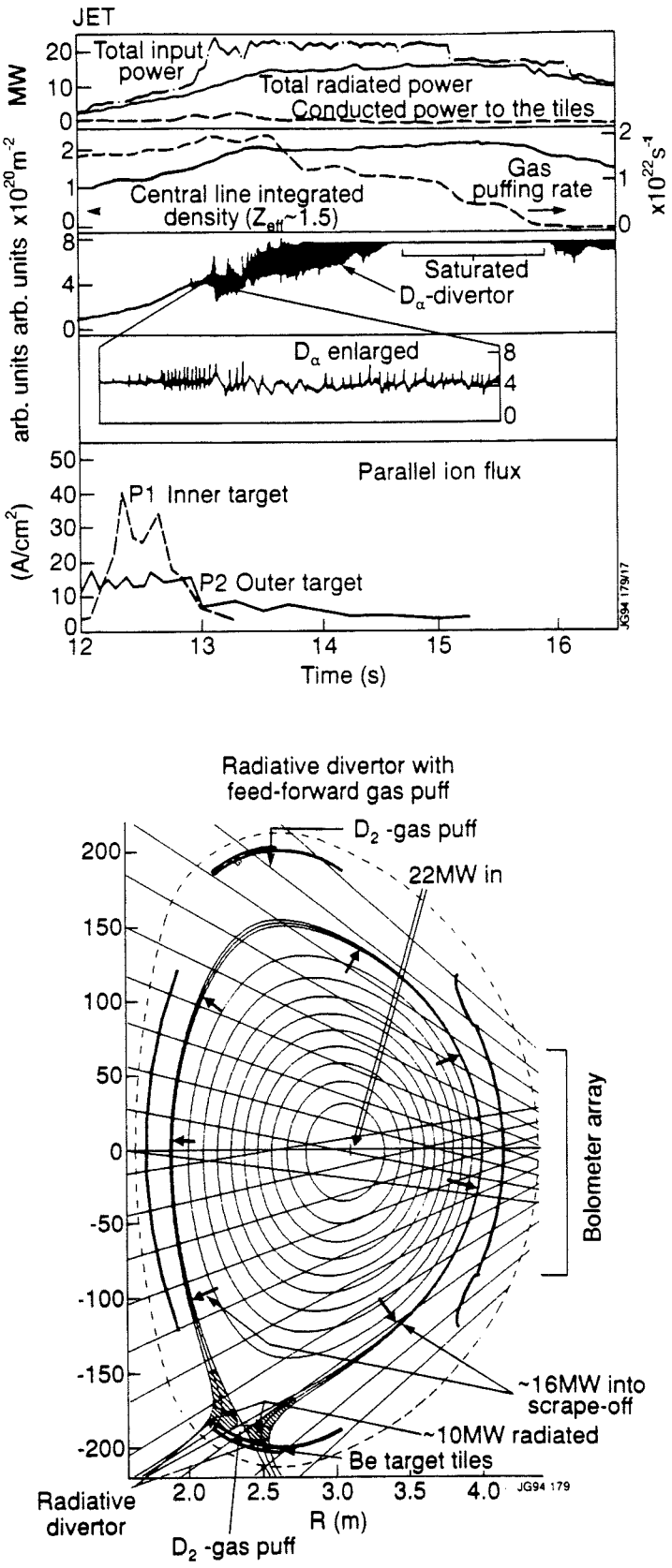

Fig. 8 (a) High power input (22MW) detached discharge in JET showing detachment from both strike zones and (b) magnetic configuration and power balance for this discharge [24].

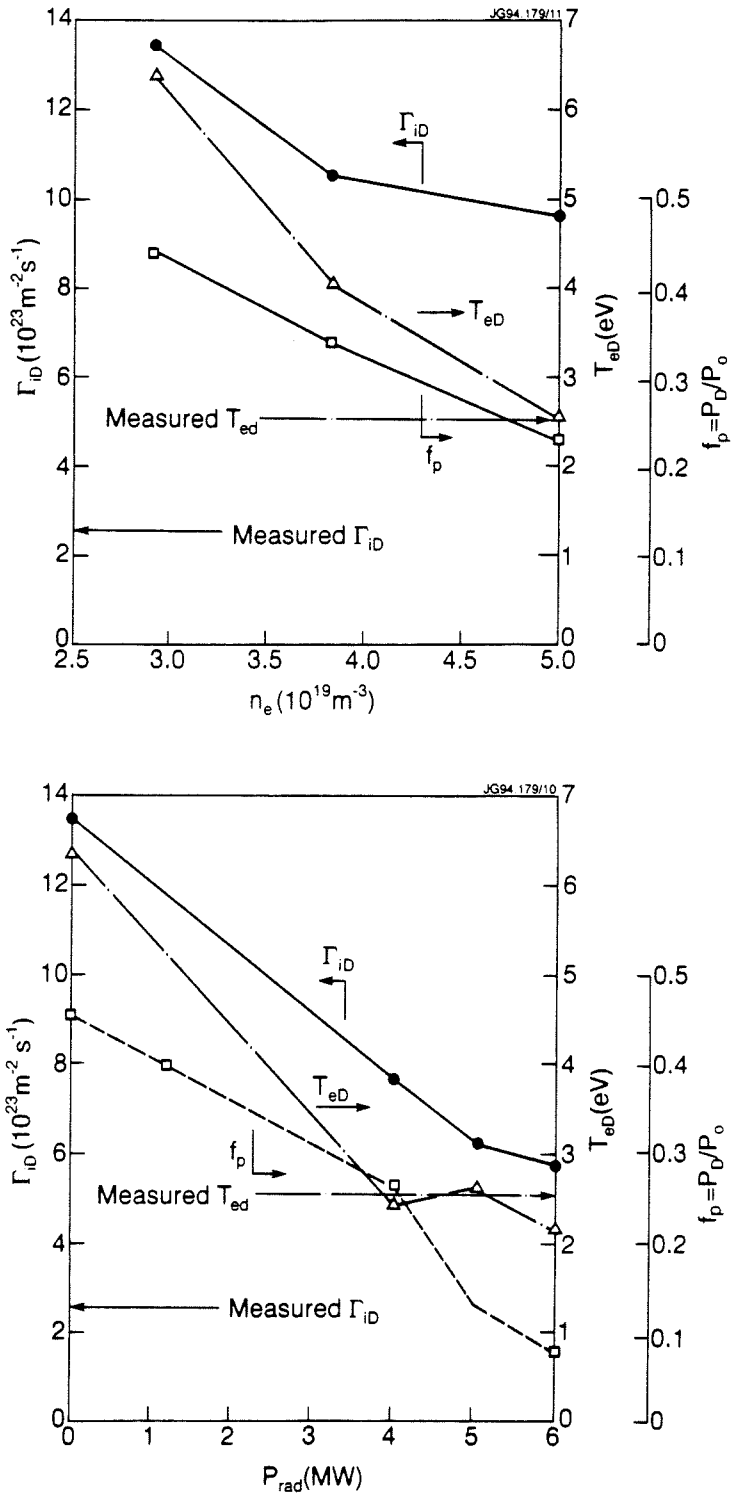

Fig. 9 Simulation of a real 10MW detached JET discharge with EDGE2D [40] : (a) pressure drop along the separatrix, f_p, electron temperature, T_e, and target ion flux, Γ_{iD}, versus mid-plane separatrix density and (b) the same parameters plotted as a function radiated power for the lowest density case in (a).

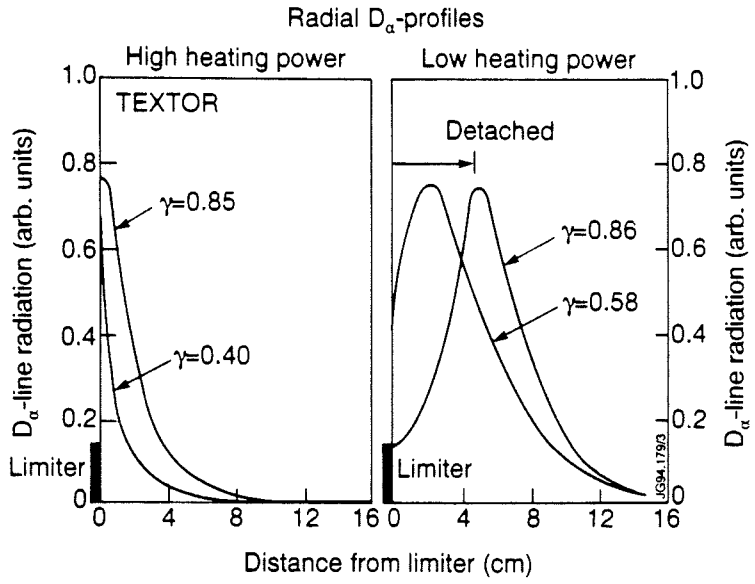

Fig. 10 Radial profiles of D_α from TEXTOR showing high and low power cases. Despite similar radiative fractions, γ, only the low power case detaches.

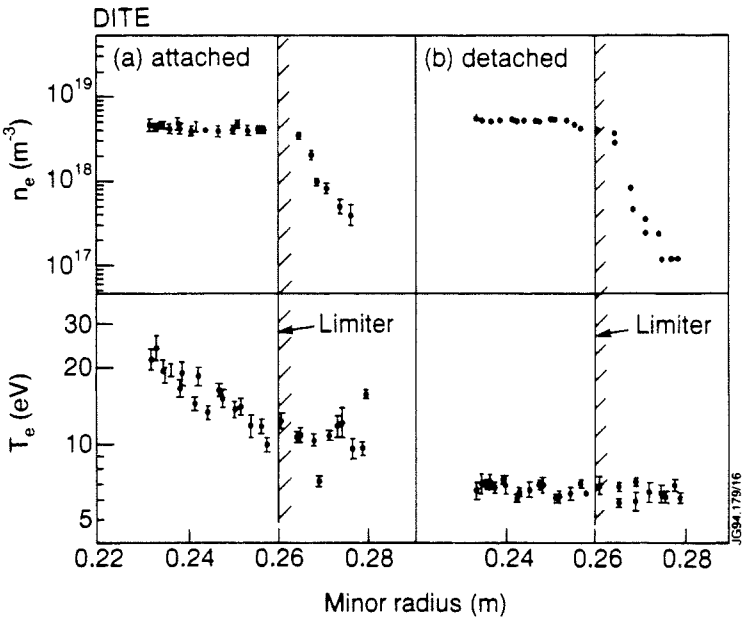

Fig. 11 Reciprocating probe profiles of density and temperature from DITE [9] showing a reduction in edge temperature and a flattening of the profile in the detached state.